Microstructure and stress characterization of engineering materials by advanced neutron diffraction

Weimin Gan

Ecole Doctorale **C**himie – **M**écanique – **M**atériaux - **P**hysique

Habilitation à Diriger des Recherches

Présentée à

UNIVERSITÉ DE LORRAINE

---------- **L'UNIVERSITE DE LORRAINE** ----------

Par

Weimin Gan

Microstructure and stress characterization of engineering materials by advanced neutron diffraction

Caractérisation de microstructures et de contraintes de matériaux d'ingénierie par diffraction avancée de neutrons

Soutenance prévue le 4 avril 2019 à Metz, devant le jury composé de:

Salima Bouvier	**Professeur, University of Technology of Compiègne, France**	**Rapporteur**
Magali Morales	**DR. HDR, Université Caen-Normandie, France**	**Rapporteur**
Werner Skrotzki	**Professeur, Dresden University of Technology, Germany**	**Rapporteur**
Daniel Chateigner	**Professeur, Normandie Université, France**	**Examinateur**
Claude Esling	**Professeur, Université de Lorraine, France**	**Examinateur**
Heinz-Günter Brokmeier	**Professeur, Clausthal University of Technology, Germany**	**Examinateur**
L.A.Leo Kestens	**Professeur, Ghent University, Belgium**	**Examinateur**
Yudong Zhang	**DR. HDR, Université de Lorraine, France**	**Examinateur**

Table of Contents

Curriculum Vitae

Weimin Gan

Senior Scientist

German Engineering Materials Science Centre at MLZ (Dept. of Neutron Scattering)
Helmholtz-Centre Geesthacht

E-mail: weimin.gan@hzg.de

Tel: +49- 89 289 10766 / 14814

Born: 13/09/1980

Male

Married, two children

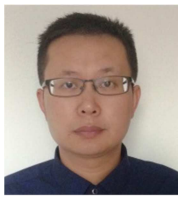

Work Experience (EXPÉRIENCE PROFESSIONNELLE)

Feb. 2012 - present: Senior scientist at **HZG** (**H**elmholtz-**Z**entrum **G**eesthacht, www.hzg.de), instrument responsible for the engineering materials science neutron diffractometer STRESS-SPEC at FRM II (Garching near Munich, Germany) for structure, texture and stress analyses.

Responsibilities & Work:

- maintenance and upgrade of the neutron diffractometer;
- development on new sample environments for *in-situ* or in operando studies;
- management and responsibility for users' neutron beam time;
- user training on the neutron diffraction technology for structure, texture and stress analyses;
- user training on the program/ software for data treatment and interpretation;
- participation in scientific projects;

Feb. 2009 - Jan. 2012: Postdoctoral fellow at HZG department of Structural Research on New Materials; second instrument responsible on neutron diffractometer for texture analysis.

Responsibilities & Work:

- instrument maintenance;
- responsible for uses' beam time mainly for texture analysis;
- participation in scientific project;

Education (FORMATION)

Formation initiale:

Aug. 2004 - Aug. 2008: PhD in materials science, Institute of Materials Science and Engineering, Clausthal University of Technology, Clausthal-Zellerfeld Germany.

Supervisor: Prof. Dr. Heinz-Guenter Brokmeier (TU Clausthal).

Dissertation: Texture and microstructure development of the silicon containing magnesium alloys after equal channel angular pressing.

(Defended on Aug. 15, 2008; doctoral degree obtained with cum laude Good).

Aug. 2002 - Jul. 2004: Master degree study in materials science, School of Materials and Engineering, Harbin Institute of Technology, Harbin P.R. China.

Supervisor: Prof. Dr. Kun Wu (Harbin Institute of Technology, China).

Thesis: High temperature compressive deformation behaviour of the extruded SiCw/AZ91 magnesium matrix composite.

(Defended on June 29, 2004; master's degree obtained).

Aug. 1998 - Jun. 2002: Bachelor study in materials science and engineering, Anhui University of Technology and Science, Wuhu P.R. China.

Thesis: Hardening behaviour of commercial steels with rare earth elements by surface heat treatment.

(Defended on Jun. 02, 2002; bachelor degree obtained)

Formation continue:

Dec. 10 - 14, 2012: TOPAS (Total Pattern Analysis Solutions) training course at Bruker AXS centre in Karlsruhe, Germany.

Jun. 01 - 02, 2012: Workshop on MAUD (Combined Analysis Introduction and Practice), Luca Lutterotti, Caen University France.

May 23 - 25, 2011: 2nd training course on X-ray line profile analysis: from basics to practice; organized by Prof. Dr. Tamás Ungár, Eötvös Loránd University, Department of Materials Physics, Budapest, Hungary.

Apr. 10 - 13, 2006: Crystallographic texture course, organised by Prof. H.-G. Brokmeier, Clausthal University of Technology, Clausthal-Zellerfeld, Germany.

Scientific Qualification (QUALIFICATIONS SCIENTIFIQUE)

Knowledge of (Connaissances sur):

- Materials science & engineering
  - Crystallographic texture
  - Theory of phase transition / thermodynamics
  - Theory of crystallographic defects and plastic deformation
  - Optical and mechanical properties of materials
  - Materials synthesis and processing
- Diffraction theory
  - X-ray and neutron diffraction
  - Scattering behaviour of materials

Equipment operating ability (Aptitude à la manipulation des équipements):

- Operating laboratory X-ray diffraction (phase identification, texture, stress and diffraction profile analysis).
- Design and operation of large facilities of synchrotron radiation and neutron scattering (phase transition/kinematics, texture, strain/stress analysis).
- Development on new sample environments for *in-situ* or in operando study of materials processing (tensile/compression, heat treatment, welding and etc.).
- Conventional thermal treatments (annealing, normalizing, quenching, tempering and chemical heat treatment).
- Conventional thermo-mechanical deformation (rolling, extrusion, forging and swaging).
- Advanced severe plastic deformation techniques (ECAP, HPT, ARB, etc.).

Programming ability (Aptitude de programmation):

- PANalytical Empyrean X-ray diffractometer.
- STRESS-SPEC engineering materials science neutron diffractometer.
- HEMS high energy synchrotron materials science beamline (for phase transition, texture and strain/stress analyses).
- Programs (e.g., StressTextureCalculator using neutron and synchrotron 2D images data, FIT2D, GKSS-ODF, JTex, BEARTEX, MTEX, PopLa, IsoDec) for pole figure and ODF, physical properties calculations.

- Programs (e.g. MAUD, TOPAS, Powdercell, FullProf, MWP or CMWP-Convolutional Multiple Whole Profile) for whole diffraction pattern analysis (for structure, texture, stress).
- Use of VPSC (**V**isco **P**lastic **S**elf **C**onsistent) software for simulation of plastic deformation and texture of polycrystalline material.
- Python programming (standard function).

Language skills (Aptitudes linguistiques):

- Chinese as mother tongue.
- Excellent in writing, listening and speaking English.
- Good in writing, listening and speaking German.

Professional activities

Teaching activities (Activités d'enseignement):

Owing to the nature of my work as instrument scientist of neutron scattering, my teaching activities were mainly related to training for users who need neutron scattering for materials research. This kind of training includes neutron course (theory and practice) and on-site training / teaching during the allocated neutron beam time, and data analysis from raw images to final interpretation.

For the neutron courses, the detailed information concerning the course name, time, number of persons enrolled in the courses (mainly the texture school) and my contribution, are summarized in the following table.

Date	**Place**	**Course name**	**Partici pants**	**My contribution**
Mar. 31, - Apr. 03, 2008	Helmholtz-Zentrum Geesthacht, Germany	Texture school (Crystallographic Textures – basic course)	24	- Neutron texture measurement - From neutron data to pole figures
Oct.15 - Oct. 16, 2013	FRM2, Technische Universität München, Garching, Germany	TUC-MLZ texture school, from area detector pictures to pole figures	15	- Neutron scattering instruments - Principles of data treatment
Sep. 29 - Oct. 01 2015	Clausthal University of Technology, Germany	Texture School at CZM (**C**lausthaler **Z**entrum für **M**aterialtechnik)	20	- STRESS-SPEC neutron diffractometer for texture and stress analyses - practical course
Feb.27-Mar.03. 2017	FRM2, Technische Universität München, Garching, Germany	Application of Neutrons and Synchrotron Radiation in Materials Science with special focus on Fundamental Aspects of Materials	50	- practical course (guided training), neutron diffraction for texture and residual stress
Mar. 06 - Mar .07, 2017	FRM2, Technische Universität München, Garching, Germany	Engineering Materials Science Workshop	17	- Neutron scattering on engineering materials - practical course (guided training), neutron diffraction for texture and residual stress

Moreover, I also contribute to the training work on the neutron instrument scientists from the neutron facilities around the world. Such kind of training has been done for,

- Dr. Rongdeng Liu, instrument scientist of the NTD (Neutron Texture Diffractometer) at CARR (China Advanced Research Reactor, Beijing, China), Department of Nuclear Physics, China Institute of Atomic Energy, Beijing China (Oct.04 2016 - Oct. 31 2017). His purpose is to learn the texture measurement and data analysis by neutron diffraction.
- Dr. Rifai Muslih, instrument scientist at DN1 (Residual Stress Diffractometer) at the GA Siwabessy Multi-Purpose Reactor in Serpong, Indonesia (May 01-31. 2017). His purpose is to learn the instrument control and texture measurement by neutrons.
- Dr. Tri Hardi, instrument scientist at DN2 (Texture Diffractometer) at the GA Siwabessy Multi-Purpose Reactor in Serpong, Indonesia (Aug 14 - 18. 2017). His purpose is to learn the texture measurement and data analysis by neutron diffraction.

Administrative Activities (Activités administratives):

Since February 2009 I was recruited as instrument scientist at the neutron source FRM 2. I am in charge of the management and the maintenance of a diffractometer (named STRESS-SPEC), and I carry out my own studies of neutron diffraction for structure, texture and stress analyses of engineering materials. I participate in hardware maintenance and upgrade, such as the slit system, the sample handling and positioning system, the detector system, the electronics, the sample environments and etc. I am involved routinely in programming for data analysis and regeneration of the instrument control software. Moreover, I am co-responsible for the management of the neutron beam time of scientific users and industrial customers as well.

My work as an instrument scientist is also extended to the outside of the neutron source FRM 2. I also participated in the work / project to construct new instruments like the BEER (Beamline for European materials Engineering Research) at ESS (European Spallation Source, Lund, Sweden), and in the commissioning of the texture diffractometer and the strain scanner at CARR (China Advanced Research Reactor, Beijing, China). This kind of participation is also realized by providing

training to PhD students or post-doctoral fellows at the STRESS-SPEC with an aim to offer them opportunities to acquire experience on instrument running.

The main activities are summarized as follows:

- Management of the maintenance of the neutron diffractometer STRESS-SPEC.
- Management of the up-to-date upgrade of the neutron diffractometer.
- Supervision of users (PhD students or researchers) for proposal writing to obtain neutron beam time.
- Users training for instrument running.
- Users training for neutron data analyses from the raw images to final results.
- Management of the required measurements from industrial customers.
- Supervision and training of the neutron instrument scientists from the cooperating institutes around the world.
- Supervision of PhD students who are possible candidates as future instrument scientist at Russia PIK reactor (Petersburg Nuclear Physics Institute).

Research activities (Activités de recherche):

During my career, research is one of my most important activities. My research competences have been constantly developed since the beginning of my doctoral study in Clausthal University of Technology in 2004. After my PhD study, I worked as post-doctoral fellow at Department of Neutron Scattering, Helmholz-Center Geesthacht in Garching where is located a fission neutron source for materials research. Owing to the specific characterization capacities of neutron scattering for materials researches, my research has been boosted since 2009 and it has led to broad scientific collaborations with universities and research institutes from both inside and outside Germany.

My research activities are mainly in two domains: research and development (R&D) of advanced light weight alloys (like Mg, Al, Ti alloys and their processing techniques) and characterization of materials by neutron scattering and synchrotron diffraction. Hereunder are some examples of my research activities in terms of **P**rojects **R**elated **T**opics (**PRT).**

PRT-1: Development of high performance light Mg alloys through advanced technologies, including new alloy systems design (e.g. micro-alloying), **s**evere **p**lastic **d**eformation techniques (**SPD**, e.g. ECAP, HPT, ARB, and etc.) and fabrication of Mg matrix composite reinforced by the addition of second ceramic phases (MMCs) or nano-particles. These were carried out under both internal cooperation with the department of **MagIC** (**Mag**nesium **I**nnovation **C**entre, HZG), and external collaboration with the Advanced Magnesium Matrix Materials Group at Harbin Institute of Technology (Harbin, China). The Sub-topics include:

- Phase /structure identification of new Mg alloys or hybrids in Mg.
- Texture and strain analyses of high plasticity Mg-RE alloys via *in-situ* tensile/ compression tests.
- Residual stress analyses and hot tearing behaviour of cast Mg alloys.
- Synthesis of high specific strength Mg matrix composites reinforced by micro and nano particles.
- Texture and micro-stress evolution of each phase of the Mg matrix composites.

The results of the topic have produced about 40 published papers (**P**rojects **R**elated **P**ublications (**PRP)**) (e.g., [1], [10], [15], [16], [18], [23], [25], [27], [32], [38], [39], etc.). Detailed projects are summarized later in the scientific review. On the above sub research topics my involvement in those projects is mainly realized by co-supervision of PhD theses, as listed later.

PRT-2: Texture and anisotropic properties characterization of engineering materials by means of advanced diffraction technologies such as neutrons and synchrotrons, and texture interpretation in relation with materials thermo-mechanical history. The sub-topics include:

- Texture of thermo-mechanically deformed **ADI** (**A**ustempered **D**uctile **I**ron) and its effect on phase quantitative.
- Structure and texture of thermo-mechanically deformed Ni-Mn-Ga ferromagnetic shape memory alloys.
- Processing process related texture gradient of semi-finished industrial products of Cu and Al alloys. Texture analysis of archaeological iron artefacts. Local or gradient texture investigations are used to reveal details that would

otherwise be inaccessible. With the texture information the manufacturing process of the ancient artefacts will be estimated.

The study in this topic has led to about 15 published papers (e.g., [4], [5], [6], [7], [7], [14], [21], [26], [30], etc.). Detailed projects are summarized later in the scientific review. My activity in this topic is a direct involvement in part of the investigation as diffraction specialist and as PhD co-supervision, as listed later.

PRT-3: Residual stress analysis of welding components using conventional welding, rotary friction welding and laser welding. Stress profiles were investigated with a strong correlation to the welding processes. The sub-topics include:

- Influence of crystallographic texture on the microstructure, tensile properties and residual stress state of laser-welded titanium joints.
- Determination of macroscopic and microscopic residual stresses in friction stir welded metal matrix composites.

This work has resulted in about 5 published papers (e.g., [2], [4], [5], [9], [18], etc.) with my direct involvement.

PRT-4: Structure and texture analyses of advanced high temperature alloys (super alloys) by neutron diffraction. The sub-topics include:

- Development of γ-TiAl based light-weight structural alloys for high-temperature applications.
- High temperature deformation behaviour of Ni super alloys.

This work have produced about 4 published papers (e.g., [22], [29], [36], [57], etc.). My involvement was as PhD co-supervisor. The PhD thesis is listed below.

PRT-5: Instrumentation and upgrade of neutron diffractometer for materials science and engineering studies, especially their sample environment development for *in-situ* or in operando analysis. The sub-topics include:

- Development of new pole figure scanning routine.
- Specified sample environment development for neutron diffractometer, such as the integration of a mechanical property test machine at room or at elevated temperatures for texture and lattice strain analyses, integration of electric field or magnetic field in diffractometer for field induced texture analyses and integration of a dilatometer with neutron diffractometer for high precision dimension measurements.

This work has produced about 10 published papers (e.g., [31], [51], [52], [60], [67], etc.). My role in this work was undertaking one part of the task.

List of research projects (Liste des projets de recherche):

With respect to the above **PRTs**, my participants in the cooperated projects are listed below.

PRT-1: (1) 'Study on the interface Strengthening and Toughening Mechanism of Carbon Nanotubes Reinforced Magnesium Matrix Composites', National Natural Science Foundation of China, chaired by Dr. Xiaojun Wang (Harbin Institute of Technology, Harbin China), 01. 2015 ~ 12. 2018.

(2) 'Investigation on Construction and Strengthening Mechanism of the CNTs/Mg Bionic Multi-layer Structures', National Natural Science Foundation of China, chaired by Dr. Xiaojun Wang (Harbin Institute of Technology, Harbin China), 01. 2017 ~ 12. 2020.

(3) 'Micro-Plastic Deformation Behavior of Pure Magnesium and its Alloys', National Natural Science Foundation of China, chaired by Prof. Mingyi Zheng (Harbin Institute of Technology, Harbin China), 01. 2013 ~ 12. 2016.

(4) 'High Performance Rare Earth Magnesium Alloys and Their Composites', Internal Cooperation Project of Ministry of Science and Technology, China, chaired by Prof. Kun Wu (Harbin Institute of Technology, Harbin China), 09. 2010 ~ 08. 2013.

(5) 'Deformation Mechanism and Damping Behaviour of Ultra-fine Grained Mg/Al Laminated Composites by Accumulative Roll Bonding Process', National Natural Science Foundation of China, chaired by Prof. Mingyi Zheng (Harbin Institute of Technology, Harbin China), 01. 2011 ~ 12. 2013.

(6) 'Mechanical Properties and Damping Mechanism of Equal Channel Angular Pressing Deformed Ultra-fine Grained Magnesium Alloy ', National Natural Science Foundation of China, chaired by Prof. Mingyi Zheng (Harbin Institute of Technology, Harbin China), 01. 2006 ~ 12. 2008.

(7) 'Preparation of High Strength Quasi-crystal Reinforced Magnesium Composites by Equal Channel Angular Pressing', chaired by Prof. Mingyi Zheng (Harbin Institute of Technology, Harbin China), 01. 2003 ~ 12. 2005.

(8) ‘Study on the interface Strengthening and Toughening Mechanism of Carbon Nanotubes Reinforced Magnesium Matrix Composites’, National Natural Science Foundation of China, chaired by Dr. Xiaojun Wang (Harbin Institute of Technology, Harbin China), 01. 2015 ~ 12. 2018.

(9) ‘Fabrication of high strength SiCp/Mg-Zn composite by microstructure optimisation’, Key Research foundation of ShanXi Province, China, in cooperation with Dr. Kunkun Deng from Taiyuan University of Science and Technology, 06.2017 ~ 06.2019.

PRT-2: (1) ‘Kinetics of Phase Transformation in Ausferritic Cast Iron (ADI)’, German Research Foundation, chaired by Prof. W. Petry and Dr. Michael Hofmann (FRM2, TU Munich, Germany), 2009-2013.

PRT-3: (1) ‘Influence of Base Metal’s Crystallographic Texture on the Mechanical Properties of Laser-Welded Titanium Joints’, German Research Foundation, Submitted in Feb. 2018.

PRT-4: (1) ‘PIK-GGBase (based on a longstanding collaboration between the neutron research centres Petersburg Nuclear Physics Institute of National Research Centre and Helmholtz-Zentrum Geesthacht)’, project leader, Prof. Martin Müller, 04. 2014 ~ 12. 2017.

PRT-5: (1) ‘Robotic System for Neutron Diffractometer’, Federal Ministry of Education and Research (BMBF, 05KN7MCA Germany), chaired by Prof. H.-G. Brokmeier (TU Clausthal), 02. 2009 ~ 12. 2013.

(2) ‘MML- From Matter to Materials & Life, topic 1: Neutron Sources for the Investigation of Condensed Matter; topic 2: Operation of the facilities’, Helmholtz Funded Program, project leader, Prof. Martin Müller, POF-III (2012 ~ 2016) and POF-V (2017 ~ 2021).

List of co-supervised theses (Liste des thèses co-dirigées):

The PhD theses related to the above **PRTs** of which I was co-supervisor are listed below. My contribution to each work is also briefly indicated.

Related to PRT-1:

(1) Cho Ding (Sep. 2013 ~ Jun. 2018), PhD student in Material Science, School of Material Science and Engineering, Harbin Institute of Technology, Harbin China.

Topic: CNTs + SiC_p hybrid reinforced magnesium matrix nano-composites: microstructure, mechanical properties and enhancement mechanism.

Thesis supervisor: Prof. Kun Wu (HIT, 50%), Co-supervisor 1: Dr. Xiaojun Wang (HIT, 30%), Co-supervisor 2: Dr. Weimin Gan (HZG, 20%).

(2) Guodong Fan, (Aug. 2010 ~ Apr. 2013), doctor of Engineering, School of Materials Science and Engineering, Harbin Institute of Technology, Harbin China

Thesis title: Research on damping and microplastic behaviour of pure Mg and Mg alloys.

Thesis supervisor: Prof. Mingyi Zheng (70%), co-supervisor 1, Prof. H.-G. Brokmeier (TU Clausthal 10%), co-supervisor 2: Dr. Weimin Gan (HZG, 20%).

(3) Zijian Yu (02. 2011 ~ 05. 2015), PhD thesis at University of Chinese Academy of Sciences (UCAS), Changchun China.

Thesis title: Investigations on microstructure and mechanical properties of a high strength Mg-11Gd-4.5Y-1Nd-1.5Zn-0.5Zr alloy.

Thesis supervisor: Prof. Meng Jian (UCAS, 70%), co-supervisor 1: Dr. Yuanding Huang (MagIC at HZG, 20%), co-supervisor 2: Dr. Weimin Gan (HZG, 10%).

(4) Jiangfeng Song (03. 2012 ~ 02. 2016), PhD thesis at Clausthal University of Technology, Clausthal-Zellerfeld Germany.

Thesis title: Hot tearing of Mg-Ca binary and Mg-Ca-Zn ternary alloys.

Thesis supervisor: Prof. DR. Babette Tonn (TU Clausthal, 50%), co-supervisor 1: Dr. Yuanding Huang (MagIC at HZG, 45%), co-supervisor 2: Dr. Weimin Gan (HZG, 5%).

(5) Yuling Xu (09. 2014 ~ 10. 2018), PhD thesis at TUHH - Technical University Hamburg, Hamburg Germany.

Thesis topic: Influence of Gd contents on its strengthening in Mg.

Thesis supervisor: Prof. DR. K.-U. Kainer (TUHH, 60%), co-supervisor 1: Dr. Yuanding Huang (MagIC at HZG, 35%), co-supervisor 2: Dr. Weimin Gan (HZG, 5%).

(6) Sihang You (09. 2015 ~ present), PhD thesis at TUHH -Technical University Hamburg, Hamburg Germany.

Thesis topic: Microstructure property relationships of as-cast and heat treated Mg-Ca-Y alloys.

Thesis supervisor: Prof. DR. K.-U. Kainer (TUHH, 50%), co-supervisor 1: Dr. Yuanding Huang (MagIC at HZG, 40%), co-supervisor 2: Dr. Weimin Gan (HZG, 10%).

Related to the PRT-2:

(7) Mr. Xiaohu Li (07. 2013 ~ 03.2018), PhD student Physics, Department of Physic, Technical University of Munich, Garching Germany.

Topic: Strain induced martensitic transformation kinetics in austempered ductile iron.

Thesis supervisor: Prof. Windfried Petry (TUM, 50%), Co-supervisor 1: Dr. Michael Hofmann (HZG, 30%), Co-supervisor 2: Dr. Weimin Gan (HZG, 20%).

Related to the PRT-3:

(8) Zhong Zhengye, (Oct. 2010 ~ Mar. 2015), doctor of Engineering, Insitute of Materials Science and Engineering, Clausthal University of Technology, Clausthal-Zellerfeld Germany.

Thesis title: *In-situ* tensile investigations on AA 7020-T6 using synchrotron diffraction for texture, lattice strain and defect density studies.

Thesis supervisor: Prof. H.-G. Brokmeier (TU Clausthal, 80%), co-supervisor: Dr. Weimin Gan (HZG, 20%).

(9) Mohammed Zakria Salih, (Sep. 2011 ~ Feb. 2014), doctor of Engineering, Insitute of Materials Science and Engineering, Clausthal University of Technology, Clausthal-Zellerfeld Germany.

Thesis title: The Effect of Magnetic Annealing on Crystallographic Texture, Microstructure and Magnetic properties Development in Fe-2.6%Si.

Thesis supervisor: Prof. H.-G. Brokmeier (TU Clausthal, 80%), co-supervisor: Dr. Weimin Gan (HZG, 20%).

(10) Nowfal Al-Hamdany, (Oct. 2011 ~ Mar. 2015), doctor of Engineering, Insitute of Materials Science and Engineering, Clausthal University of Technology, Clausthal-Zellerfeld Germany.

Thesis title: Texture and Stress Characterization of a Copper Tube by Neutron, Synchrotron and Electron Diffraction.

Thesis supervisor: Prof. H.-G. Brokmeier (TU Clausthal, 60%), co-supervisor: Dr. Weimin Gan (HZG, 40%).

Related to the PRT-4:

(11) Ms. Victoria Kononikhina (Aug. 2015 ~ present), PhD student in Metal Physics, Institute of Materials Research, Helmholtz-Zentrum Geesthacht, Geesthacht, Germany.

Topic: Investigation of ordering and disordering of β/β_o phase in TiAl alloys by neutron diffraction.

Thesis supervisor: Prof. Andreas Schreyer (HZG, 50%), Co-supervisor 1: Dr. Florian Pyczak (HZG, 20%), Co-supervisor 2: Dr. Andreas Stark (HZG, 20%), Co-supervisor 3: Dr. Weimin Gan (HZG, 10%),

Related to the PRT-5:

(12) Martin Finkel, (Sep. 2015~ Sep 2016), **master** work, Physic Department of Technical University of Munich, Garching Germany.

Thesis title: Elastic constants from multi-phase, polycrystalline materials.

Thesis supervisor: Dr. Michael Hofmann (TUM, 60%), Co-supervisor: Dr. Weimin Gan (HZG, 40%).

Scientific Outreach (Rayonnement scientifique):

- Based on the broad research activities, as first author and co-author my publication record has reached so far about 90 in open academic journals (details see the publication list below).
- Contribution to book writing,
  - Neutrons and Synchrotron Radiation in Engineering Materials Science, From Fundamentals to Applications (Second Edition), Wiley-VCH, 2017.
- Since March 2017 I am invited by CIAE (China Institute of Atomic Energy) as a consultant to supervise local staffs for texture and stress measurements and data interpretation using neutron diffractometer.

List of publications (Liste de publications)(sorted by year):

(2018)

[1] Ke Hua, Yudong Zhang, Weimin Gan, Hongchao Kou, jinshan Li, Claude Esling. Correlation between imposed deformation and transformation lattice strain α variant selection in a metastable β-Ti alloy under isothermal compression. Acta Mater. 161 (2018) 150.160).

[2] Bo Lan, T.Ben Britton, Tea-Sung Jun, Weimin Gan, Michael Hofmann, Fionn P.E. Dunne, Michael J.S. Lowe. Direction volumetric measurement of crystallographic texture using acoustic waves. Acta Mater. 159 (2019) 384-394.

[3] Bo Lan, Michael, A. Carpenter, Weimin Gan, Michael Hofmann, Fionn P.E. Dunne, Michael J.S. Lowe. Rapid measurement of volumetric texture using resonant ultrasound spectroscopy. Scripta Mater. 157 (2018) 44-48.

[4] Friedrich E. Wagner, Rupert Gebhard, Weimin Gan, Michael Hofmann. The metrallurgical texture of gold artefacts found at hte Bronze Age rampart of Bernstorf (Bavaria) studied by neutron diffraction. J. Archaeo. Sci. Rep. 20 (2018) 338-346.

[5] X.H. Li, P. Saal, W.M. Gan, M. Hoelzel, W. Volk, W. Petry, M. Hofmann. Strain-Induced martensitic transformation kinetic in austempered ductile iron. Metall. Mater. Trans. 49A (2018) 95.
[6] Nowfal Al-Hamdany, Heinz-Günter Brokmeier, Weimin Gan. Crystallographic texture and lattice strain evolution during tensile load of swaged brass. Mater. Sci. & Eng. A 711 (2018) 149-155.
[7] Nowfal Al-Hamdany, Heinz-Günter Brokmeier, Mohammed Salih, Zhengye Zhong, Bernd Schwebke, Norbert Schell, Weimin Gan. Crystallographic textue gradient along the wall thickness of an SF-copper tube. Mater. Charact. 139 (2018) 125-133.
[8] Xiaorui Liu, Benoît Beausir, Yudong Zhang, Weimin Gan, Hui Yuan, Fuxiao Yu, Claude Esling , Xiang Zhao, Liang Zuo. J. Alloys & Comp. 730 (2018) 208-218.
[9] Fangjie Mo, Erdong Wu, Changsheng Zhang, Hong Wang, Zhengye Zhong, Jian Zhang, Bo Chen, Michael Hofmann, Weimin Gan, Guangai Sun. Metal. & Mater. Intern. March (2018) 1-10.

(2017)
[10] G. Garcés, E. Oñorbe, W. Gan, K. Máthis, D. Tolnai, K. Horváth, P. Pérez, P. Adeva. Mater. Charact. 126 (2017) 116-124.
[11] V. Zinth, C.v.Lüdders, Jörn Wilhelm, Simon V. Erhard, Michael Hofmann, Stefan Seidlmayer, Joana Rebelo-Kornmeier, Weimin Gan, Andreas Jossen, Ralph Gilles. J. of Powder Soures, 361 (2017) 54-60.
[12] Yong Hu, Zongbin Li, Bo Yang, Suxin Qian, Weimin Gan, Yuanyuan Gong, Yang Li, Dewei Zhao, Jian Liu, Xiang Zhao, Liang Zuo, Dunhui Wang, Youwei Du. APL Mater. 5 (2017) 46103.
[13] Jiangkun Fan, Jinshan Li, Yudong Zhang, Hongchao Kou, Jaafar Ghanbaja, Weimin Gan, Lionel Germain and Claude Esling. J. Appl. Cryst. 50 (2017) 795-804.
[14] Ke Hua, Yudong Zhang, Hongchao Kou, Jinshan Li, Weimin Gan, Jean-Jacques Fundenberger, Claude Esling. Acta. Mater. 132 (2017) 307-326.
[15] G. Garcés, E. Oñorbe, W. Gan, K. Máthis, D. Tolnai, K. Horváth, P. Pérez, P. Adeva. Mater. Charact. 15 (2017) 364-378.
[16] Zijian Yu, Yuanding Huang, Weimin Gan, Zhengye Zhong, Norbert Hort, Jian Meng. J. Mater. Sci. 52 (2017) 6670-6686.
[17] Weimin Gan, Michael Hofmann, Volker Ventzke, Christian Randau, Yuanding Huang, Armin Kriele, Heinz-Guenter Brokmeier. Microstructure and residual stress in rotary friction welded dissimilar metals of AA7020-T6/316L. Mater. Sci. Forum. 879 (2017) 572-577.
[18] Weimin Gan, Yuanding Huang, Yuling Xu, Michael Hofmann, Karl Kainer, Nober Hort. In Situ Tensile texture Analysis of a new Mg-RE alloy. Mater. Sci. Forum. 879 (2017) 779-783.
[19] Rebelo Kornmeier J., Gan, W.M., Marques, M. J., Castanhola Batista A., Hofmann M., Loureiro A. Texture characterization of stainless steel cladded layers of process vessels. Mater. Sci. Forum. 879(2017) 1588-1593.
[20] X.X. Zhang, D.Wang, B.L. Xiao, H. Andrä, W.M. Gan, M.Hofmann, Z.Y.Ma. Enhanced multiscale modeling of macroscopic and microscopic residual stresses evolution during multi-thermo-mechanical processes. Materials and Design 115 (2017) 364-378.
[21] Zongbin Li, Bo Yang, Naifu Zou, Yudong Zhang, Claude Esling, Weimin Gan, Xiang Zhao, Liang Zuo. Materials. 10 (2017).(doi:10.3390/ma10050463).
[22] Victoria Kononikhina, Andreas Stark, Weimin Gan, Andreas Schreyer. Ordering and disordering of β/β_o-phase in γ-TiAl based alloys investigated by neutron diffraction. Mater Res Soc Symp Proc. (2017).
[23] Chang Hai, Zheng Mingyi, Heinz Guenter Brokmeier, Gan Weimin. Interface characterization of the Mg/Al laiminated composite fabricated by accumulative roll bonding at ambient temperature. ACTA Metel. Sinca (in Chinese), 53 (2017) 220-1226.

(2016)
[24] Emad Maawad, Weimin Gan, Michael Hofmann, Volker Ventzke, Stefan Riekehr, Heinz-Günter Brokmeier, Nicoklai Kashaev, Martin Müller. Influence of crystallographic texture on

the microstructure, tensile properties and residual stress state of laser-welded titanium joints. Materials & Design. 101 (2016)137-145.
[25] Zijian Yu, Yuanding Huang, Weimin Gan, Chamini Lakshi Mendis, Zhengye Zhong, Heinz Günter Brokmeier, Norbert Hort, Jian Meng. Microstructure evolution of Mg–11Gd–4.5Y–1Nd–1.5Zn–0.5Zr (wt%) alloy during deformation and its effect on strengthening. Materials Science & Engineering A657 (2016) 259-268.
[26] X H Li, P Saal, W M Gan, M Landesberger, M Hoelzel, M Hofmann. Strain Induced Martensitic Transformation in Austempered Ductile Iron (ADI). Journal of Physics: Conference Series 746 (2016) 012055.
[27] Yuanding Huang, Lei Yang, Sihang You, Weimin Gan, Karl Ulrich Kainer, Norbert Hort. Unexpected formation of hydrides in heavy rare earth containing magnesium alloys. Journal of Magnesium and Alloys 4 (2016) 173-180.
[28] X.G. Qiao, T. Ying, M.Y. Zheng, E.D. Wei, K.Wu, X.S. Hu, W.M. Gan, H.G. Brokmeier. I.S. Golovin. Microstructure evolution and mechanical properties of nano-SiCp/AZ91 composite processed by extrusion and equal channel angular pressing (ECAP). Materials Characterization 121 (2016) 222-230.
[29] C. Turk, H. Leitner, G.Kellezi, H.Clemens, W.M.Gan, P.Staron, S.Primig. Impact of the B2 ordering behaviour on the mechanical properties of a FeCoMo alloy. Materials Science & Engineering A662 (2016) 511-518.
[30] Zongbin Li , Naifu Zou , Bo Yang , Weimin Gan, Long Hou, Xi Li, Yudong Zhang, Claude Esling, Michael Hofmann, Xiang Zhao, Liang Zuo. Effect of compressive load on the martensitic transformation from austenite to 5M martensite in a polycrystalline Ni–Mn-Ga alloy studied by *in-situ* neutron diffraction. Journal of Alloys and Compounds. 666 (2016) 1-9.

(2015)
[31] C. Randau, H.G. Brokmeier, W.M. Gan, M. Hofmann, M. Voeller, W. Tekouo, N. Al-hamdany, G. Seidl, A. Schreyer. Improved sample manipulation at the STRESS-SPEC neutron diffractometer using an industrial 6-axis robot for texture and strain analyses. Nuclear Instruments and Methods in Physics Research, A 794 (2015) 67-75.
[32] G. Garces, P. Perez, S. Cabeza, H.K. Lin, S. Kim, W. Gan, P. Adeva. Reverse tension/compression asymmetry of a Mg–Y–Zn alloys containing LPSO phases. Materials Science & Engineering A647 (2015) 287- 293.
[33] X.X. Zhang, D.R. Ni, B.L. Xiao, H. Andrae, W.M. Gan, M. Hofmann, Z.Y. Ma. Determination of macroscopic and microscopic residual stresses in friction stir welded metal matrix composites via neutron diffraction. Acta Materialia 87 (2015) 161-173.
[34] M.Z. Salih, M.U hlarz, F. Pyczak, H.-G. Brokmeier, B. Weidenfeller, N.Al-hamdany, W.M. Gan, Z.Y. Zhong, N. Schell. The effect of magnetic annealing on crystallographic texture and magnetic properties of Fe-2.6% Si. J. of Magnetism and Magnetic Materials 381 (2015) 350-359.
[35] N Al-Hamdany, WM Gan, C Randau, H-G Brokmeier, M Hofmann. Diffraction on heavy samples at STRESS-SPEC using a robot system. IOP Conf. Series: Materials Science and Engineering 82 (2015) 012105.
[36] Christoph Turk, Gert Kellezi, Harald Leitner, Peter Staron, Weimin Gan, Helmut Clemens, Sophie Primig. B2 order transformation in a Fe-25 at% Co-9 at% Mo alloy. Mater. Res. Soc. Symp. Proc. Vol. 1, 2015.
[37] LIU Mengying, CHANG Hai, XU Feng , XU Zhengfang, YANG Zhao, WANG Ning , GAN Weimin, FENG Qiang. MICROSTRUCTURE EVOLUTION AND MECHANICAL PROPERTIES OF TC1 ALLOY FABRICATED BY PLASMA ARC COLD HEARTH MELTING DURING ROLLING PROCESS. ACTA METALLURGICA SINICA (in Chinese). 51 (2015) 341-348.

(2014)
[38] W.M. Gan, Y.D. Huang, R. Wang, G.F. Wang, A. Srinivasan, H.-G. Brokmeier, N. Schell, K.U. Kainer, N. Hort. Microstructures and mechanical properties of pure Mg processed by rotary swaging. Materials and Design 63 (2014) 83-88.

[39] Weimin Gan, Yuanding Huang, Zhi Wang, Norbert Hort, Michael Hofmann. Residual stresses near the hot sprues of as-cast Mg-Zn alloys investigated by STRESS-SPEC neutron diffractometer. Materials Science Forum Vols. 768-769, 428-432 (2014).
[40] Zongbin Li, Yudong Zhang, Claude Esling, Weimin Gan, Naifu Zou, Xiang Zhao, Liang Zuo. *In-situ* neutron diffraction study of martensitic variant redistribution in polycrystalline Ni-Mn-Ga alloy under cyclic thermo-mechanical treatment. APPLIED PHYSICS LETTERS 105, 021907 (2014). .
[41] Xiao Guang Qiao, YaWei Zhao, WeiMin Gan, Ying Chen, MingYi Zheng, Kun Wu, Nong Gao , Marco J. Starink. Hardening mechanism of commercially pure Mg processed by high pressure torsion at room temperature. Materials Science & Engineering A619 (2014) 95-106.
[42] N. Al-hamdany, H.-G. Brokmeier, C. Randau, W. M. Gan, M. Voeller. Texture gradient studies of a Cu-tube by the robot at STRESS-SPEC. Cryst. Res. Technol., 1-11 (2014). DOI 10.1002/crat.201400229.
[43] Rong-chang ZENG, Wolfgang DIETZEL, Rudolf ZETTLER, Wei-min GAN, Xin-xin SUN. Microstructural evolution and delayed hydride cracking of FSW-AZ31 magnesium alloy during SSRT. Trans. Nonferrous Met. Soc. China 24 (2014) 3060-3069. DOI: 10.1016/S1003-6326(14)63443-9.
[44] Song Jiangfeng, DIERINGA Hajo, HUANG Yuanding, GAN Weimin, KAINER Karl Ulrich, HORT Norbert. Mechanical Properties and Microstructures of Nano SiC Reinforced ZE10 Composites Prepared with Ultrasonic Vibration. Advanced Materials Research Vol. 1019 (2014) pp 169-176.
[45] Jiangfeng Song, Yuanding Huang, Karl Ulrich Kainer, Weimin Gan, Norbert Hort. Residual stresses of the as-cast Mg-xCa alloys with hot sprues by neutron diffraction. Advanced Materials Research Vol. 996 (2014) pp 592-597. doi:10.4028/www.scientific.net/AMR.996.592.
[46] M.Z. Salih, B. Weidenfeller, N. Al-hamdany, H.-G. Brokmeier, W.M. Gan. The effect of intermediate annealing between cold rolled steps on crystallographic texture and magnetic properties of Fe-2.6% Si. Journal of Magnetism and Magnetic Materials 362 (2014) 141-149. http://dx.doi.org/10.1016/j.jmmm.2014.03.009.
[47] M.Z. Salih, B. Weidenfeller, N. Al-hamdany, H.-G. Brokmeier, W.M. Gan. Magnetic properties and crystallographic textures of Fe 2.6% Si after 90% cold rolling plus different annealing. Journal of Magnetism and Magnetic Materials, 354, 105-111 (2014).
[48] E. Maawad, H.-G. Brokmeier, L. Wagner, M. Hofmann, W.M. Gan, Ch. Genzel, M.Klaus. Non-destructive residual stress evaluation in mechanically surface treated Ti–2.5Cu by diffraction techniques. NDT&E International 61 (2014) 67-70. http://dx.doi.org/10.1016/j.ndteint.2013.10.002.
[49] Yuanding Huang, Weimin Gan, Karl Ulrich Kainer, Norbert Hort. Role of multi-microalloying by rare earth elements in ductilization of magnesium alloys. Journal of Magnesium and Alloys 2 (2014) 1-7. http://dx.doi.org/10.1016/j.jma.2014.01.005.

(2013)

[50] W.M. Gan, Y.D. Huang, R. Wang, Z.Y. Zhong, N. Hort, K.U. Kainer, N. Schell, H.-G. Brokmeier, A. Schreyer. Bulk and local textures of pure magnesium processed by rotary swaging. Journal of Magnesium and Alloys 1 (2013) 341-345. http://dx.doi.org/10.1016/j.jma.2013.12.004.
[51] M. Hoelzel, W. M. Gan, M. Hofmann, C. Randau, G. Seidl, Ph. Juettner, W.W. Schmahl. Rotatable multifunctional load frames for neutron diffractometers at FRM II-design, specifications and applications. Nuclear Instruments and Methods in Physics Research. A 711 (2013) 101-105.
[52] M. Hofmann, W. M. Gan, J. Rebelo-Kornmeier, M. Schöbel. Materials science at the diffractometer STRESS-SPEC at FRM II. Neutron News, 24:3, 14-17 (2013).
[53] G. D. Fan, M. Y. Zheng, C. H. Ju, X. S. Hu, K. Wu, W. M. Gan, H. G. Brokmeier. Effect of grain size on cyclic microplasticity of ECAP processed commercial pure magnesium. J Mater Sci (2013) 48: 1239-1248.

[54] G.D. Fan, M.Y.Zheng, X.S.Hu, K.Wu, W.M. Gan, H.-G. Brokmeier. Internal friction and microplastic deformation behavior of pure magnesium processed by equal channel angular pressing. Materials Science & Engineering, A 561 (2013) 100-108.
[55] L.B. Tong, M.Y. Zheng, D.P. Zhang, W.M. Gan, H.-G. Brokmeier, J. Meng, H.J. Zhang. Compressive deformation behavior of Mg-Zn-Ca alloy at elevated temperature. Materials Science & Engineering, A586 (2013) 71-77.
[56] Chang Hai, Zheng Mingyi, Gan Weimin, Xu Chao, H. G. Brokmeier. Texture Evolution of the Mg/Al Laminated Composite by Accumulative Roll Bonding at Ambient Temperature. Rare Metal Materials and Engineering, Volume 42, Issue 3, March 2013.
[57] T.A. Krol, C. Seidel, J. Schilp, M. Hofmann, W. Gan, M.F. Zaeh. Verification of structural simulation results of metal-based additive manufacturing by means of neutron diffraction. Physics Procedia 41, (2013) 842 - 850.

(2012)
[58] Weimin Gan, Yuanding Huang, Lei Yang, Karl Ulrich Kainer, Miao Jiang, Heinz-Günter Brokmeier and Norbert Hort. Identification of unexpected hydrides in Mg–20 wt% Dy alloy by high-brilliance synchrotron radiation. J. Appl. Cryst. (2012). 45, 17-21.
[59] W. M. Gan, C Randau, M Hofmann, H G Brokmeier, M Mueller, A. Schreyer. Peak broadening and peak shift pole figures investigations by STRESS-SPEC diffractometer at FRM II. Journal of Physics: Conference Series. 340 (2012) 012100.
[60] Heinz-Günter Brokmeier, Christian Randau, Weimin Gan, Michael Hofmann, Thomas Lippmann, Norbert Schell. Investigation of texture gradients of semi-finished products by neutrons and photons. Materials Science Forum. Vols. 702-703 (2012) pp 499-506.
[61] Deng K. K., Wang X.J., Wu Y. W., Hu X. S., Wu K., Gan, W. M. Effect of particle size on microstructure and mechanical properties of SiCp/AZ91 magnesium matrix composite. Materials Science and Engineering a-Structural Materials Properties Microstructure and Processing Volume: 543 Pages: 158-163 Published: MAY 1 2012.

(2011)
[62] H.-G. Brokmeier, W.M.Gan, C.Randau, M.Voeller, J.Rebelo-Kornmeier, M.Hofmann. Texture analysis at neutron diffractometer STRESS-SPEC. Nuclear Instruments and Methods in Physics Research. A 642 (2011) 87-92.
[63] Weimin Gan, Heinz-Guenter Brokmeier, Mingyi Zheng, Kun Wu. Textures in multi-directional forged Mg by neutron diffraction. Advanced Materials Research. Vols. 146-147 (2011) pp. 879-882.
[64] K.K. Deng, X.J. Wang, W.M. Gan, Y.W. Wu, K.B. Nie, K. Wu, M.Y. Zheng, H.G. Brokmeier. Isothermal forging of AZ91 reinforced with 10 vol.% silicon carbon particles. Materials Science and Engineering, A 528 (2011) 1707-1712.
[65] L.B. Tong, M.Y. Zheng, S.W. Xu, S. Kamado, Y.Z. Du, X.S. Hu, K. Wu, W.M. Gan, H.G. Brokmeier, G.J. Wang, X.Y. Lv. Effect of Mn addition on microstructure, texture and mechanical properties of Mg-Zn-Ca alloy. Materials Science and Engineering. A 528 (2011) 3741-3747.

(2010)
[66] W.M. Gan, E. Maawad, H. Chang, G.D. Fan, C. Randau, M.Y. Zheng, K. Wu, H.-G. Brokmeier. Effect of texture on damping behaviour in an AZ80 alloy. Solid State Phenomena Vol. 160 (2010) pp 117-121.
[67] H.-G. Brokmeier, C. Randau, W. Tekouo, M. Hofmann, W. Gan, M. Müller, A. Schreyer, W. Petry. The Robot Concept at STRESS-SPEC for the Characterisation or Semi-Finished Products. Materials Science Forum. Vol. 652 (2010) pp 197-201.
[68] H.-G. Brokmeier, H. Chang, W.M. Gan, M.Y. Zheng, K. Wu. Texture development of ARB processed Mg/Al multilayers. Journal of Physics: Conference Series. 240 (2010) 012125.
[69] H. Chang, M.Y. Zheng, K. Wu, W.M. Gan, L.B. Tong, H.-G. Brokmeier. Microstructure and mechanical properties of the accumulative roll bonded (ARBed) pure magnesium sheet.

Materials Science and Engineering. A 527 (2010) 7176-7183.
[70] K. Wu, H. Chang, E. Maawad, W.M. Gan, H.G. Brokmeier, M.Y. Zheng, Microstructure and mechanical properties of the Mg/Al laminated composite fabricated by accumulative roll bonding (ARB). Mater. Sci. Eng. A 527 (2010) 3073-3078.
[71] C. Xu, M.Y. Zheng, H. Chang, X.S. Hu, K. Wu, W.M. Gan, H-G. Brokmeier. Microstructure and Properties of Pure Mg/ZK60 Laminate Processed by Accumulative Roll Bonding. Materials Science Forum Vol. 650 (2010) pp 343-346.
[72] K.K. Deng, K. Wu, X.J. Wang, Y.W. Wu, X.S. Hu, M.Y. Zheng, W.M. Gan, H.G. Brokmeier. Microstructure evolution and mechanical properties of a particulate reinforced magnesium matrix composites forged at elevated temperatures. Materials Science and Engineering. A 527 (2010) 1630-1635.
[73] J. Zurbitu, R. Santamarta, C. Picornell, W.M. Gan, H.-G. Brokmeier, J. Aurrekoetxea. Impact fatigue behavior of superelastic NiTi shape memory alloy wires. Materials Science and Engineering. A 528 (2010) 764-769.

(2009)
[74] W. M. Gan, K. Wu, M.Y. Zheng, X. J. Wang, H. Chang, H.-G. Brokmeier. Microstructure and Mechanical Property of the ECAPed Mg_2Si/Mg Composite. Materials Science and Engineering A, 516 (2009) pp 283-289.
[75] W.M. Gan, H.-G. Brokmeier, C. Randau, M.Y. Zheng, H. Chang, G.D. Fan, K. Wu. Textures at deformation region of an ECAP processed Mg by synchrotron diffraction. Proceedings of the 8th International Conference on Magnesium Alloys and Their Applications, Weimar Germany, Edited by K.U. Kainer, Wiley-VCH (2009) pp 282-287.
[76] W.M. Gan, M.Y. Zheng, H. Chang, X.J. Wang, X.G. Qiao, K. Wu, B. Schwebke, H.-G. Brokmeier. Microstructure and tensile property of the ECAPed pure magnesium. Journal of Alloys and Compounds, 470 (2009) pp 256-262.
[77] H. Chang, M.Y. Zheng, W.M. Gan, K. Wu, E. Maawad, H.G. Brokmeier. Texture evolution of the Mg/Al laminated composite fabricated by the accumulative roll bonding. Scripta Materialia, Vol. 61 (2009) 717-720.

(2008)
[78] W.M. Gan, H.-G. Brokmeier, M.Y. Zheng, H. Chang, X.J. Wang, K. Wu. Comparison of microstructure and texture development of ECAPed pure Mg with Mg-Si alloy. Achives of Metallurgy and Materials, Vol. 53, Issue 1 (2008) pp 63-68.
[79] W.M. Gan, H.-G. Brokmeier, H.Chang, M.Y.Zheng, K. Wu. Texture gradient in a single pass ECAPed pure Mg by neutron radiation. Materials Science Forum, Vols. 584-586 (2008) pp 513-517.
[80] H.-G. Brokmeier, W. Gan, M. Zheng, Z. Zuberova, Y Estrin. Development of extrusion and rolling textures during ECAP of Mg alloys. Materials Science Forum, Vols. 584-586 (2008) pp 748-753.
[81] M. Y. Zheng, S. W. Xu, W. M. Gan, K. Wu, S. Kamado, Y. Kojima, H-G. Brokmeier. Compressive behavior of ultrafine-grained Mg-Zn-Y-Zr alloy containing quasicrystalline phase. Materials Science Forum, Vols. 584-586 (2008) pp 287-292.
[82] X.J. Wang, X.S. Hu, K. Wu, K.K. Deng, W.M. Gan, C.Y. Wang, M.Y. Zheng. Hot deformation behavior of SiCp/AZ91 magnesium matrix composite fabricated by stir casting. Materials Science and Engineering. A 492 (2008) 481-485.
[83] R.E. Bolmaro, V.L. Sordi, M. Ferrante, WeiMin Gan, H.-G. Brokmeier. CUBE TEXTURE DUE TO DYNAMIC RECRYSTALLIZATION IN Pb AND Pb-62 % Sn ALLOYS UNDER EQUAL CHANEL ANGULAR EXTRUSION PROCESSING. ICOTOM- 15th International Conference on the Textures of Materials, March 2008.

(2007)
[84] Muhammad Shahzad, Dan Eliezer, Weimin Gan, Sangbong Yi, Lothar Wagner. Influence of Extrusion Temperature on Microstructure, Texture and Fatigue Performance of AZ80 and ZK60 Magnesium alloys. Materials Science Forum, Vols. 561-565 (2007) pp 187-

190.
[85] ShiWei XU, MingYi ZHENG, XiaoGuang QIAO, WeiMin GAN, Kun WU, Shigeharu KAMADO, Yo. KOJIMA. Microstructure and Tensile Properties of a Mg-Zn-Y-Zr Alloy Containing Quasicrystal Phase Processed by Equal Channel Angular Pressing. Key Engineering Materials, Vols. 353-358 (2007) pp 595-598.
[86] X.S. Hu, K. Wu, M.Y. Zheng, W.M. Gan, X.J. Wang. Low frequency damping capacities and mechanical properties of Mg-Si alloys. Materials Science and Engineering, A452-453 (2007) pp 374-379.
[87] X.J. Wang, K. Wu, H.F. Zhang, W.X. Huang, H. Chang, W.M. Gan, M.Y. Zheng, D.L. Peng. Effect of hot extrusion on the microstructure of a particulate reinforced magnesium matrix composite. Materials Science and Engineering, A 465 (2007) pp 78-84.

(2006)
[88] Weimin Gan, Mingyi Zheng, Xiaoguang Qiao, Shiwei Xu, Xiaoshi Hu, Ku Wu, H.-G. Brokmeier, Bernd Schwebke, Andreas Schreyer, Karl Ulrich Kainer. Texture Development in Different Routes EAP Processed Mg-Si Alloys by Neutron Diffraction. Proceedings of the 7th International Conference on Magnesium Alloys and Their Applications, Edited by K.U. Kainer, Wiley-VCH, (2006) pp 529-534.
[89] M. Y. Zheng, S. W. Xu, X. G. Qiao, W.M. Gan, K. Wu, S. Kamado, Y. Kojima, H.-G. Brokmeier. Equal Channel Angular Pressing of Magnesium Alloy Containing Quasicrystal Phase. Materials Science Forum. Vols. 503-504 (2006) pp 527-532.

(2005)
[90] Gan Weimin, Wu Kun, Li Shubo, Zheng Mingyi. High temperature compressive deformation behaviors of extruded AZ91 magnesium alloy. Trans. Nonferrous Met. Soc. China, Vol. 15 (2005) pp 288-292.
[91] S. B. Li, W.M. Gan, M. Y. Zheng, K. Wu. Compressive deformation behavior of the SiCw/AZ91 composite at elevated temperatures. Materials Science Forum, Vols. 488-489 (2005) pp 783-786.
[92] S. B. Li, M. Y. Zheng, W. M. Gan, K. Wu. Hot Deformation Behavior of Sicw/AZ91 Magnesium Matrix Composite in Compression. Materials Science Forum, Vols. 475-479 (2005) pp 893-896.
[93] W. M. Gan, M. Y. Zheng, S. B. Li, K. Wu. Compressive behavior of extruded SiCw/AZ91 at temperatures close to and above the solidus of the matrix alloy. Materials Science Forum. Vols. 488-489 (2005) pp. 827-830.
[94] M.Y. Zheng, X. G. Qiao, S. W. Xu, W. M. Gan, K. Wu, S. Kamado, Y. Kojima, H. G. Brokmeier. Effect of hot extrusion on microstructure and mechanical properties of quasicrystal-reinforced Mg-Zn-Y alloy. Transactions of Nonferrous Metals Society of China. 2005, 15(4): 715-721.
[95] S. B. Li, W. M. Gan, M. Y. Zheng, K. Wu. Microstructure evolution of SiCw/AZ91 magnesium matrix composite during high temperature deformation. Trans. Nonferrous Met. Soc. China, 2005, 15(s2): 245-250.

II. Scientific work

Microstructure and stress characterization of engineering materials by advanced neutron diffraction

Introduction

The main scientific results are stemming from my research activities in the fields of microstructure characterization by advanced neutron diffraction on structure, texture /anisotropy and strain/stress of the engineering materials. With first a brief introduction to an improved pole figure scanning routine developed at STRESS-SPEC for better data quality and fast measurement via modern robotics; then taking the advantage of neutrons with high penetration the combined study of bulk texture have been shown in relation to residual stress (on welding components), and other advantages of neutron diffraction for flexible sample environment series of *in-situ* studies on texture evolution (lightweight Mg alloy) and phase/structure transition (Ni-Mn-Ga and Ti alloy) under thermo-mechanical deformation are thereafter detailed.

1. Improved pole figure measurement by neutron diffraction

In the last decades, there have been significant advances in texture measurement techniques and analyzing software. Various texture measuring techniques, from laboratory machines to large facilities has been used for many years. By comparing the characteristics of each method, neutron diffraction is favored for a large sample volume and coarse-grained materials, for averaging over texture gradients for a direct correlation to macroscopic materials behavior as well as for multi-phase gradient materials. Synchrotron diffraction is favored for global textures on a small volume scale and for fast in situ experiments. The high penetration power of neutrons, the high-energy X-rays into solid matter and a high freedom to install various devices, e.g. furnace or loading devices, directly in the beam line allow a wide range of possibilities for in situ texture analysis under different sample conditions.

Nearly 30 years after the discovery of neutron by Chadwick [1.1], the first neutron diffraction texture measurement was carried out by Brockhouse [1.2]. As a consequence of the behavior of neutrons when interacting with material [1.3], neutron diffraction became an additional diffraction technique to X-ray or electron diffraction. Bunge combined neutron texture measurements on Cu-sheet firstly with a newly developed quantitative texture described by the orientation distribution function (ODF) based on the harmonic method [1.4]. Since that time neutron diffraction became a standard method in bulk texture analysis producing highest quality ODF data compared to all the other methods. Today, neutron diffraction is a standard method in a large variety of investigations in physics, chemistry, materials and geological science. Pole figure measurement by neutron diffraction is similar to standard X-ray texture diffraction measurement and is to obtain the variation of diffracted

intensities for about 1368~32400 sample orientations. However, due to the high penetration power of neutrons complete pole figures are obtained. For that reason neutron pole figures are of the highest quality and normalisation can be done directly by integrating over complete pole figures.

The instrument STRESS-SPEC supports two methods for pole figure scanning [1.5]. Firstly, a step scan mode which allows running sample rotation φ in constant steps Δφ from 0° to 360°, as shown in **Fig. 1.1** (a) with a constant grid of 5º×5º. At any tilt angle χ step width in Δφ can be adapted to the texture sharpness. The area detector allows any step width in Δχ for data evaluation. Equal angular scans as well as equal area scans are possible. Secondly, continuous scanning along φ is implemented comparable to spiral scanning using conventional X-rays. A schematic illustration of continuous scanning method is shown in **Fig. 1.1** (b). Continuous scanning has the advantage for eliminating positioning time and for STRESS-SPEC the total counting time can be reduced to 30%. Furthermore, continuous rotation guarantees that all crystallites contribute, which is not the case for most pole figure scanning routines in other diffractometers. Related to rotation speed and detector readout time, the data storage can be accomplished with every 1° in φ rotation or as desired by the user. It should be noticed that the newly implemented robot system offers more freedom to optimize the rotation speed and also to combine pole figure measurement with x, y, z scanning (texture mapping) [1.6]. Number of tilt positions in χ depends on the 2θ angle, the radii of the Debye-Scherrer rings and the sample to detector distance. Due to the sample composition and the sample to detector distance, a number of pole figures can be measured simultaneously as shown for Mg-Al composite in **Fig. 1.2**.

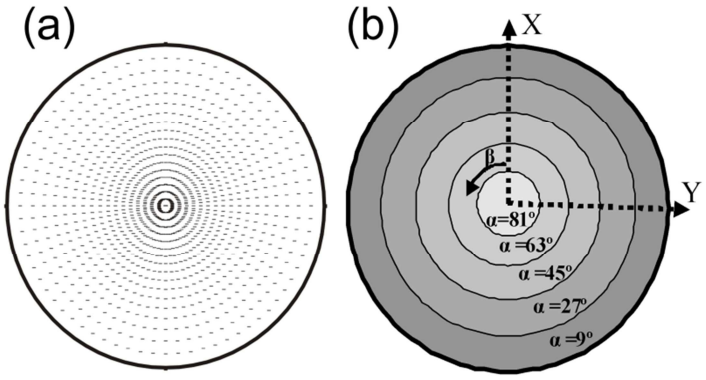

Fig. 1.1 Schemes of pole figure scan with (a) discrete method using an equal angular 5º ×5º and (b) with discrete steps in χ (0~90º) and continuous scanning of φ (0~360º).

A software package StressTexCalculator (STECA) has been developed which allows extracting pole figure data for intensity pole figures (crystallographic texture), for peak position pole figures (macro strain) or for peak broadening pole figures (micro strain) and to construct diffraction patterns (phase analysis) as well as strain profile patterns as function of x, y, z (strain mapping) [1.7].

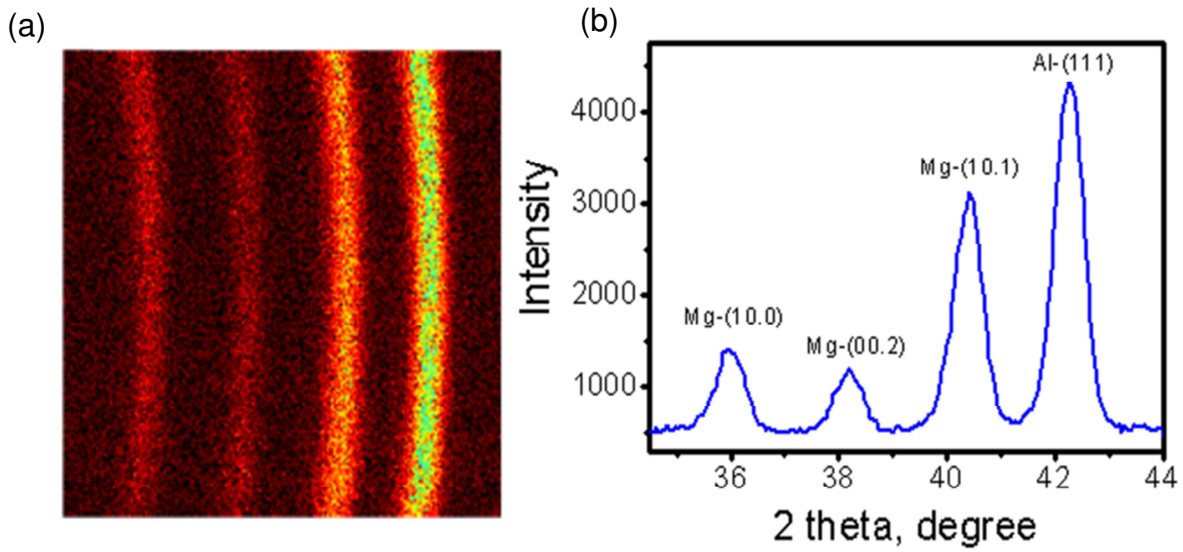

Fig. 1.2 (a) Detector image of an Mg/Al composite including Mg (10.0), Mg (00.2), Mg (10.1); (b) Diffraction pattern related to (a).

Recently, we have successfully developed a robot based sample handling and positioning system at modern large scale facilities which offers more flexible options such as to run an automatic sample changer (**Fig. 1.3** (a)), to combine residual strain and texture analyses on complex or large industry component (**Fig. 1.3** (b)) [1.8], and to install a sample environment (e.g. electric field, furnace, etc.) for *in-situ* pole figure measurement (**Fig. 1.3** (c)), etc. [1.9]. With an implementation of a laser or a video camera control system, the target positioning accuracy of the robot system can reach ~ 100 µm which is enough for bulk texture analysis. A planned upgrading to improve the robot position accuracy to ~30 µm is on-going. Application of the robotic technique is also attractive for the modern spallation source which has much high flux and can realize fast texture analysis in minute range. It is easy to combine texture and strain analyses as well.

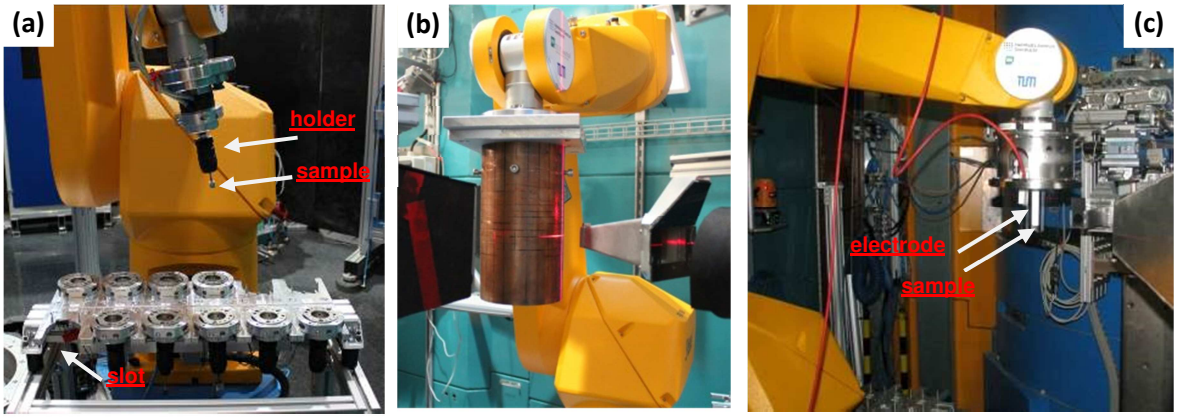

Fig. 1.3 Applications of the robot based system at STRESS-SPEC: (a) an automatic sample changer with 12 storage slots; (b) combined texture and strain analyses on a commercial 15 kg Cu tube; (c) pole figure measurement under electric field.

Reference:

[1.1] J. Chadwick, Proc. Roy. Soc. A136 (1932) 692-708.

[1.2] B. N. Brockhouse, Can. J. Phys. 31 (1953) 339-355.

[1.3] G. E. Bacon, Neutron Diffraction, third ed., Clarendon Press, Oxford, 1975.

[1.4] H. J. Bunge, C. Esling, Quantitative Texture Analysis, 1982.

[1.5] H.-G. Brokmeier, W.M. Gan, C. Randau, M. Voeller, J. Rebelo-Kornmeier, M. Hofmann. Nucl. Instr. & Meth. in Phy. Res. A 642 (2011) 87-92.

[1.6] C. Randau, H.G. Brokmeier, W.M. Gan, M. Hofmann, M. Voeller, W. Tekouo, N. Al-hamdany, G. Seidl, A. Schreyer. Nucl. Instr. & Meth. in Phy. Res. A 794 (2015) 67-75.

[1.7] C. Randau, U. Garbe, H.-G. Brokmeier. J. Appl. Cryst. 44 (2011) 641-646.

[1.8] H.-G. Brokmeier, C. Randau, W. Tekouo, M. Hofmann, W. Gan, M. Müller, A. Schreyer, W. Petry. Mater. Sci. Forum. 652 (2010) 197-201.

[1.9] N. Al-Hamdany, W.M. Gan, C. Randau, H-G. Brokmeier, M. Hofmann. IOP Conf. Series: Mat Sci. & Eng. 82 (2015) 012105.

2. Combined local texture and residual stress analysis of an RFWed Al7020/316L steel rod

2.1 Introduction

RFW- **R**otary **F**riction **W**elding, a solid state joining technique in which the welding temperature is below the melting point, is widely applied to weld dissimilar materials. No additional filler material is used and the welding takes place in the solid phase during RFW, i.e. no macroscopic melting is observed [2.1]. Since there is nearly no limitation to weld any metals, the use of RFW for joining dissimilar materials has considerably been increased over the years, mainly in the aerospace industry. Here conventional structures made of steel have been replaced by lightweight materials, such as Al, Ti, and even Mg alloys [2.2]. Plastic deformation can occur during joining especially in dissimilar materials which have large differences in yield strength. In addition, due to the different thermal expansion coefficients of the two metals in a dissimilar weld, large residual stresses develop in the RFW process, which might influence the properties in the real service. To study the local texture of an RFWed Al7020/316L austenitic steel with a dimension of Ø25×160 mm using a conventional Eulerian cradle in non-destructive way is very difficult due to its spatial limitation. But this can be easily handled by the robot system at STRESS-SPEC. The measured gauge volume was 2×2×2 mm^3. The residual strain can also be measured without changing the setup [2.3].

2.2 Texture distribution

Fig. 2.1 shows the texture evolution of positions A, B and C of Al7020, respectively. There exist two strong deformation components of Brass {110} <112> and Copper {112} <111> at the matrix material (position C); and a weak recrystallized Goss {110} <100> component as well. While at position B the maximum intensity of the pole figure (111) was decreased into nearly half with the similar intensity of Goss component. It is clear that the above three components are nearly destroyed at position A. An interesting phenomenon was the appearance of a weak rotated Cube which is a typical shear component in *fcc* materials [2.4]. This suggested a plastic deformation of the Al7020 during stir welding.

2.3 Residual stress mapping

Fig. 2.2 shows the 2D residual strain maps of a half rod at a region around the weld. The black dots in the graph depict the measurement positions. Residual stresses of both hoop and axial demonstrate a similar variation from the surface to the weld line. In the Al alloy (Al7020) tensile stresses develop from about 10 mm before the weld zone and increase to

about 250 MPa at the weld line, approaching the yield strength of the material. These tensile stresses are balanced by the compressive residual stress on the steel (316L) side reaching almost ~200 MPa. They gradually decrease to nearly 0 MPa at distance of 20 mm to the weld Line on the 316L side. A relatively high tensile residual stress (~250 MPa) in the AA7020-T6 Al is in-homogeneously distributed within 2 mm to the weld line. This should result from the fast plastic deformation. The maximum tensile residual stress is relatively high for aluminium alloy and could easily initiate crack or contribute to the propagation of crack in real service. Decreasing this tensile residual stress would require further optimisation of welding parameters or subsequent heat treatments.

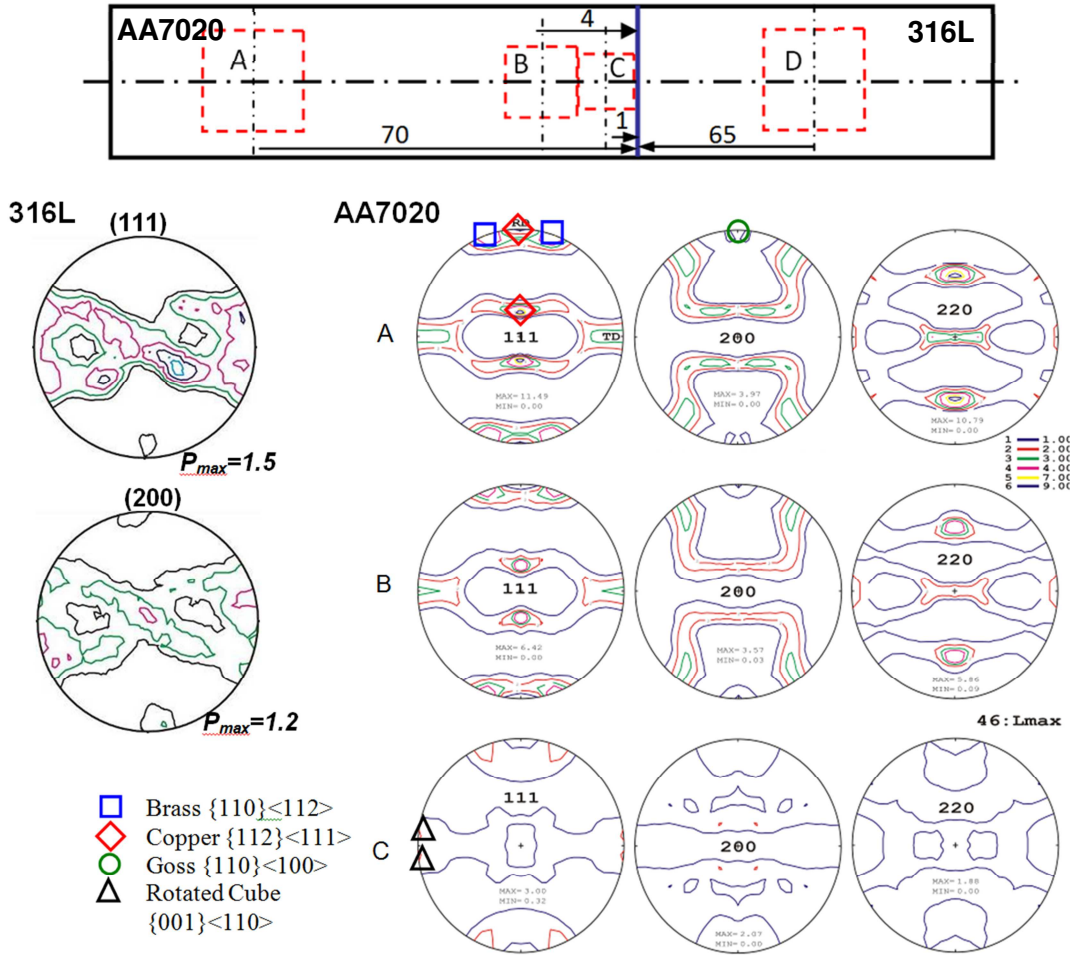

Fig. 2.1 Measured pole figures of 316L steel and AA7020, respectively.

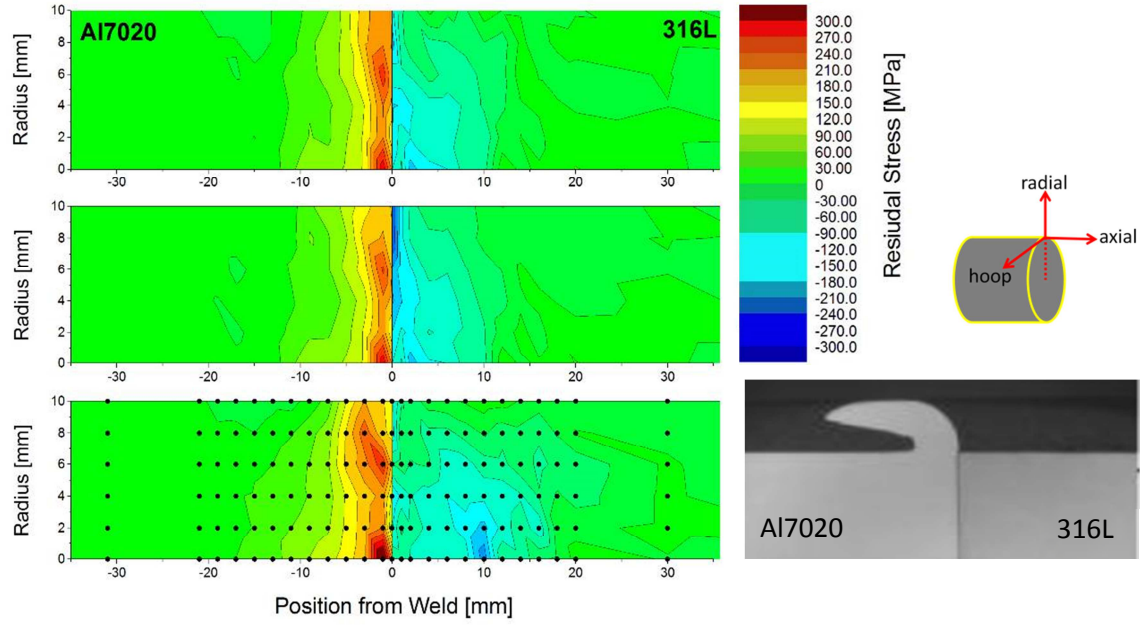

Fig. 2.2 Residual stress maps of the RFW weld of AA7020-T6 alloy (on the left) and 316L steel. From top to bottom are shown: radial, axial and hoop stresses.

2.4 Summary

(1) Local texture analysis indicated a weak shearing component near the weld line of AA7020-T6, in good agreement with the microscopic results.

(2) Residual stress mapping by neutron diffraction demonstrated a gradual increase of a tensile residual stress located at about 10 mm to the weld line on the AA7020-T6 side; and it indicated a non-uniform distribution through the diameter of the rod. A maximum compressive residual stress was produced at the rod centre near the weld line on the 316L steel side.

References:

[2.1] P. T. Houldcroft, Welding Process Technology, Cambridge University, Cambridge 1977.

[2.2] V. Ventzke, H.-G. Brokmeier, P. Merhof, M. Kocak. Solid State Phenon. 160 (2010) 319-326.

[2.3] W.M. Gan, M. Hofmann, V. Ventzke, C. Randau, Y.D. Huang, A. Kriele, H.-G. Brokmeier. Mater. Sci. Forum. 879 (2017) 572-577.

[2.4] L.A.I. Kestens, H. Pirgazi. Mater. Sci. & Tech. 32 (2016) 1303-1315.

3. Influence of texture on microstructure, tensile properties and residual stress state of laser welded Ti joints

3.1 Introduction

Titanium and its alloys are extensively used in the aerospace and automotive industries. Commercially available Ti semi-finished products are normally in sheet form, in which strong texture conventionally exists. This could lead to anisotropic mechanical and physical properties (e.g. thermal expansion varies along different crystallographic directions of a hexagonal crystal structure and conductivity). Laser beam welding (LBW) of engineering components used in these industrial fields is receiving increased attention [3.1]. Residual stresses play a significant role in the performance of welded joint, since unfavorable residual stresses cause, for instance, fatigue failures due to an accelerated fatigue crack growth [3.2].

Preferred grain orientations/ texture of base materials could influence the mechanical properties, the residual stresses and the microstructure of the welded joints. This should be considered for design purposes, in particular for materials having non-cubic crystal structures. Numerous experiments have been carried out in this field of study without considering the crystallographic texture based anisotropy of base materials. In the present study, commercially pure titanium (CP-Ti) rolled sheets were laser welded along various directions with respect to the sample orientations, namely rolling direction (RD), transverse direction (TD) and 45° to RD. Three-dimensional strain profiles and the local texture around the weld were measured by neutron diffraction at STRESS-SPEC. Various sets of sample orientations, namely S1 = sample 1 (Rolling Direction RD on side A ↔ RD on side B), S2 = sample 2 (RD on side A ↔ 90° to RD on side B) and S3 = sample 3 (RD on side A ↔ 45° to RD on Side B) as shown schematically in **Fig. 3.1**, were prepared. Side A is fixed with the RD perpendicular to the welding direction for all samples, whereas side B has three orientations, as detailed above.

3.2 Microstructure

A low-magnification microstructure of the transverse cross section of each welded joint obtained by PLM (polarized light microscopy) is shown in **Fig. 3.2**. Obviously, three zones of the laser welded joints, namely the base material (BM), the heat affected zone (HAZ) and the fusion zone (FZ) can be distinguished. Furthermore, these micrographs clearly show the full penetration of the welds as well as a variation of local grain shape and crystallographic orientation (texture) developed due to the welding process.

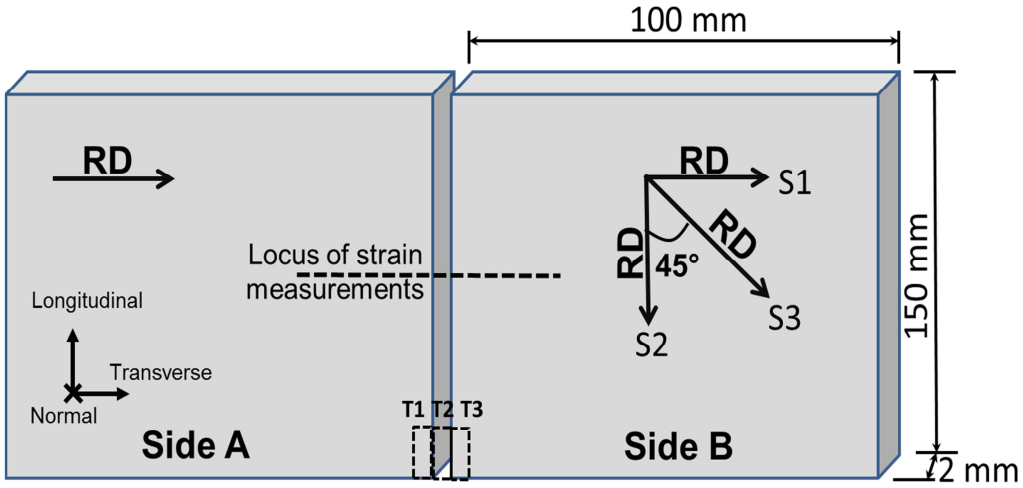

Fig. 3.1 Scheme showing the various sets of welded sheets. RD = rolling direction, S1 = sample 1 (RD-RD), S2 = sample 2 (RD-90° to RD), S3 = sample 3 (RD-45°to RD) and T = texture samples. The *longitudinal*, *transverse* and *normal* arrows/cross refer to the coordinates of stress components.

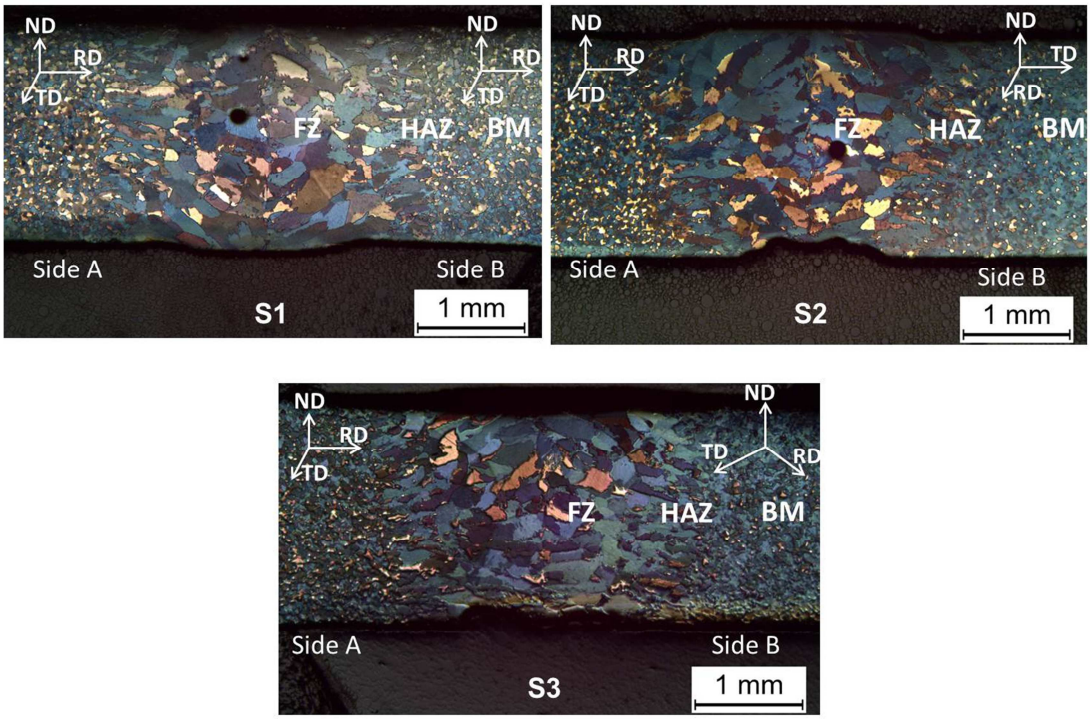

Fig. 3.2 Optical micrographs of laser welded CP-Ti. RD = rolling direction, TD = transverse direction, ND = normal direction, S1 = sample 1 (RD on side A- RD on side B), S2 = sample 2 (RD on side A - 90° to RD on side B), S3 = sample 3 (RD on side A - 45°to RD on side B), BM = base metal, HAZ = heat affected zone and FZ = fusion zone.

For quantitative grain orientation analysis, EBSD technique was used. The EBSD analysis revealed that the amount of Ti β-phase (cubic crystal structure (BCC) with space group Im-3m) in all the zones is small (volume fraction < 3%). Therefore, the current analyses focus only on the Ti α-phase (hexagonal crystal structure (HCP) with space group $P6_3/mmc$). The IPF micrographs of the grain maps of each zone of the joints are shown in **Fig. 3.3**. It should be pointed out that the EBSD examination was conducted on side B which has different sample orientations, since no significant change in the microstructure morphology of side A in S2 and S3 compared to that of side B of S1 is expected. The average grain size and misorientation angle of each zone are listed in **Table 3.1**. As seen, the FZ and HAZ have coarser and more elongated grains compared to the BM due to grain growth and the preferential direction of the heat flow.

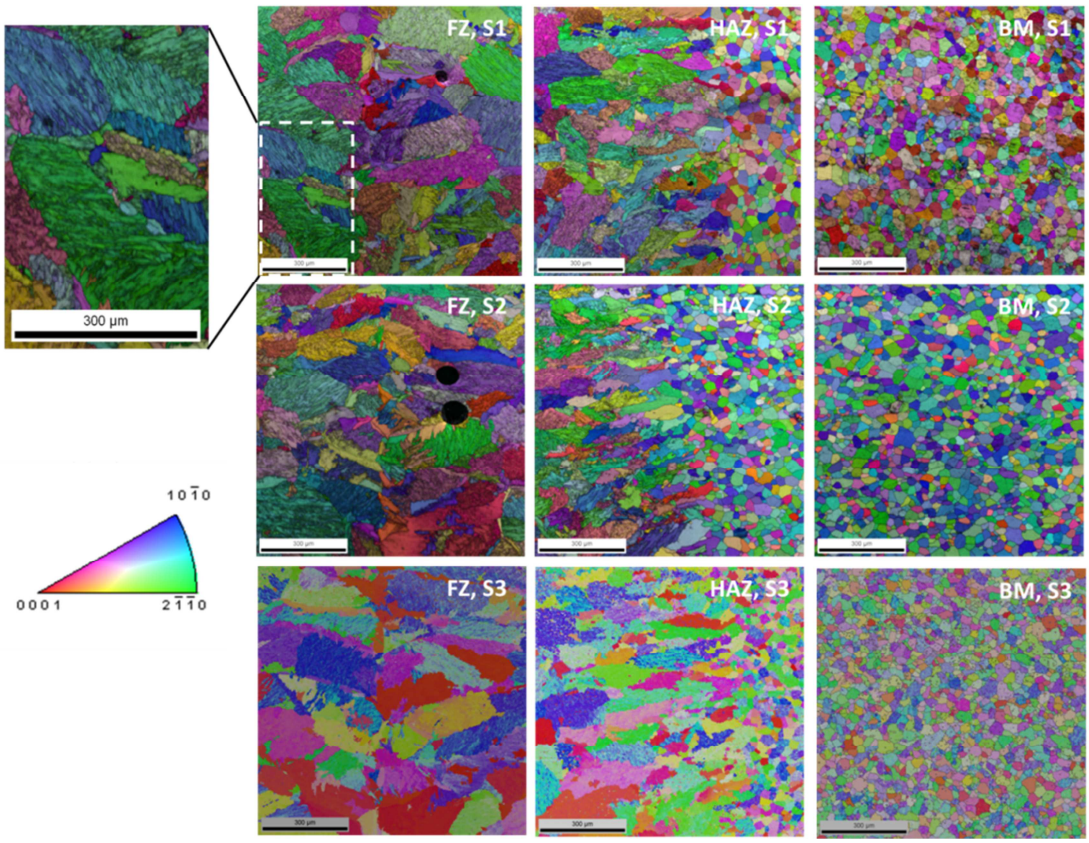

Fig. 3.3 EBSD IPF micrographs of the laser welded joints taken in the FZ, HAZ and BM zones of side B (color-code indicates orientations represented with the transverse direction inverse pole figure). S1 = sample 1 (RD on side A - RD on side B), S2 = sample 2 (RD on side A - 90° to RD on side B), S3 = sample 3 (RD on side A - 45°to RD on side B), BM = base metal, HAZ = heat affected zone and FZ = fusion zone.

Table 3.1 Average grain sizes and misorienation angles of BM, HAZ and FZ .

Zone		S1	S2 Side B	S3 Side B
BM	Average grain size (μm)	35	33	30
	Average misorienation angle (°)	54.5	53.6	54.8
HAZ	Average grain size (μm)	77	54	73
	Average misorienation angle (°)	56.0	57.3	57.4
FZ	Average grain size (μm)	144	122	128
	Average misorienation angle (°)	63.7	60.1	62.0

BM = base metal, HAZ = heat affected zone, FZ = fusion zone

In both the HAZ and the FZ, the microstructure consists of colonies of parallel α plates in delineated prior β grains due to transformation from β to α phase during cooling (see magnified image in **Fig. 3.3**). Moreover, finer grains are observed near the weld centerline. This grain morphology in the FZ depends on a complex relationship between the welding parameters and the temperature field. Interestingly, the HAZ of S2 has finer grains compared to S1 and S3. In order to understand this behavior of S2, the texture of S2 on both sides (side A and B) was measured at various positions (see **Fig. 3.4**a) using neutron diffraction which offers better grain statistics than EBSD. The results are compared with, for instance, the texture of S1 (Fig. **3.4**b). It should be noted that only one side of S1 (side A) was measured as the two sides are the same. It is clearly seen that the ideal texture component of the equiaxed α grains in the BM are {-12.5} <10.0> [3.3], where the {-12.5} planes lie on the rolling plane and the <10.0> directions are parallel to the rolling direction (RD), coming from the splitting of the basal plane from the normal direction (ND) with an angle of about ±33° toward the transverse direction (TD). The Euler angles (Bunge notation) of this component are $\varphi_1 = 0°$, $\phi \approx 33°$ and $\varphi_2 = 0°$ as shown in **Fig. 3.4**c of the orientation distribution function ODF of the BM. Besides, there is an overlap of fiber components which is typical for this rolled material, namely two basal fiber components tilted ±33° from the ND in the direction of TD as well as one <10.0> fiber which tends to align parallel to the RD along ϕ at $\varphi_1 = \varphi_2 = 0°$ (see the dashed lines in **Fig. 3.4**). Furthermore, there are a few grains in the BM with a basal pole oriented parallel to the TD which could be a result of the activation of a very weak {11.0} <00.1> or {10.0} <11.0> component as illustrated schematically in **Fig. 3.5**a and **Fig. 3.5**b, respectively. Due to the existence of this kind of weak texture component and the randomly oriented grains as a main part in the microstructure, some texture information cannot be seen in the pole figures. Also, {01.3} <2 -1.0> component was present in the sheet as seen in the ODF section with $\varphi_2 = 30°$ in **Fig. 3.4**c. This texture of rolled pure Ti sheets (c/a ratio smaller

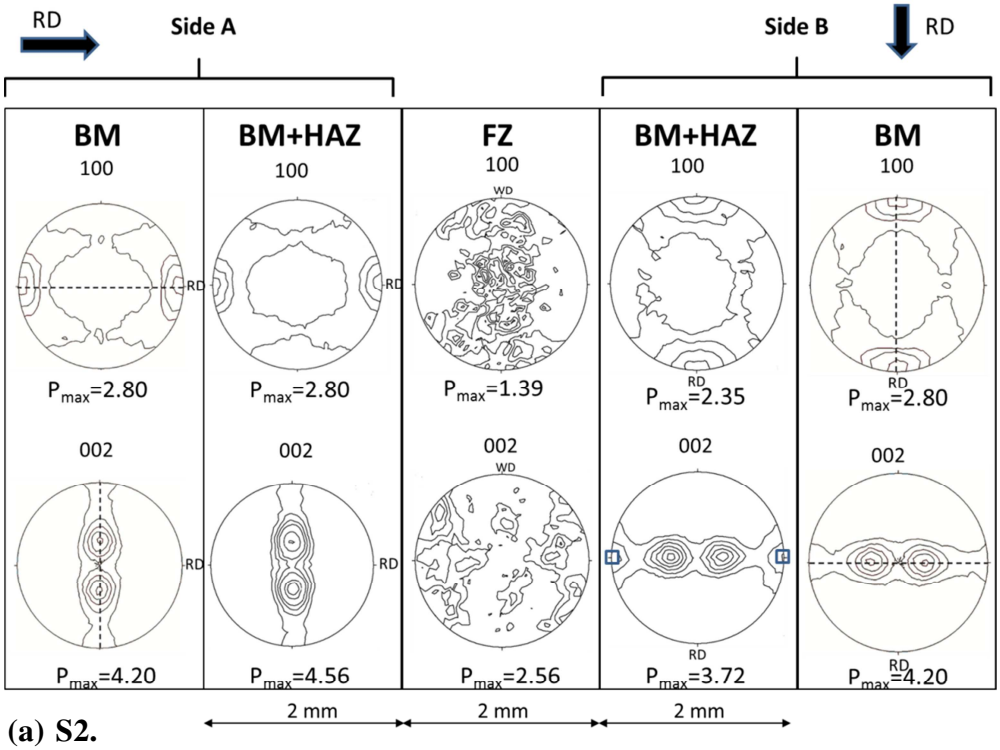

(a) S2.

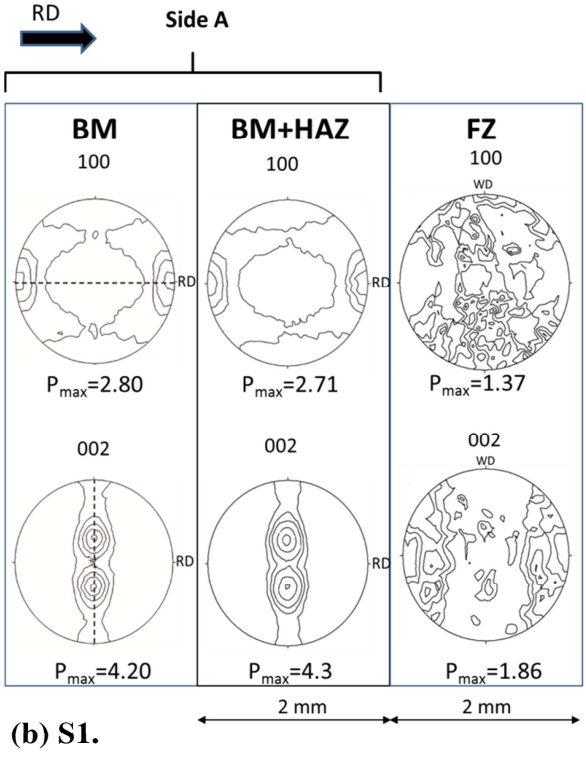

(b) S1.

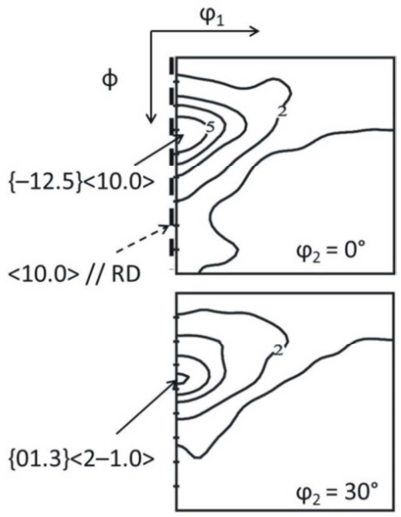

(c) Two ODF sections of the BM

Fig. 3.4 Texture development in the fusion zone (FZ) and base metal (BM) and heat affected zone (HAZ) of S2 (a) and S1 (b). P_{max} = maximum pole density, RD = rolling direction, WD = welding direction.

than the ideal ratio of 1.633) has arisen due to a combination of prismatic {10.0} <11.0> and basal {00.1} <11.0> slip during rolling process followed by annealing [3.4]. It should be noted that this kind of texture components can be changed depending on rolling and annealing parameters as well as alloying elements.

Obviously, more grains with a basal pole oriented parallel to the TD (blue square symbol in **Fig. 3.4** a) were developed in the BM+HAZ area of S2 on side B only where the RD is parallel to the WD. This is a result of activation of the recrystallization component {11.0} <10.0>, provided that there are grains of the BM with the basal plane oriented perpendicular to the WD as on side B of S2. This result indicates that the anisotropic physical properties of the BM due to texture could play a major role in recrystallization potential in welded joints. In addition, the texture in the FZ for both S1 and S2 is relatively weak and looks similar. The basal poles are oriented with a pronounced scattering toward the BM or perpendicular to the WD, since the easy grain growth direction for *hcp* metals occurs parallel to the basal plane in the <10.0> direction as reported by Lippold [3.6].

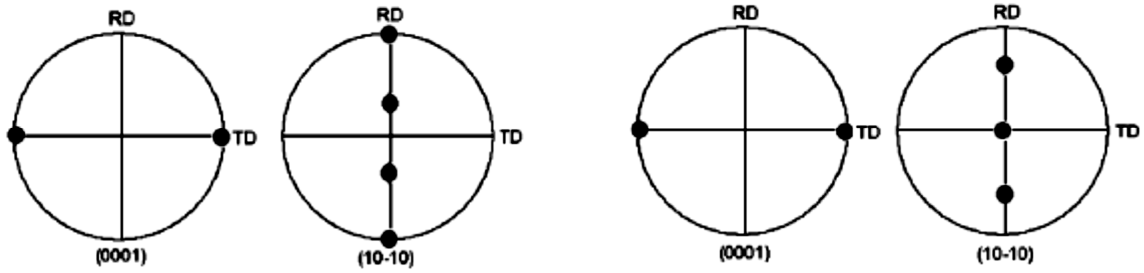

(a) {11.0} <00.1> (b) {10.0} <11.0>

Fig. 3.5 Scheme showing the texture components: {11.0} <00.1> (a) and {10.0} <11.0> (b) on both (00.2) and (10.0) pole figures [3.5]. RD = rolling direction, TD = transverse direction.

An example of the distribution of disorientation angle (DOA) of S1 which has similar trend to the other samples is shown in **Fig. 3.6** with different scales of *Number fraction*-axis for better illustration. Obviously, the peak frequency (number fraction) located at around 60°- 63° and 90° increased markedly in the HAZ compared to the BM and are more pronounced in the FZ than those in the HAZ and BM. This is dependent on the activation of certain crystallographic variants during the phase transformation from β to α and likely due to recrystallization. When pure Ti is cooled from above the β-transus, α phase grains are developed and oriented according to the Burgers relationship which generates 12 distinct

orientation variants of the α-phase with respect to a single β grain: $\{110\}_\beta$ // $(00.1)_\alpha$ and $<111>_\beta$ // $<11.0>_\alpha$.

The α/α orientations can be formed within a prior β grain by a combination of any two of the 12 orientation variants. The increase of the aforementioned DOA in the HAZ and FZ with a DOA around 10° is consistent with the following disorientation rotation axis/rotation angle pairs for α/α boundary as explained by Wang et al. [3.7]:

- [1 1. 0] / 60°,
- [-1.377 -1. 0.356] / 60.83°,
- [-10 5. -3] / 63.26°,
- [1 -2.38. 0] / 90°, and
- [0 0.1] / 10.53°

This result indicates that the number of α colonies inherited from the same parent β grain, with a tolerance of ±2.5°approximately, increases gradually from the HAZ to the FZ. Besides, the other disorientation angles cannot be related to a unique parent β grain through the Burgers orientation rotation [3.8].

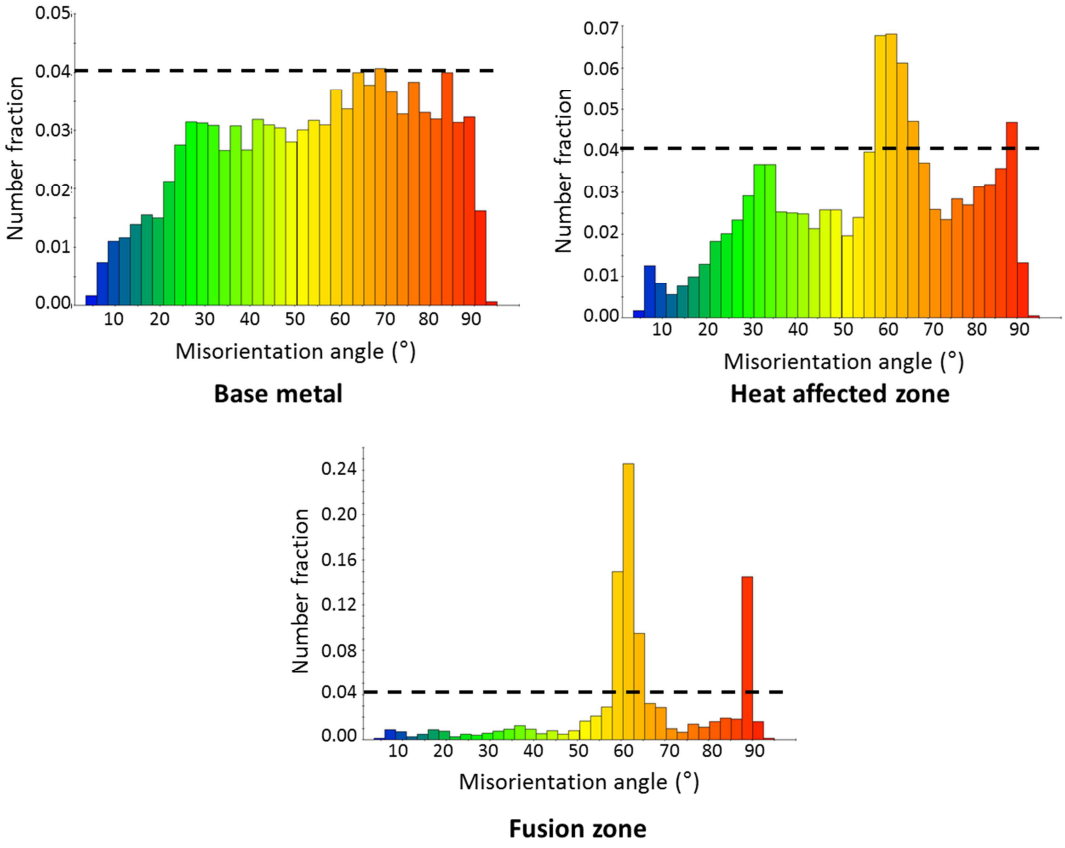

Fig. 3.6 Disorientation angle distributions of the BM, HAZ and FZ of sample 1 (S1). Dashed line represents the peak disorientation angle in the BM.

3.3 Mechanical properties

The micro-hardness profiles in the laser welded CP-Ti joints are displayed in **Fig. 3.7**. It is observed that the hardness increased gradually from the HAZ to the FZ compared with the BM with a peak percentage of 36% in S1, 14% in S2 and 23% in S3 on average. This is due to changes in microstructure, residual stress and texture. It is observed that the HAZ and the FZ of all the joints have coarse grains consisting of colonies of parallel plates of the α phase. This resulted in more strengthening in these zones compared with the BM. This agrees with the results published by Liu et al. [3.9]. A variation of the hardness profiles on both sides of the welded joints could be attributed to the influence of the developed texture. For instance, hardness values of S1 and S2 in the range between 1 and 2 mm from the weld centerline on side B are different. At this position, a new recrystallization texture component was developed in S2 on Side B with more basal planes oriented toward the TD as illustrated in **Fig. 3.4 a**. It is known that microhardness increases in an area where the basal planes are perpendicular to the indentation direction [3.10]. However, the microhardness of the HAZ is greater on side B of S2 compared to that on side A where stronger texture was developed. This increase in microhardness could be a result of higher density of grain boundaries (i.e. finer grains) in the HAZ on side B (see **Fig. 3.3** and **Table 3.1**).

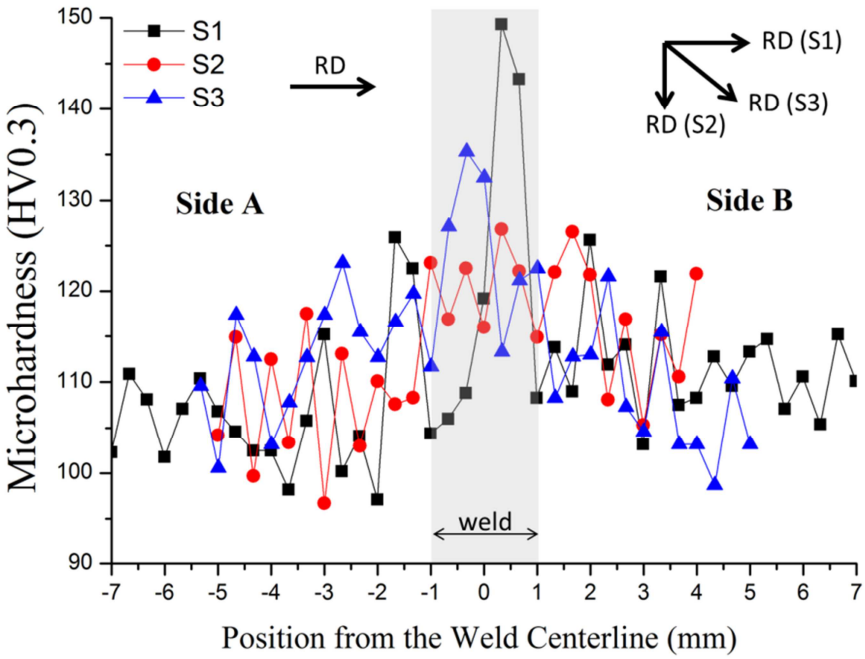

Fig. 3.7 Microhardness profiles in the laser welded CP-Ti samples. S1 = sample 1 (rolling direction RD on side A- RD on side B), S2 = sample 2 (RD on side A - 90° to RD on side B), S3 = sample 3 (RD on side A - 45°to RD on side B).

Tensile properties of the joints are obtained as average values of three tensile tests and are listed in **Table 3.2**. All tensile samples were broken at the BM due to its lower hardening than the FZ. Also, this indicates that the weld element is sound. Obviously, texture of the starting material plays a key role in the tensile properties of the welded joints. Tensile loading was applied on S1 in the direction parallel to the rolling direction (RD) of both sides, i.e. the loading direction is parallel to the prismatic pole or <10.0> and <2-1.0> (90° to the c-axis). This is the reason why S1 has the smallest Young's modulus (E), since it depends on the relation between the c-axis and the loading direction. For single Ti crystal, the c-axis has the greatest E, i.e. $E_{(00.2)}$, while $E_{(10.0)}$ is the smallest. The anisotropy factor ($E_{(00.2)}$ / $E_{(10.0)}$) in terms of Young's moduli is 1.40 [3.11]. This factor differs in polycrystalline materials depending on texture, alloying elements and likely microstructure. Furthermore, the anisotropic strength and ductility is attributed to the deformation system activated by tensile loading. When the tensile axis was parallel to the RD, the deformation was accommodated by the activation of the easier prismatic slip system (slip on the {10.0} planes in the <1-2.0> direction). This resulted in a lower yield strength and a higher ductility of S1. On the other hand, due to the orientation of the basal pole or c-axis between normal and transverse directions on side B of S2 as shown in **Fig. 3.4**, the more difficult deformation with basal (00.1) <12.0> or <a+c> pyramidal slip would occur. This relates to their greater critical resolved shear stress than that for the prismatic slip system as reported by Pawar [3.12]. This explains the lower ductility and higher yield strength of S2 in comparison with S1. The values of Young's modulus and yield strength of S3 (side B has a direction of 45° to the RD) lie between those for S1 and S2 due to a combination of aforementioned slip systems.

Table 3.2 Average results of tensile properties of laser welded joints of CP-Ti (Gr. 1).

Sample ID	E (GPa)	$\sigma_{0.2}$ (MPa)	UTS (MPa)	e_f(%)
S1	111	165	290	48
S2	139	176	286	36
S3	127	170	277	36

E = Young's modulus, $\sigma_{0.2}$ = 0.20% proof strength, UTS = tensile strength, e_f = engineering fracture strain.

In addition, it is observed that the tensile strength (UTS) of S1 is slightly higher than those of S2 and S3. It seems that the activation of deformation twining and corresponding grain orientations due to the plastic deformation during the tensile loading up to the necking strain

could be the reason for that change in the UTS. However, in situ texture inspection in CP-Ti samples cut from different directions should be conducted as well in order to understand that behavior.

3.4 Residual stress profiles

Longitudinal and transverse residual stress distributions in the welded joints are displayed in **Fig. 3.8**. It was found that the normal stresses are very close to zero in the welding zones, since stresses cannot be sustained in a thin sheet in the normal direction. Therefore, the normal stresses were not plotted in **Fig. 3.8** to make it clearer. Pronounced tensile residual stresses in the longitudinal direction were generated in the FZ and gradually decreased away from the weld. This stress is balanced by a compressive residual stress away from the weld centerline at a distance of approximately 6 mm. This is attributed to the shrinkage in the WD constrained by the BM during the cooling of the FZ and HAZ. On the other hand, the transverse stress component of the FZ which is perpendicular to the welding direction is small. It is well known that the laser welding generates low heat input to the BM which minimizes the shrinkage in the transverse direction. Furthermore, it is observed that the peak residual stresses in the FZ of all samples are similar and reach almost the yield stress of the BM.

In spite of the fact that the coefficient of thermal expansion (CTE) is anisotropic, i.e. $CTE_{(a\text{-}axis)} = 9.5 \times 10^{-6}\ C^{-1}$ and $CTE_{(c\text{-}axis)} = 5.6 \times 10^{-6}\ C^{-1}$ in single crystal Ti [3.13], and the variation in the microstructures in the distinct zones, the results show no significant statistical difference on the residual stresses related to the texture. This could be due to relatively weak texture (< 5 m.r.d) and relatively large gauge volume used for strain measurements which averaged possible strain gradients within that volume.

Nevertheless, further experiments are still needed on samples with sharper texture using a better spatial resolution. In addition, the uncertainty of the stress values due to a likely change in local diffraction elastic constants which are affected by a variation of local texture and microstructure developed in the welding zones must be considered as well. Moreover, CTE of the BM should be determined in three directions with respect to the rolling direction RD (0°, 45° and 90°) as well as in the normal direction and correlated with the texture. Modeling with finite element method is also required in order to understand the results and find out the predominant factors affecting this residual stress state.

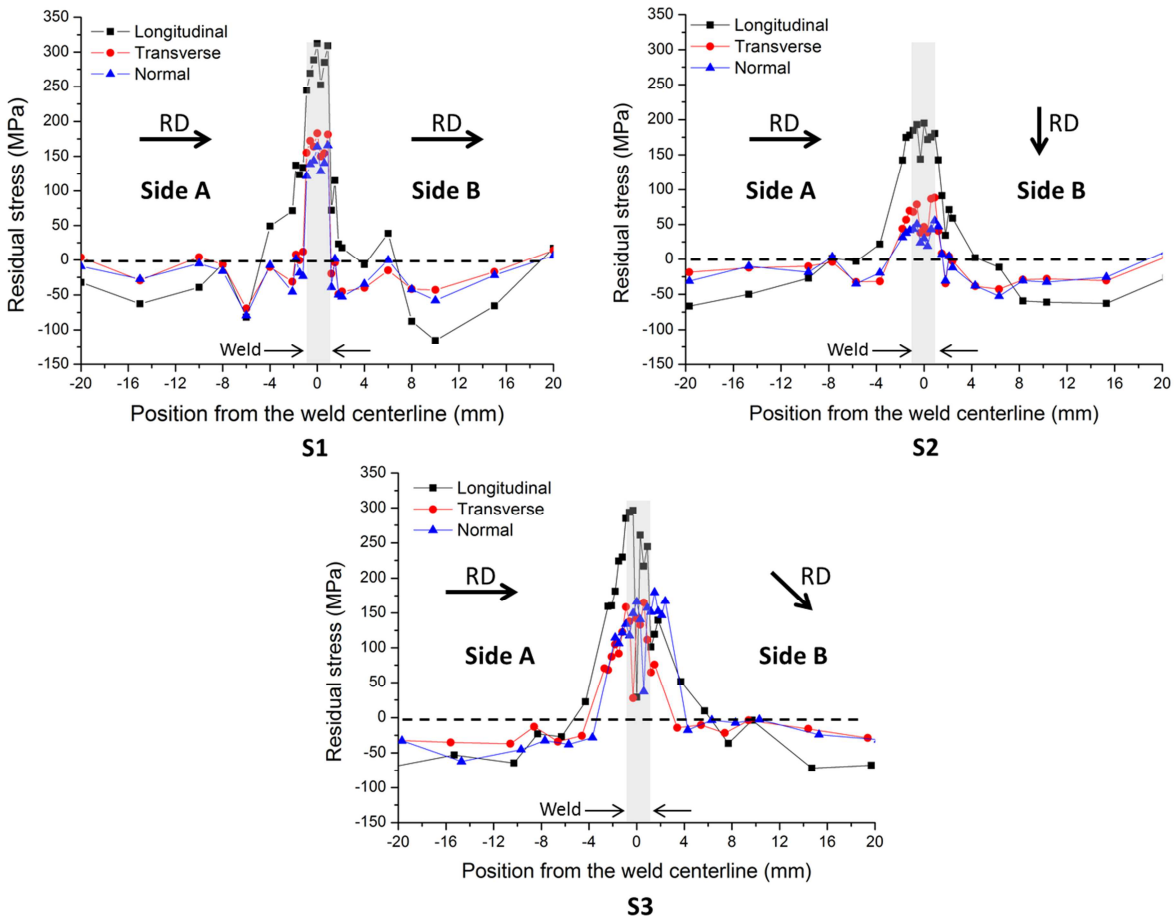

Fig. 3.8 Residual stress profiles in the laser welded CP-Ti samples. S1 = sample 1 (rolling direction RD on side A -RD on side B), S2 = sample 2 (RD on side A - 90° to RD on side B), S3 = sample 3 (RD on side A - 45°to RD on side B). Statistical errors are within ±25 MPa and ±50 MPa.

3.5 Summary

(1) The initial texture of the CP-Ti sheet to be laser welded plays a role in the mechanical properties and the microstructure of the welded joints. There is no significant statistical difference on the residual stresses related with the texture.

(2) This texture influence should be considered when welding engineering components in order to understand their behavior and to be able to compare the results.

References:

[3.1] W.M. Steen, J. Mazumder, Laser Material Processing, 4th Ed., Springer-Verlag, London, 2010. DOI: 10.1007/978-1-84996-062-5.

[3.2] E. Maawad, W.M. Gan, M. Hofmann, V. Ventzke, S. Riekehr, H.-G. Brokmeier, N. Kashaev, M. Müller. Materials & Design. 101 (2016)137-145.

[3.3] Y.N. Wang, J.C. Huang. Mater. Chem. & Phy. 81(2003) 11-26.

[3.4] M.J. Philippe. Materi. Sci. Forum. 157-162 (1994) 1337-1350.

[3.5] R.K. Leary, E. Merson, K. Birmingham, D. Harvey, R. Brydson. Mater. Sci. Eng. A 527 (2010) 7694-7705.

[3.6] J.C. Lippold, Welding Metallurgy and Weldability, John Wiley & Sons; Auflage: 1. Auflage (20. Januar 2015). P. 19. ISBN: 978-1-118-23070-1.

[3.7] S.C. Wang, M. Aindow, M.J. Starink, Acta Mater. 51 (2003) 2485–2503.

[3.8] H. Liu, K. Nakata, J.X. Zhang, N. Yamamoto, J. Liao. Mater. Charcht. 65 (2012) 1-7.

[3.9] H. Liu, K. Nakata, N. Yamamoto, J. Liao. Sci. Technol. Weld Join. 16 (2011) 224-233.

[3.10] R.K. Leary, E. Merson, K. Birmingham, D. Harvey, R. Brydson. Mater. Sci. Eng. A 527 (2010) 7694-7705.

[3.11] D. Tromans, Elastic anisotropy of hcp metal crystals and polycrystals, IJRRAS, 6-4 (2011) 462-483.

[3.12] R.R. Pawar, V.T. Deshpande. Acta Cryst. A 24 (1968), 316-317.

[3.13] H. Nasiri-Abarbekoh, A. Ekrami, A.A. Ziaei-Moayyed, M. Shohani. Mater. Des. 34 (2012) 268-274.

4. *In-situ* tensile texture analysis of a high ductility Mg-RE alloy

4.1 Introduction

A new Mg-RE (Mg- 0.38 wt.% Gd- 0.20 wt.% Zr) alloy was previously developed by micro-alloying method (when RE< 0.4 wt.%, named micro-alloying), and a high ductility and good corrosion resistance were achieved [4.1]. *In-situ* tensile tests under neutron diffraction were performed to investigate firstly the deformation behavior; and secondly the texture evolution which can be related to the deformation mechanism, and finally to understand why the as-cast Mg-RE alloys show such a high tensile ductility [4.2].

Less activation of dislocation system in Mg easily leads to strong anisotropy, i.e. the formation of preferred orientation/ texture [4.3]. Typical texture developed under thermo-mechanical deformation or annealing of Mg and its alloys has been well reported and documented [4.4, 4.5]. Study on the texture evolution can help to understand the activation of slip systems. Diffraction measurements for *in-situ* microstructural analysis, such as lattice strain and texture, using advanced neutron facilities demonstrate advantages because they offer a high penetration depth and a relatively fast data collection with area detector. Such kind of diffractometer equipped with load frames or furnaces is well developed in current days and are still in proving. Since crystallographic texture measurement is time consuming, high flux neutron measurements at successive points of the strain-stress curve under tensile or compression allow revealing texture evolution. Fundamentals of pole figure measurement using neutron diffraction has well been established. *In-situ* texture analysis in relation to the stress-strain behavior can provide experimental data to confirm the validity of texture simulation of and to understand the mechanical property evolution during tensile or compression experiments.

The texture measurement points were selected to some specific loads, i.e. under yield strength, strain hardening, hardening to platform transition, UTS and cracking, as marked by the 5 points in **Fig. 4.1**. At each point the specimen was first pulled to certain value of the load at a speed of 3.5 N/s; and then simultaneously to a fixed strain when the load is reached. Pole figure measurement was done using non-continuous phi rotation at 40 s per 5°.

4.2 Texture evolution

Fig. 4.2 shows the (10.0) and (00.2) measured complete pole figures from P1 to P5, respectively. At P1 a random orientation distribution is observed. At P2 where the sample was pulled to a strain of 7.3%, the basal plane of most grains are re-oriented to be parallel to the tensile direction (in the pole figure centre), i.e. the formation of a (10.0) fibre. Further

increase of tensile strain to P3 and P4, the pole figures show no obvious change but a slight increase of the maximum pole intensity. After being fractured at P5, a component similar to a shear component appeared. This should be due to an instantaneous torsion effect.

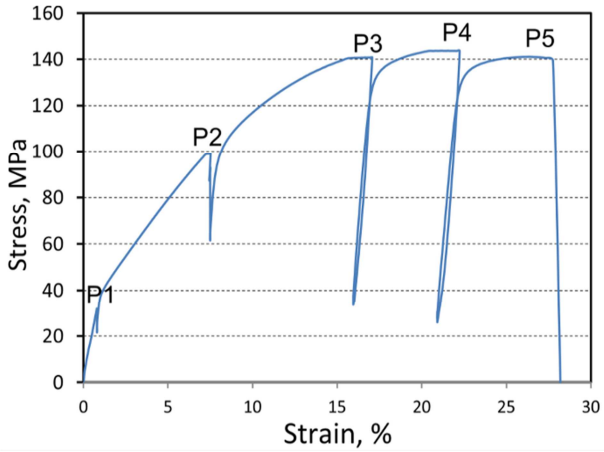

Fig. 4.1 *In-situ* pole figure measurement points from P1 to P5 in the tensile stress-strain curve.

To obtain more details the calculated inverse pole figures of the tensile direction at the five points are shown in **Fig. 4.3**. A standard inverse pole figure in which ideal texture components are marked [4.6] is also displayed as a reference. First, the strengthening of the (10.0) fibre from P2 to P5 is obvious. Second, non-basal components like (11.2) and (21.3) are obtained from P2 to P5. This indicates the activation of non-basal slip during tensile deformation. It is noted that there exit many twins in all the cases, which indicates that the twinning deformation is very active during the whole tensile deformation. Moreover, optical microstructures corresponding to the pole figure measurement points are also shown in **Fig. 4.4**. It is seen that there exits many twins in all the cases, which further confirms that the twinning deformation is very active during the whole tensile deformation.

Combining the texture and microstructure evolutions which are presented above, the tensile deformation behavior of the Mg-Gd-Zr alloy can be described as follows. The strong hardening from P1 to P2 shown in the tensile curve could be mainly due to the basal gliding and twinning deformation. However at P3 and P4 where a plateau occurs in the curve, the activation of non-basal slip is expected which contributes a lot to the increase of the ductility of this new Mg-Gd-Zr alloy. It should be also pointed out that the quantitative texture simulation can offer more details since similar studies have been done in conventional Mg alloys using the VPSC model [4.7].

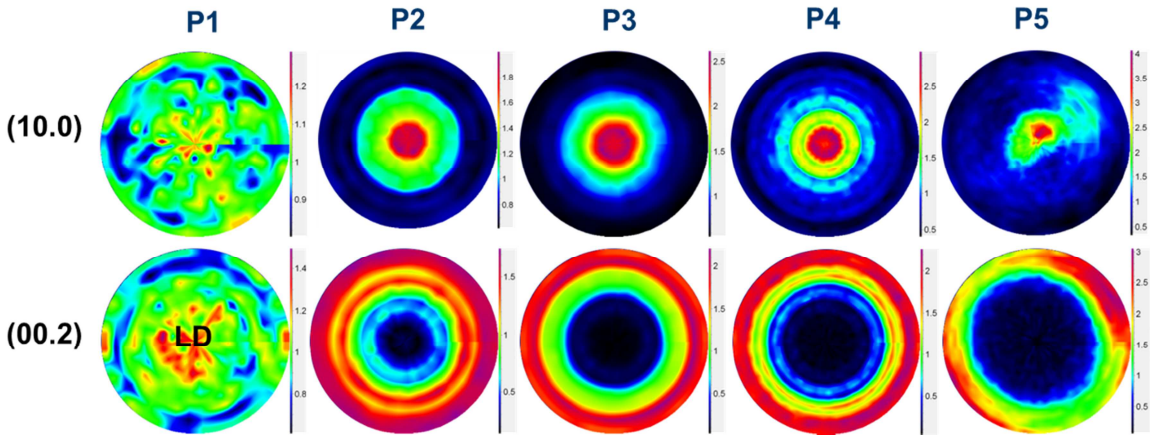

Fig. 4.2 (10.0) and (00.2) pole figure showing the texture evolution from P1 to P5 (tensile direction is in the pole figure centre).

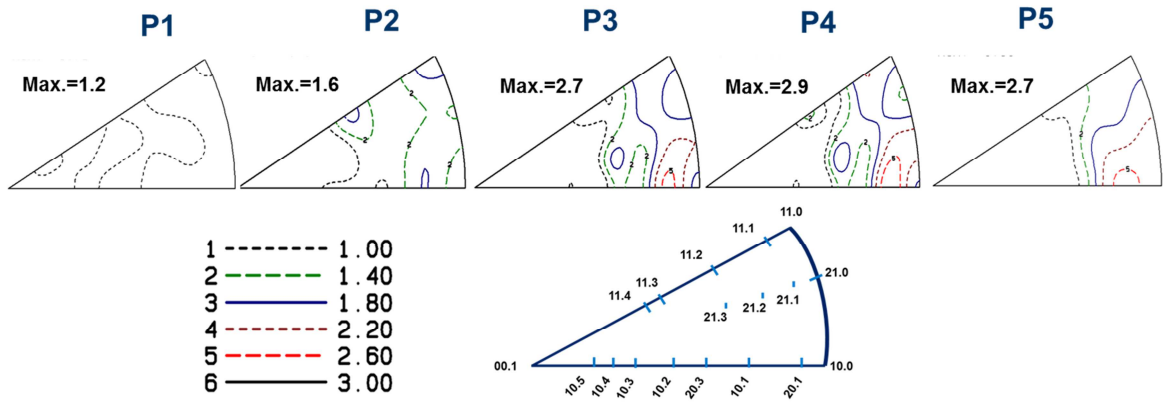

Fig. 4.3 Texture evolution presented with the tensile direction inverse pole figures from P1 to P5.

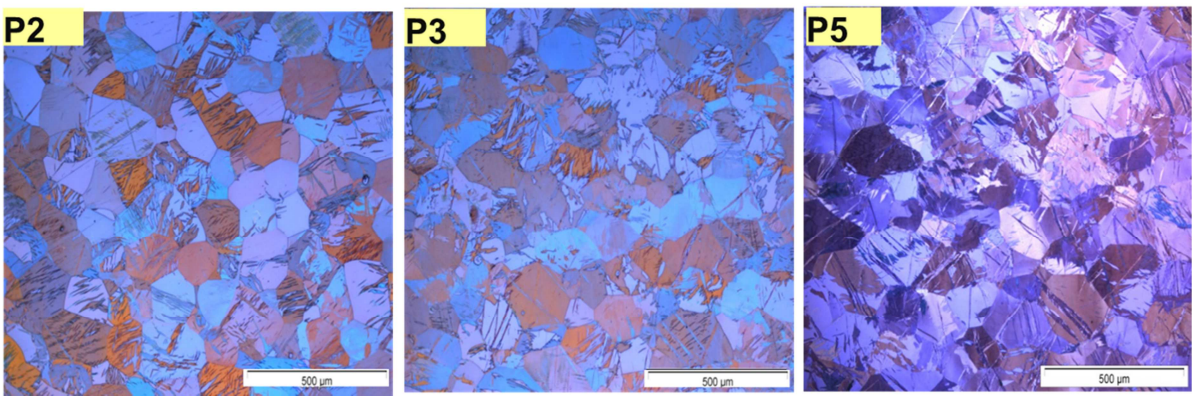

Fig. 4.4 Optical microstructures corresponding to the pole figure measurement points P2, P3 and P5, respectively.

4.3 Summary

The pole figures of the bulk samples at five strain points of a new Mg-Gd-Zr alloy during tensile deformation were successfully measured *in-situ* via neutron diffraction. The produced texture during tensile test has been well correlated to the strain hardening behavior and to the microstructure evolution. Results indicated that in addition to the basal glide and the twinning contribution, the activation of non-basal slip plays also an important role, especially at the stage when the strains reach the plateau part. This greatly contributes to the enhancement of the ductility of the new Mg-Gd-Zr alloy in this study.

References:

[4.1] Y.D. Huang, W.M. Gan, K.U. Kainer, N. Hort. J. of Mag. & Alloys. 2 (2014) 1-7.

[4.2] W.M. Gan, Y.D. Huang, Z. Wang, N. Hort. Mater. Sci. & Forum. 768-769 (2014) 428-432.

[4.3] P.G. Partridge. Metall. Rev. 12 (1967) 169-194.

[4.4] Y.N. Wang, J.C. Huang. Mater. Chem. & Phy. 81 (2013) 11-26.

[4.5] H.R. Wenk, P. Von Houtte. Rep. Prog. Phys. 67 (2004) 1367- 1428.

[4.6] I. Saxl, I. Haslingerova, J. Czechoslov. J. Phys. B 24 (1974) 1351.

[4.7] R.A. Lebensohn, C.N. Tome, Acta Metall. Mater. 41 (1993) 2611- 2624.

5. *In-situ* neutron diffraction study of Ni-Mn-Ga alloy

Ni-Mn-Ga alloys, which combine the properties of ferromagnetism with those of a reversible martensitic transformation, are conceived as a novel class of multifunctional magnetic materials [5.1- 5.3]. Under a magnetic field, these alloys demonstrate not only giant magnetic shape memory effect but also significant magnetocaloric effect. For instance, large magnetic field-induced strains up to 12% can be achieved in single crystals [5.4], originating from the magnetically driven reorientation of martensitic variants with strong magnetocrystalline anisotropy [5.5]. With the advantage of large output and fast dynamic response under magnetic field, such alloys have potential for various applications in actuators, sensors, and magnetic refrigeration systems.

In this work, the first part will present the variant redistribution of seven-layered modulated (7M) martensite under cyclic **T**hermo-**M**echanical **T**reatment (**TMT**) under *in-situ* neutron compressive deformation [5.6- 5.8]. And the second part will focus on the deformation mechanisms of Ni-Mn-Ga 7M martensite during a unidirectional compression process with an aim to fully uncover the deformation mechanisms of the Ni-Mn-Ga 7M martensite and to correlate the microscopic shear processes with the macroscopic mechanical behavior of the material.

5.1 Martensitic variant redistribution in polycrystalline Ni-Mn-Ga alloy under TMT

5.1.1 Experimental procedure

A polycrystalline Ni-Mn-Ga alloy ingot with nominal composition of $Ni_{50}Mn_{30}Ga_{20}$ was prepared by directional solidification, followed by homogenization at 1173 K for 24 h. The actual composition of the ingot was verified to be $Ni_{50.1}Mn_{28.8}Ga_{21.1}$ by energy dispersive spectroscopy (EDS) attached to a scanning electron microscope (SEM). The room-temperature crystal structure was determined by powder X-ray diffraction (XRD) with Cu-K_α radiation. The martensitic transformation temperatures were measured by differential scanning calorimetry (DSC, TA Q100) in a temperature range from 183 K to 473 K, with a heating and cooling rate of 10 K/min, respectively. The magnetic properties were measured with a vibrating sample magnetometer (VSM, Lakeshore 7407). The cylindrical-shaped samples with dimensions of Ø5 mm × 10 mm were cut from the ingot for the subsequent cyclic TMT and neutron diffraction.

The *in-situ* TMT and neutron diffraction experiments were performed using the materials science neutron diffractometer STRESS-SPEC at MLZ, with a monochromatic wavelength of 2.1 Å. The uniaxial compressive load was applied by a rotatable multifunctional (tension/

compression/ torsion) load frame installed at STRESS-SPEC, with the "constant load" mode to ensure a fixed load. For the *in-situ* measurements on the cyclic TMT, one cylindrical-shaped sample with dimensions of Ø5 mm × 10 mm was first heated from room temperature to 393 K to reach the fully austenitic state, where a uniaxial compression load of -10 MPa was applied on cooling along the solidification direction (SD). Then, the sample was cooled to room temperature at a cooling rate of 2 K/min under the constant load, during which the neutron diffraction images were continuously recorded at an interval of 60 s by a two-dimensional (2D) detector at $2\theta = 43.5°$. These two steps were taken as to constitute Cycle 1 of the TMT. For Cycle 2 and Cycle 3, the experimental conditions were the same as those of Cycle 1, except that the constant compression load was set to be -25 MPa and -50 MPa, respectively. The macroscopic strain changes of the tested sample in each cycle were measured by a clip-on extensometer in the load frame. Besides, the bulk crystallographic textures of the initial sample (without TMT) and the treated sample (with three TMT cycles) were measured *ex-situ*. The gauge volume for *in-situ* measurement was 5mm ×5mm ×5mm and Ø15 mm × open for *ex-situ* pole figure measurement, respectively.

For the present directionally solidified alloy, the start and finish temperatures of the forward and backward martensitic transformations - determined from the measured DSC curves - are respectively 347.8 K (M_s), 331.3 K (M_f), 336.8 K (A_s) and 352.2 K (A_f). According to the powder XRD analyses, the studied alloy consists of seven-layered modulated (7M) martensite at room temperature, having a monoclinic incommensurate superstructure with lattice parameters $a_{7M} = 4.2651$ Å, $b_{7M} = 5.5114$ Å, $c_{7M} = 42.365$ Å, and $\beta = 93.27°$ [5.9]. Under this superstructure frame, the easy magnetization axis of the 7M martensite corresponds to the *b* axis of the superstructure, *i.e.* $[0\ 1\ 0]_{7M}$.

5.1.2 Results and discussion

Fig. 5.1 shows the room-temperature microstructure of the studied alloy at the initial state. It can be seen that the original austenite grains are columnar-shaped along the SD, with an average diameter of ~500 μm. For cubic structured metals, the $<0\ 0\ 1>_A$ crystallographic directions are the principal crystal growth directions during solidification [5.10]. Thus, for the present alloy, the columnar-shaped austenite grains should have a strong $<0\ 0\ 1>_A$ preferred orientation parallel to the SD.

Fig. 5.1 Microstructure of directionally solidified and homogenized alloy at room temperature, showing the columnar-shaped morphology of original austenite grains.

Fig. 5.2(a) shows the neutron diffraction patterns of the initial cylindrical-shaped sample. At room temperature (~ 303 K), four reflections of 7M martensite, i.e. $(-1\ 0\ 10)_{7M}$, $(1\ 0\ 10)_{7M}$, $(0\ 2\ 0)_{7M}$, and $(1\ 0\ 13)_{7M}$, were detected in the 2θ range of ~36°-52° (**Fig. 5.2(a)-** lower), where the $(1\ 0\ 10)_{7M}$ diffraction possesses the strongest intensity. Within the measured 2θ range, only the $(2\ 0\ 0)_A$ diffraction can be observed in the austenite temperature region (**Fig. 5.2(a)-** upper). **Figs. 5.2(b)-5.2(d)** display the serial patterns measured on cooling across the martensitic transformation under the compressive load of -10 MPa (Cycle 1), -25 MPa (Cycle 2), and -50 MPa (Cycle 3), respectively. It is seen from **Fig. 5.2(b)** that under ~10 MPa, the martensitic transformation started at around 348.7 K and finished at around 335.9 K. Compared with the initial sample, the compressive load of ~10 MPa has led to a certain increase in *Ms* (~0.9 K). Moreover, the strongest diffraction peak of 7M martensite was changed to the $(0\ 2\ 0)_{7M}$, suggesting a redistribution of martensitic variants induced by the applied load during the martensitic transformation. For Cycle 2 under -25 MPa (**Fig. 5.2(c)**), the martensitic transformation started at around 350.1 K and finished at around 339.4 K, being slightly higher than the corresponding temperatures of Cycle 1. Meanwhile, the $(0\ 2\ 0)_{7M}$ diffraction intensity of 7M martensite was increased with respect to Cycle 1. As for Cycle 3 under -50 MPa (**Fig. 5.2 (d)),** the martensitic transformation further shifted to a higher temperature region (M_s= 356.3K and M_f= 345.6 K). There remained at room temperature

almost only the $(0\ 2\ 0)_{7M}$ reflection in the measured 2θ range after the completion of the three TMT cycles, as shown in **Fig. 5.2(e).** Apparently, the uniaxial compression has exerted significant influence on variant distribution, creating a strong preferential orientation of the $(0\ 2\ 0)_{7M}$ plane.

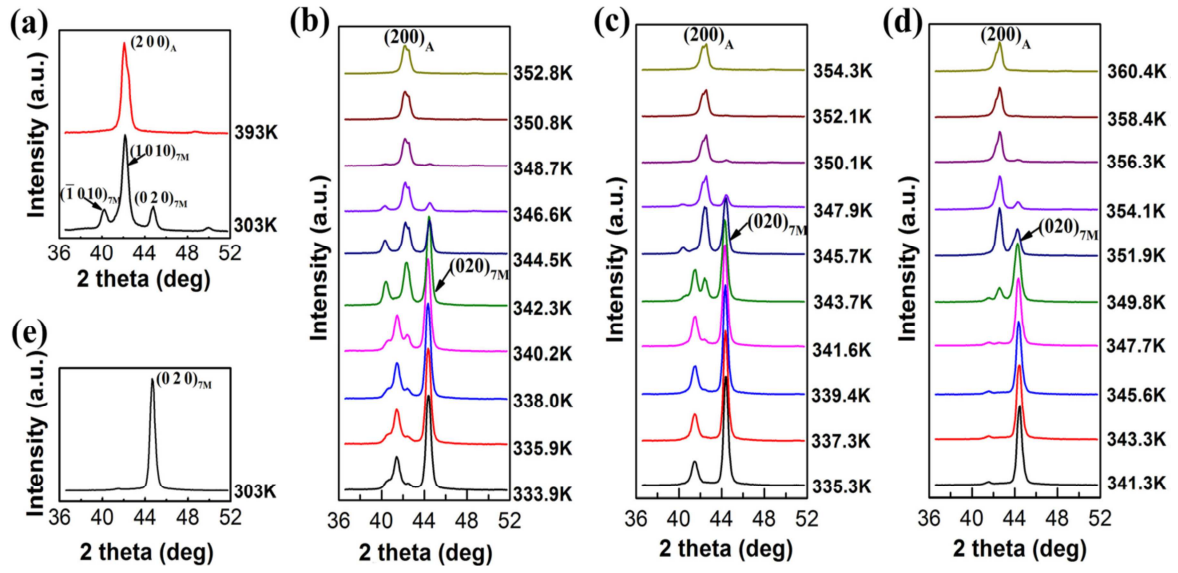

Fig. 5.2 (a) Neutron diffraction pattern measured on initial sample at ~393 K and ~303 K. (b)-(d) Neutron diffraction patterns measured on TMT sample during cooling under compressive load of ~10 MPa (Cycle 1), ~25 MPa (Cycle 2), and ~50 MPa (Cycle 3). (e) Neutron diffraction pattern measured on TMT sample at ~303 K without compressive load after three TMT cycles.

The macroscopic shape changes of the tested sample in each cycle, recorded with the integrated *in-situ* measurements, are presented in **Fig. 5.3**. It is seen that the uniaxial compressive load applied during martensitic transformation resulted in considerable macroscopic strain. With increasing the compression load, the deformation amount increased gradually, i.e. -2.1%, -2.8% and -3.3% for Cycle 1, Cycle 2 and Cycle 3, respectively. Such a trend may also indicate the increase in the degree of preferred variant orientation. Here, the gradual strain changes before and after the martensitic transformation could be due to the shrinkage on cooling, which were also observed by other authors [5.11, 5.12].

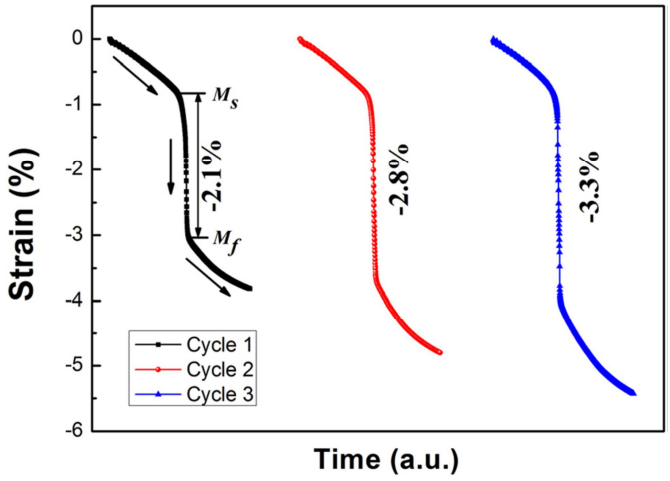

Fig. 5.3 Macroscopic strain curves of tested sample under three TMT cycles.

According to the *in-situ* neutron diffraction measurements, the applied uniaxial compression can significantly influence the martensitic transformation thermodynamics, resulting in increased transformation temperatures. With increasing compression load, the martensitic transformation temperature increases gradually. The increases of M_s under -10 MPa, -25 MPa and -50 MPa were ~0.9 K, ~2.3 K and ~ 8.5 K, respectively. The shifts of transformation temperature under uniaxial load σ - observed in the present work - can well be described by the Clausius-Clapeyron equation: $d\sigma/dT = -\Delta S \cdot \rho/\varepsilon$, where ΔS and ε stand respectively for the entropy change and transformation strain, and ρ is the mass density. Here, the entropy change ΔS was determined from the DSC measurements to be ~21.7 J $kg^{-1}K^{-1}$, and the mass density ρ was taken as ~7.964 g·cm^{-3} [5.13]. By inputting the corresponding values to the Clausius-Clapeyron equation, it derives that the uniaxial load of -10 MPa, -25 MPa and -50 MPa can result in the respective increase of 1.2 K, 4.1 K and 9.5 K in M_s, which are rather close to the observed transformation temperature shifts.

The backscattered electron (BSE) images of the initial sample and the TMT sample are shown in **Figs. 5.4a** and **4b**, respectively. It is seen from **Fig. 5.4a** that in the initial state, the 7M martensite plates exhibit typical self-accommodated microstructure. There appear a certain bending in some individual plates and most of them tend to be parallel to the SD. Besides, the neighbouring plates are very close in plate thickness. After three cycles of treatment, the resultant microstructure is totally different from that of the initial state, as shown in **Fig. 5.4b**. The 7M martensite plates are straighter and tend to be oriented with an angle of ~45° to the loading direction (LD). It is noted that the thickness ratio of neighbouring

plates has changed greatly, i.e. one plate is much thicker than the other. Especially, the thinner plates almost disappeared in some local regions. This simpler variant configuration should be originated from the accommodation of the external compression by suppressing certain unfavourable variants. Moreover, such kind of variant arrangement should be also advantageous for the variant interface movement. As demonstrated by Straka *et al*. [5.14], a mixture of differently oriented variants exhibited a relatively large twinning stress, whereas the single-variant or two-variant microstructure could result in a reduced twinning stress, which is much easier for variant reorientation.

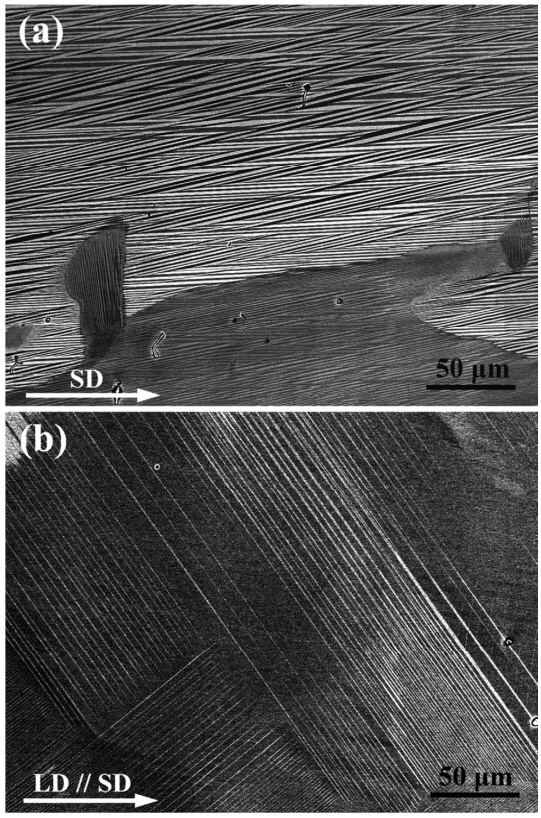

Fig. 5.4 (a) BSE image of 7M martensite without TMT. (b) BSE image of 7M martensite after three TMT cycles.

To have further insight into the variant redistribution induced by external compression during martensitic transformation, the complete pole figures were constructed using the neutron diffraction data. Here, the high penetration capability of neutrons, which exceeds that of X-rays by about four orders of magnitude, is considered to allow more reliable analysis on the global orientation distribution of the studied samples. Since the easy magnetization axis is an important parameter that accounts for the magnetocrystalline anisotropy in Ni-Mn-Ga

alloys, we shall focus on the orientation distribution of the easy magnetization axis of 7M martensite (i.e. $<0\ 1\ 0>_{7M}$). **Fig. 5.5** displays the $(0\ 2\ 0)_{7M}$ complete pole figures of the samples without and with the cyclic TMT. It can be seen that in the initial sate (**Fig. 5.5a**), the $<0\ 1\ 0>_{7M}$ directions of 7M martensite tend to be perpendicular or parallel to the SD. After the three cycles of treatment (**Fig. 5.5b**), the $<0\ 1\ 0>_{7M}$ directions become almost parallel to the LD (//SD). Notably, a strong $<0\ 1\ 0>_{7M}$ preferential orientation along the LD was induced by the external compression during the martensitic transformation.

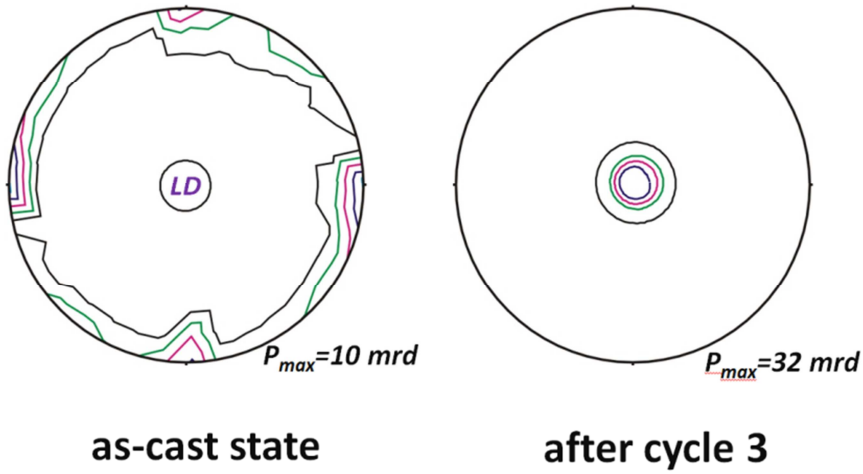

Fig. 5.5 $(0\ 2\ 0)_M$ pole figures of as-cast and of TMT 3 cycles. LD- loading direction // SD- solidification direction.

In order to analyze the influence of the cyclic TMT on the magnetic properties, the magnetization curves were measured on the initial sample (without TMT) and the TMTed sample (after three cycles of treatment) along the SD, as shown in **Fig. 5.6**. Evidently, the magnetization of the sample after the cyclic TMT is much easier to reach the saturation due to the presence of a strong $<0\ 1\ 0>_{7M}$ preferential orientation along the LD. The inset of **Fig. 5.6** displays the magnetization curves of the samples measured perpendicular to the SD (//LD). In this situation, the TMTed sample is more difficult to reach the saturation magnetization, as compared with the initial sample.

For directionally solidified Ni-Mn-Ga alloys, austenite grains form preferentially in columnar shape with their $<1\ 0\ 0>_A$ directions along the SD [5.10]. This particularity can be indirectly deduced from the $(0\ 2\ 0)_{7M}$ pole figure of the initial sample without TMT (**Fig. 5.5a**), where the $<0\ 1\ 0>_{7M}$ directions of 7M martensite tend to be perpendicular or parallel to the SD. With the specific orientation relationship for the austenite to 7M martensite

transformation [5.15], it can be predicted that parent austenite grains possess a strong <1 0 0>$_A$ preferential orientation parallel to the SD. Notably, in the present study, the uniaxial compressive loading was actually applied along the SD. As the <0 1 0>$_{7M}$ directions of the 7M martensite are inherited from the <1 0 0>$_A$ directions of the austenite with a reduction of the atomic spacing, the formation of the 7M martensite plates having the <0 1 0>$_{7M}$ // SD becomes more favourable under the uniaxial compression.

Further examinations on the neutron diffraction patterns demonstrate that the compressive loading has induced certain lattice strain in austenite. The lattice strain ε_{hkl} in the direction normal to a (h k l) lattice plane can be evaluated from the measured interplanar spacing (d_{hkl}) using the equation: $\varepsilon_{hkl} = (d_{hkl} - d_{0,hkl}) / d_{0,hkl}$, where $d_{0,hkl}$ is the stress-free reference interplanar spacing. Prior to the martensitic transformation, the lattice strains of the (2 0 0)$_A$ plane under three TMT cycles are determined to be -0.007 (-10 MPa), -0.0096 (-25 MPa) and -0.0105 (-50 MPa), respectively. These lattice strains would initiate the martensitic transformation. Meanwhile, the self-accommodation character of martensite variants is broken due to the lattice strains induced in certain directions in austenite. To accommodate these lattice strains of austenite, some variants with the <0 1 0>$_{7M}$ parallel to the LD form preferentially, leading to the macroscopic strain and the formation of a strong <0 1 0>$_{7M}$ preferred crystallographic orientation along the LD.

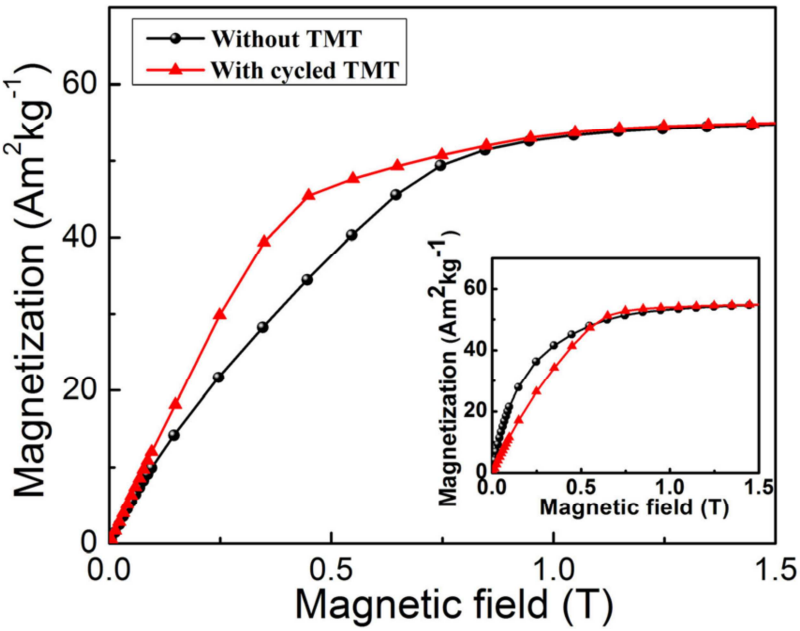

Fig. 5.6 Room-temperature magnetization curves measured on samples without and with TMT along SD (//LD). Inset: measured perpendicular to the SD (//LD).

5.1.3 Summary

The influences of uniaxial compression on martensitic transformation in a directionally solidified Ni-Mn-Ga polycrystalline alloy were studied by neutron diffraction. Direct experimental evidence was obtained on the redistribution of martensite variants, triggered by the uniaxial compression during martensitic transformation. The cyclic thermo-mechanical treatment resulted in large unidirectional lattice strains for the martensitic transformation and hence great change in the martensite microstructure. The 7M martensite plates formed with a strong $<0\ 1\ 0>_{7M}$ preferential crystallographic orientation along the loading axis, along which the saturation of magnetization was more easily reached. The present investigations provide fundamental information on variant selection subject to external stress field and the necessary guidelines for microstructure optimization of polycrystalline Ni-Mn-Ga alloys through external field training.

5.2 Deformation mechanisms Ni-Mn-Ga 7M modulated martensite studied by *in-situ* neutron diffraction and interrupted *in-situ* EBSD

5.2.1 Experimental procedure

For this work, a polycrystalline Ni-Mn-Ga alloy with nominal composition of $Ni_{50}Mn_{30}Ga_{20}$ was prepared by arc-melting using high purity raw materials in a shielding gas of argon. The ingots were re-melted for four times to achieve composition homogeneity. The alloy was further directionally cast by means of Bridgeman method at a withdrawal rate of 50 μm/s. The as-cast alloy was cut into rectangular parallelepiped samples with dimensions of 10 × 5 × 5 mm^3 with the longer edge parallel to the solidification direction (SD). The cut samples were further annealed under vacuum at 1173 K for 24 h and air-cooled to the room temperature to homogenize the composition.

Unidirectional compression under *in-situ* neutron diffraction measurement at room temperature was performed at neutron diffractometer STRESS-SPEC under constant loading rate (2 N/s). The neutron diffraction measurements with a monochromatic wavelength of 2.1 Å and a beam size of 5 × 5 mm^2 were performed under the experimental layout as illustrated in three-dimensions and a top view and a flat view in **Fig. 5.7**. The angle between the compressive load direction (LD) and the horizontal plane defined by the incident and the diffracted beams is χ, and the rotation angle around the LD is ω. These two angles define the orientation of the sample with respect to the incident beam and the detector. The LD tilts within a plane perpendicular to the diffraction plane and the horizontal plane. The neutron

diffraction images were continuously recorded each 60 s using a two-dimensional (2D) detector with an opening window of 14° (2θ).

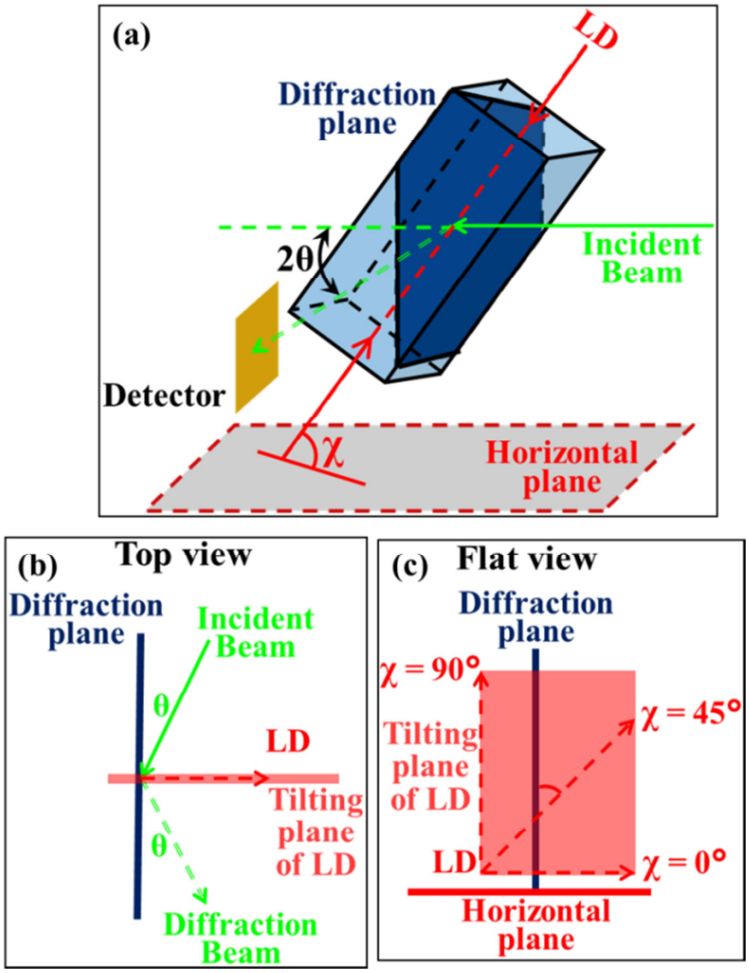

Fig. 5.7 Schematic representation of the sample position with respect to the compressive load direction (LD), the incident beam (BD) and the diffracted beam in (a) three-dimensional (3D) space, (b) the top view and (c) the flat view. The tilting plane of LD is perpendicular to the diffraction plane.

Pole figures of the initial sample and the deformed samples (with a reduction of 2%, 4% and 6%, respectively) were measured ex-situ by neutron diffraction to visualize the global texture evolution. The gauge volume of the samples for the pole figure measurements is 5 (parallel to SD) × 5 × 5 mm^3.

To follow the evolution of the microstructure and the crystallographic orientations of the sample during the unidirectional compression, an interrupted *in-situ* microstructural characterization was performed in a field-emission-gun scanning electron microscope (SEM,

Jeol JMF6500-F) with electron backscatter diffraction (EBSD) detecting system. Prior to the unidirectional compression, the samples were mechanically polished, and then electrolytically polished with a solution of 20% nitric acid in methanol at temperatures lower than 273 K and at a voltage of 18 V for 10 seconds. Unidirectional compression in 4 steps was performed manually using a home-made compression system. The accumulative reductions were 2%, 3%, 4.5% and 5.5%, respectively. Between steps, microstructural and crystallographic measurements were conducted in the same sample areas. To obtain statistical information, five EBSD maps with sizes of $80 \times 56\ \mu m^2$ were acquired.

To determine the *in-situ* neutron diffraction measurement setup, the initial texture of the as-annealed sample was studied. The present alloy is composed of single 7M modulated martensite at room temperature. The as-annealed texture is shown by the pole figures of $\{-1\ 2\ 10\}_{7M}$, $\{1\ 0\ \ 10\}_{7M}$ and $\{1\ 2\ 10\}_{7M}$ in **Fig. 5.8**. The three planes selected correspond to the respective twinning planes of the Type-I and the compound twins produced by the martensitic transformation (denoted TrF-twins) [5.16], and the Type-I deformation twins (DeF-twins) of the 7M martensite [5.16]. As it can be seen in the figures, the alloy possesses a partial fiber texture with the $\{-1\ 2\ \ 10\}_{7M}$ planes parallel to the solidification direction (SD) and the $\{1\ 0\ 10\}_{7M}$ planes perpendicular to the SD, and the $\{1\ 2\ 10\}_{7M}$ plane at about 46° to the SD.

From such a characteristic texture, the measurement setup of the *in-situ* neutron diffraction measurements during the unidirectional compression to monitor the three twinning systems can be conceived. The pole figures in **Fig. 5.8** indicate that the $\{-1\ 2\ 10\}_{7M}$, $\{1\ 0\ 10\}_{7M}$ and $\{1\ 2\ 10\}_{7M}$ planes are located at $\chi = 90°$ ($\{-1\ 2\ 10\}_{7M}$), 0° ($\{1\ 0\ 10)\}_{7M}$) and 44° ($\{1\ 2\ 10\}_{7M}$) respectively; thus three samples (denoted S1, S2 and S3) were used. The geometrical positions of the sample and the detector were chosen as given in **Table 5.1**. It is worth mentioning that due to the orientation spread of the planes, the sample position was adjusted with respect to the determined position to capture abundant diffraction signals.

Table 5.1 Sample orientation represented by χ, 2θ and ω in polar coordinate system.

Sample	χ (°)	2θ (°)	ω (°)
S1	90	62 (for $\{-1\ 2\ 10\}_{7M}$ reflection)	
S2	0	42 (for $\{1\ 0\ 10\}_{7M}$ reflection)	Adjustable
S3	44	62 (for $\{1\ 2\ 10\}_{7M}$ reflection)	

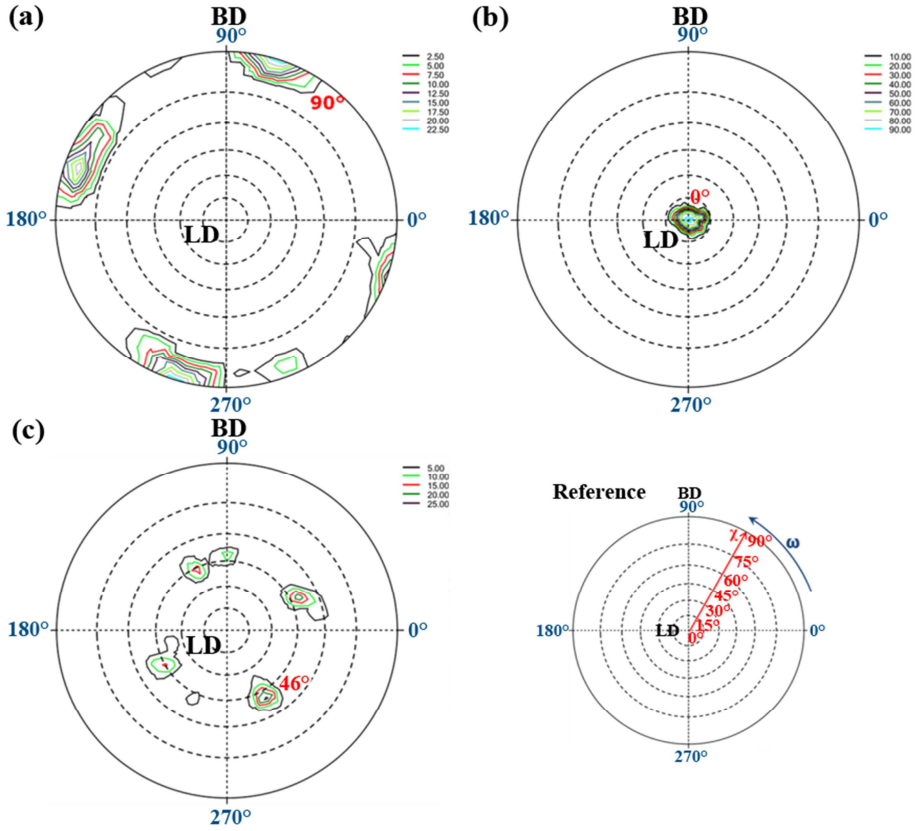

Fig. 5.8 $\{-1\ 2\ 10\}_{7M}$ (a), $\{1\ 0\ 10\}_{7M}$ (b) and $\{1\ 2\ 10\}_{7M}$ (c) pole figures of the as-annealed polycrystalline Ni-Mn-Ga. The reference coordinator system is displayed as (d).

5.2.1 Results and discussion

5.2.1.1 *In-situ* neutron diffraction patterns

Fig. 5.9 shows the stress-strain curve of the unidirectional compression and the corresponding *in-situ* neutron diffraction patterns of the three samples, acquired during the compression processes. The stress-strain curve in **Fig. 5.9(a)** well reveals the deformation characteristics of Ni-Mn-Ga 7M martensite [5.17]. From the starting point marked in black, the stress first increases almost linearly with the stain (the red line part), then stays more or less unchanged with the strain (the plateau part of the curve, *i.e.* the dark yellow and green line parts), demonstrating a steady stress state and again increases approximately linearly with the strain (the cyan line part). After the strain of the sample reaches the designed value as marked with the olive point, the unloading process begins (the blue line part) until completion.

The neutron diffraction patterns of S1 in **Fig. 5.9 (b_1)** well reveal the orientation change of the martensite during the deformation. It is seen that initially, only the $\{-1\ 2\ 10\}_{7M}$ diffraction

peak (2θ = ~62°) can be observed within the 2θ range of 55- 69°. This plane is the twinning plane of the Type-I TrF-twin that is produced by the martensitic transformation and is also the interface between the twin related variants (A/D or B/C) [5.18]. When the deformation reached the first part of the plateau (the dark yellow line part in **Fig. 5.9 (a)**), the $\{-1\ 2\ 10\}_{7M}$ peak weakens and a peak at 2θ = 60.4° starts to appear. This peak corresponded to the $\{1\ 1\ 2\}_{NM}$ (NM, non-modulated martensite) peak, indicating the occurrence of the 7M to NM intermartensitic transformation. Such a structural transformation was evidenced in the previous study [5.16]. When the deformation reaches the end of the plateau part (the green line part in **Fig. 5.9 (a)**), the $\{-1\ 2\ 10\}_{7M}$ peak largely weakens, but the $\{1\ 1\ 2\}_{NM}$ peak strengthens and a new peak appears at 2θ = 59.6°. This new peak corresponds to the $\{0\ 0\ 20\}_{7M}$ peak. This indicates the occurrence of variant reorientation of the 7M martensite through twinning. When the deformation continued to the second linear part (the cyan line part), the $\{-1\ 2\ 10\}_{7M}$ peak totally disappears. The intensities of the $\{1\ 1\ 2\}_{NM}$ peak and the$\{0\ 0\ 20\}_{7M}$ peak stay almost stable till unloading (the olive point in **Fig. 5.9 (a)**).

The similar situation appeared with the $\{1\ 0\ 10\}_{7M}$ peak that corresponds to the compound TrF-twinning plane. As shown in **Fig. 5.9 (b_2)**, the neutron diffraction patterns of S2, the $\{1\ 0\ 10\}_{7M}$ peak weakens in the first part of the plateau in the stress-strain curve and disappears in the second part (**Fig. 5.9 (b_2)**). Simultaneously, the $\{0\ 2\ 0\}_{7M}$ and the $\{1\ 1\ 0\}_{NM}$ peaks appear and strengthen, indicating the reorientation of the 7M variants through twinning/detwinning and the occurrence of the intermartensitic transformation during the deformation. In addition, the $\{1\ 0\ 10\}_{7M}$ peak in the first part of the plateau shifts slightly (~1°) toward the higher 2θ with respect to that in the first linear part of the stress-strain curve, indicating a decrease of the planar spacing of the $\{1\ 0\ 10\}_{7M}$ planes. As in the initial state, most of the 7M martensite was oriented with their $\{1\ 0\ 10\}_{7M}$ plane perpendicular to the compressive load (**Fig. 5.8 (b)**), the decrease of the planar spacing of these planes suggested an elastic response of the martensite to accommodate the imposed compression.

Fig. 5.9 (b_3) displays the diffraction patterns of S3 acquired during the deformation process. In addition to the intensity change of the existing 7M peaks and the disappearance/appearance of the 7M peaks that correspond to the reorientation of 7M martensite variants as evidenced in **Fig. 5.9 (b_1)** and **(b_2)**, the intermartensitic transformation is revealed, as highlighted with the rectangular frame in **Fig. 5.9 (b_3)** and further magnified in the insert in the figure. The $\{2\ 0\ 0\}_{NM}$ at 2θ = 65.6° firstly appeared in the first part of the plateau of the stress-strain curve (**Fig. 5.9 (a)**), indicating the deformation induced

intermartensitic transformation, but then greatly weakened in the second part and finally disappeared when the strain reaches the second linear deformation regime after the plateau. The disappearance of this peak could be a result of reorientation or a reverse intermartensitic transformation. This will be clarified with the interrupted *in-situ* SEM-EBSD investigation.

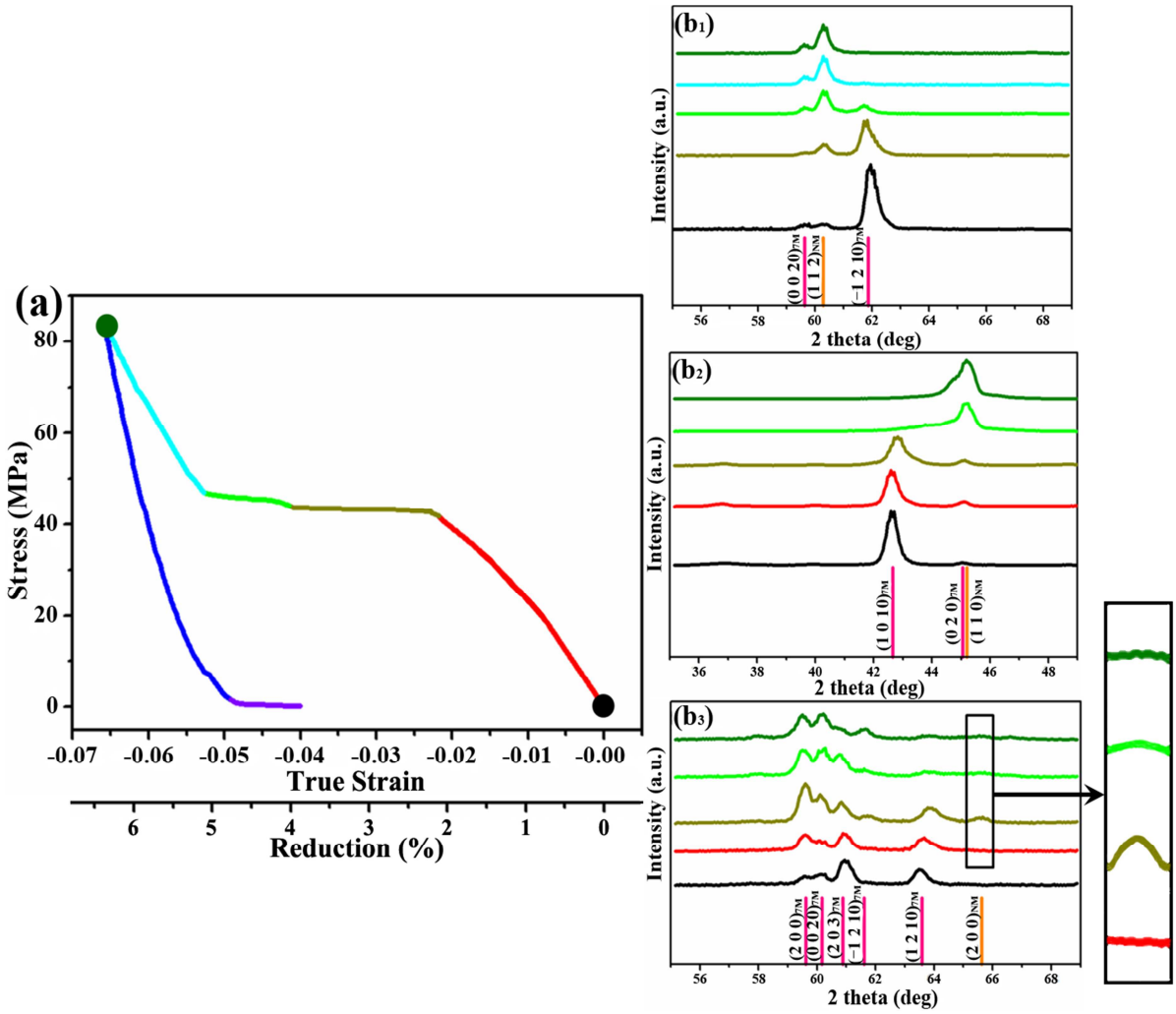

Fig. 5.9 Stress-strain curves during unidirectional compression at room temperature (a), and the corresponding neutron diffraction patterns ((b_1) for S1, (b_2) for S2 and (b_3) for S3) measured within 2θ of 35~49° or 55~69° at various deformation stages indicated with the consistent colors on the stress-strain curve. The evolution of $\{2\,0\,0\}_{NM}$ is highlighted with the rectangular frame in (b_3) and further magnified in the insert.

5.2.1.2 Interrupted *in-situ* EBSD examination

Fig. 5.10 displays a large scaled initial microstructure. The blue arrow shows the SD and the red lines highlight the initial austenite grains. It is seen that the material is composed of

plate shaped martensite located within the columnar original austenite grains. Most of the martensite plates align parallel to the SD.

Fig. 5.11 shows the EBSD micrographs acquired from one of the representative sample areas corresponding to the initial state (a_1), and the states after 2% (b_1), 3% (c_1), 4.5% (d_1) and 5.5% (e_1) reductions, as well as the corresponding area fractions of the martensite variants. The four reductions correspond to the first linear part (2%), the beginning part (3%) and the last part (4.5%) of the plateau, and the second linear part (5.5%) of the stress-strain curve in **Fig. 5.9(a)**. The measured area corresponds to one martensite colony. One can see that before the deformation there are four plate-shaped 7M martensite variants, referred to as variant A, B, C and D, (**Fig. 5.9(a_1)**). Crystallographic analysis demonstrates that the four variants are interrelated by three types of TrF-twin relations, *i.e.*, Type-I TrF-twin (A/C and B/D), Type-II TrF-twin (A/B and C/D) and compound TrF-twin relationships (A/D and B/C), as frequently reported in the literature for the 7M Ni-Mn-Ga alloys [5.19]. The corresponding twinning elements are listed in **Table 5.2**. The interfaces between the variants are their K_1 planes ($\{-1\ 2\ 10\}_{7M}$ for Type-I TrF-twins, $\{-1.0621\ 2\ 9.3785\}_{7M}$ for Type-II TrF-twins and $\{1\ 0\ 10\}_{7M}$ for compound TrF-twins), as marked in **Fig. 5.9(a_1)**. From **Table 5.2**, one can find that the Type-I and Type-II twins possess the same magnitude of twinning shear. The twinning shears of the compound TrF-twins are the same but with much smaller magnitude, one order smaller than those of the Type-I and Type-II TrF-twins. Thus the contribution of the compound TrF-twins is negligible. If we only consider the strain contribution of the variants through twinning or detwinning to the external deformation, the variants with compound TrF-twin relation can be treated as one variant. From **Fig. 5.11(a_2)** one can see that, the area fractions of variant A + D and variant B + C are similar, each pair being about 50%. To estimate the activation possibilities of the detwinning (of the TrF-twins) the existing variants, their Schmid Factors (SFs) were calculated with respect to the external compressive load, and are listed in **Table 5.3**. Although the activation of the individual shear systems is strongly related to their local stress state, we can assess that the applied external force imposes the major influence at the beginning of the deformation. The results show that the detwinning systems of all the three TrF-twin types have small SFs, but the detwinning of the compound TrF-twin has relatively higher SFs and should be easy to be activated.

Table 5.2 Twinning elements K_1, K_2, η_1, η_2, P and s of Type-I, Type-II and compound TrF-Twins.

Twinning element \ Variant pair	A-C or B-D (Type-I)	A-B or C-D (Type-II)	A-D or B-C (Compound)
K_1	$(1\ 2\ \bar{1}0)_{7M}$	$(1.0621\ 2\ \bar{9}.3785)_{7M}$	$(1\ 0\ 10)_{7M}$
K_2	$(\bar{1}.0621\ 2\ 9.3785)_{7M}$	$(\ \bar{1}\ 2\ 10)_{7M}$	$(\bar{1}\ 0\ 10)_{7M}$
η_1	$[\bar{1}0.5541\ 10\ 0.9446]_{7M}$	$[\bar{1}0\ 10\ 1]_{7M}$	$[\bar{1}0\ 0\ 1]_{7M}$
η_2	$[10\ 10\ \bar{1}]_{7M}$	$[10.5541\ 10\ \bar{0}.9446]_{7M}$	$[10\ 0\ 1]_{7M}$
P	$(\bar{1}\ \bar{0}.0570\ \bar{1}0.5699)_{7M}$	$(\bar{1}\ 0.0570\ \bar{1}0.5699)_{7M}$	$(0\ 1\ 0)_{7M}$
s	0.2299	0.2299	0.0135

Table 5.3 SFs of the detwinning systems of TrF-twin, twinning system of DeF-twin and the shuffling systems.

		SF
Detwinning of TrF-twin	Type-I	−0.0105~0.0094
	Type-II	−0.0045~0.0029
	compound	−0.1346~0.1192
Twinning of DeF-twin	Type-I	0.4657~0.4887
Shuffling		0.4708~0.4850

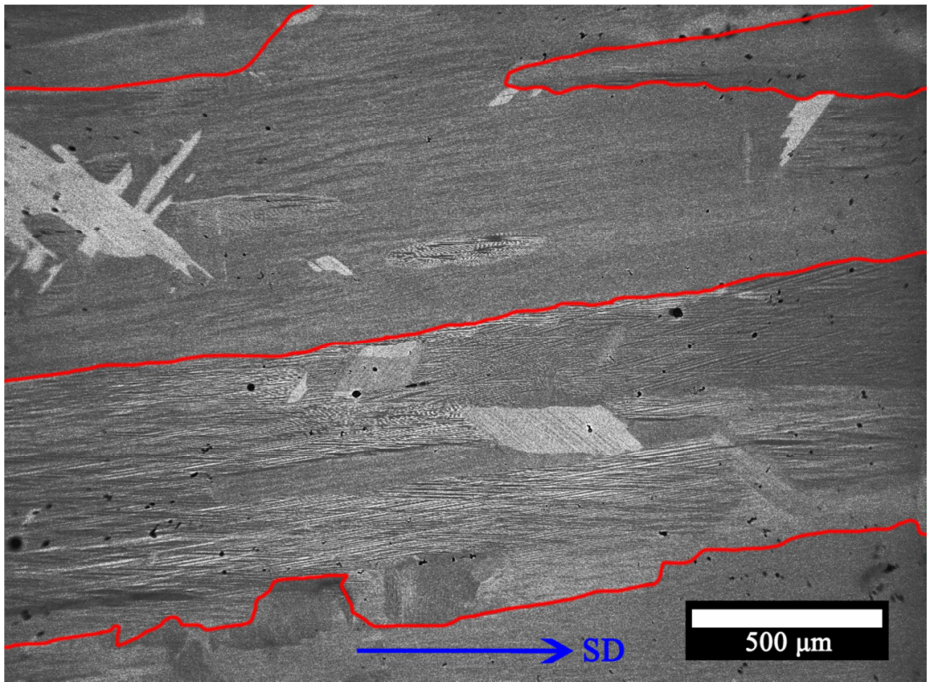

Fig. 5.10 SEM backscattered electron (BSE) micrograph of the as-annealed Ni50Mn30Ga20 alloy fabricated by directional solidification. The solidification direction (SD) is indicated with the blue arrow and the initial austenite grains are highlighted with the red lines.

Fig. 5.11(b_1) shows the microstructure in the same sample area after the 2% reduction, corresponding to the end of the first linear part of the stress-strain curve (**Fig. 5.9(a)**). Compared with that of the initial state, the area fraction of the variants changed with no new variant detected. The fraction of variant A increases at the expense of variant D (**Fig. 5.11(b_2)**). Although the fraction of variant B does not change much (**Fig. 5.11(b_2)**), from **Fig. 5.11(b_1)** one can nevertheless see that some of the variants slightly thicken. This thickening is still at the expense of variant D (variant B and D are Type-II TrF-twin related) to accommodate the macroscopic deformation despite of the low SF. These results reveal the occurrence of detwinning processes of the TrF-twins through twin boundary motion, evidencing the activation of the detwinning of TrF-twin systems, especially the detwinning of compound TrF-twin system. This is consistent with the SFs of the TrF-twins. Thus in the first linear part of the stress-strain curve, the alloy responses to the external loading by a mixed elastic-plastic deformation. The plastic deformation is mainly realized by the detwinning of the existing TrF-twins.

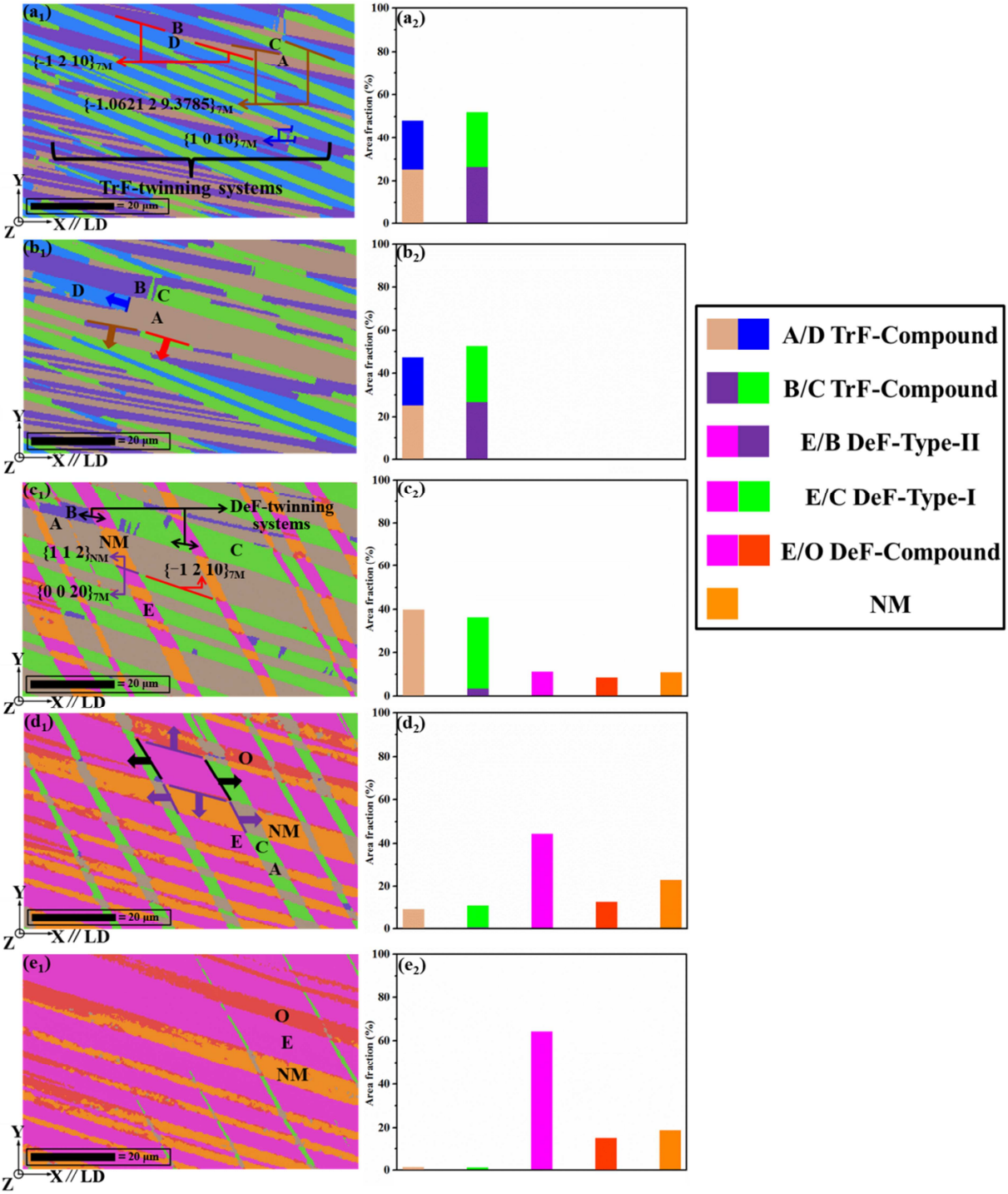

Fig. 5.11 SEM/EBSD orientation micrographs of the sample area acquired at reductions of 0% (a_1), 2% (b_1), 3% (c_1), 4.5% (d_1) and 5.5% (e_1). The corresponding area fractions of variants are displayed in (a_2)-(e_2). The compressive load is applied parallel to X axis that is also parallel to the solidification direction (SD).

When the sample is further deformed to the reduction of 3%, *i.e.,* the first half of the plateau part of the stress-strain curve (**Fig. 5.9(a)**), the microstructure changes drastically. Detwinning of the TrF-twins happens intensively. Variant D totally disappears and only limited area fraction of Variant B remains (**Fig. 5.11(c_1)** and **(c_2)**). However, the area fractions of variant A and C increase. Variants A and C are Type-I TrF-twin related. This confirms that the twinning resistance of the Type-I TrF-twins is much higher than those of the Type-II and the compound TrF-twins [5.20]. Accompanying the detwinning process between the existing variants with TrF-twin relations, the Type-I/II DeF-twinning systems [5.16] of the remaining variants and the shuffling system for intermartensitic transformation [5.16] of variant A are activated and new 7M variants (variant E in pink and variant O in jacinth in **Fig. 5.11(c_1)** and **(c_2)**) and NM martensite (in orange in **Fig. 5.11(c_1)** and **(c_2)**) are formed, indicating the reorientation of the 7M variants and the occurrence of the intermartensitic transformation. Variants E and C are in Type-I DeF-twin relation and variant O is twin related with variant A with an approximate DeF-twin relationship. The corresponding twinning elements were determined and are displayed in **Table 5.4**. Comparing the twinning elements of the DeF-twins with those of TrF-twins (**Table 5.4** with **Table 5.2**), one can find that the twinning shear of the DeF-twins is about one half of that of the TrF-twins, indicating that the deformation capacity of these twins are smaller than the TrF-twins. The SF of the twinning of DeF-twin systems and the intermartensitic transformation shuffling system under the compressive load were also calculated and are displayed in **Table 5.3**. It is seen that although these systems possess relatively larger SFs, none is activated when the detwinning of the TrF-twins (with lower SFs) happened intensively. This suggests that the twinning resistance or the Critical Resolved Shear Stress (CRSS) of these systems should be much higher. From the microstructures in **Fig. 5.11(c_1)** and **(c_2)**, we can see that the NM martensite and variant E are formed in continuity and repeatedly, changing the initial plate-like microstructure to a grid-like one. The orientation relationship (OR) between variant A and the NM is $\{0\ 0\ 10\}_{7M}$ // $\{1\ \bar{1}\ 2\}_{NM}$ and $<10\ 0\ 0>_{7M}$//$<1\ \bar{1}\ \bar{1}>_{NM}$ that is typical for the intermartensitic transformation of Ni-Mn-Ga alloys [5.16, 5.21]. The $\{0\ 0\ 1\}_{7M}$/$<1\ 0\ 0>_{7M}$ is also the shuffling system for the intermartensitic transformation [5.21]. These results reveal that the first part of the plastic deformation is realized by intensive detwinning of the existing TrF-twins (Type-I, Type-II and compound), the activation of the twinning of Type-I DeF-twin systems and the intermartensitic transformation.

Table 5.4 Twinning elements K_1, K_2, η_1, η_2, P and s of Type-I and Type-II DeF-twins.

Twinning element \ Variant pair	A_{C2}/E or D_{C2}/F (Type-I DeF-twin)	A_{C2}/F or D_{C2}/E (Type-II DeF-twin)
K_1	$(1\ 2\ 10)_{7M}$	$(1.1314\ 2\ 8.6864)_{7M}$
K_2	$(-1.1314\ 2\ -8.6864)_{7M}$	$(\ -1\ 2\ -10)_{7M}$
η_1	$[-11.045\ 10\ -0.8955]_{7M}$	$[-10\ 10\ -1]_{7M}$
η_2	$[10\ 10\ 1]_{7M}$	$[11.045\ 10\ 0.8955]_{7M}$
P	$(1\ 0.1103\ -11.1025)_{7M}$	$(1\ -0.1103\ -11.1025)_{7M}$
s	0.1154	0.1154

When the compression proceeds to 4.5%, *i.e.*, the second half of the plateau part of the stress-strain curve (**Fig. 5.9(a)**), drastic boundary motion happens (**Fig. 5.11(d_1)**) between variant C and E through twinning and between variant A and the NM martensite through intermartensitic transformation, resulting in the area fraction decrease of variants C and A and the area fraction increase of variant E and of the NM martensite, as displayed in **Fig. 5.11(d_2)**. Moreover, the boundary between variant C and E and that between variant A and the NM martensite moved coordinately, keeping the twin and the phase boundaries in continuity. This consistent movement is the consequence of the consistent shear deformation of the DeF-twin for variant C and the shuffling of variant A and the geometrical consistency of the two systems (the twinning system and the shuffling system), as detailed in Ref [5.16]. For an easy reference, the deformation gradient tensors representing the lattice deformation of the two shear systems, expressed in the macroscopic sample coordinate system (as used in **Fig. 5.11**, where the X axis is the compression axis), is given in **Table 5.5**. In the two tensors, the values of ε_{11} are smaller than 1, that of ε_{22} larger than 1 and that of ε_{33} close to 1. This indicates that the twinning of Type-I DeF-twin of variant C and the shuffling of variant A produce a contraction in the LD, and an elongation and a slight contraction in the other respective perpendicular directions. These characteristics reveal that the twinning of Type-I DeF-twin

and the shuffling well accommodate the macroscopic strain and also very compatible between them two. The similar shear elements ε_{ij} in the two tensors also demonstrate that the shear is consistent in forming the new 7M variants and in forming the NM martensite. Such geometrical consistency of the two systems (DeF-twinning and shuffling) allows the two deformation processes progress in continuity until the two old variants (C and A) are fully replaced. This accounts for the steady flow character of the deformation of the present material. Interestingly, such a deformation character is normally observed in the alloys with metallic bonds during their isothermal deformation process in which two processes, i.e., work hardening by dislocation multiplication and work softening by recovery and recrystallization, are in balance. However, for the present material the mechanism for the steady flow is very different. It is by a continuous process of highly coordinated twinning and intermartensitic transformation.

Table 5.5 Deformation gradient tensors of twinning of Type-I DeF-twin of variant C and shuffling of variant A in the macroscopic sample coordinate frame. The compressive load is applied along the X axis.

Variant	Deformation gradient tensor, ε_{ij}		
C (to E)	0.9521	-0.0263	0.0072
	0.0881	1.0484	-0.0132
	0.0033	0.0018	0.9995
A (to NM)	0.9460	-0.0087	0.0158
	0.0859	1.0572	-0.0063
	-0.0048	-0.0205	0.9885

Another spectacular phenomenon is the noticeable appearance of variant O formed in the NM martensite regions, notably in the neighborhood of variant E with a straight interface, as displayed in **Fig. 5.11($\mathbf{d_1}$)**. Moreover, it grows, on one hand, together with the NM martensite into variant A and, on the other hand, into the NM martensite in the same region with the imposed macroscopic deformation (**Fig. 5.11($\mathbf{c_1}$)** and **($\mathbf{d_1}$)**). Such a character suggests that the formation of variant O is realized by the reverse intermartensitic transformation from the NM

martensite. By crystallographic calculations, we find that O-NM possesses the OR of intermartensitic transformation. It is $(0\ 0\ 10)_{7M}$ // $(1\ 1\ 2)_{NM}$ and $[10\ 0\ 0]_{7M}$ // $[1\ 1\ -1]_{NM}$ with a deviation angle of the OR planes and OR directions of 0.32° and 0.30°, respectively. This further confirms that the reverse martensitic transformation is possible by the reverse shuffling on the same system. By comparing **Fig. 5.11(c_1)** and **(d_1)**, we also notice that variant E and C slightly thicken at the expense of the NM and variant A, suggesting that inverse intermartensitic transformation also happened from NM to variant E. Crystallographic examination reveals that the intermartensitic transformation OR also exists between these two. It is $(0\ 0\ 10)_{7M}$ // $(1\ 1\ 2)_{NM}$ and $[-10\ 0\ 0]_{7M}$ // $[1\ 1\ -1]_{NM}$ with deviation angles between the respective OR planes and the OR directions of 0.67° and 0.70°. Thus the difference between these two reverse intermartensitic transformation processes (NM to variant E with slight amount and NM to O with large amount) should be studied to figure out the reason why NM martensite prefer to transform to variant O of the 7M martensite rather than to variant E.

With the ORs, the reverse shuffling process (intermartensitic transformation) from NM martensite to variant O and to variant E can be visualized by the atomic correspondences between each pair, as displayed in **Fig. 5.12**. Since the lattice deformation in the reverse intermartensitic transformation to form 7M variants can be regarded as an average shear to change the tetragonal NM lattice to the average lattice of the monoclinic martensite, plus a lattice modulation to eventually form the 7M modulated martensite. Thus the average shear distinguishes the lattice deformation to form the two 7M variants (O and E), as the lattice modulations for them are the same. The calculated average shears to form variant O and E are 0.1362 and 0.2505, respectively. Obviously, the reverse shuffling to variant O is much smaller and thus much easier than that to variant E, therefore the NM martensite prefers to transform to variant O.

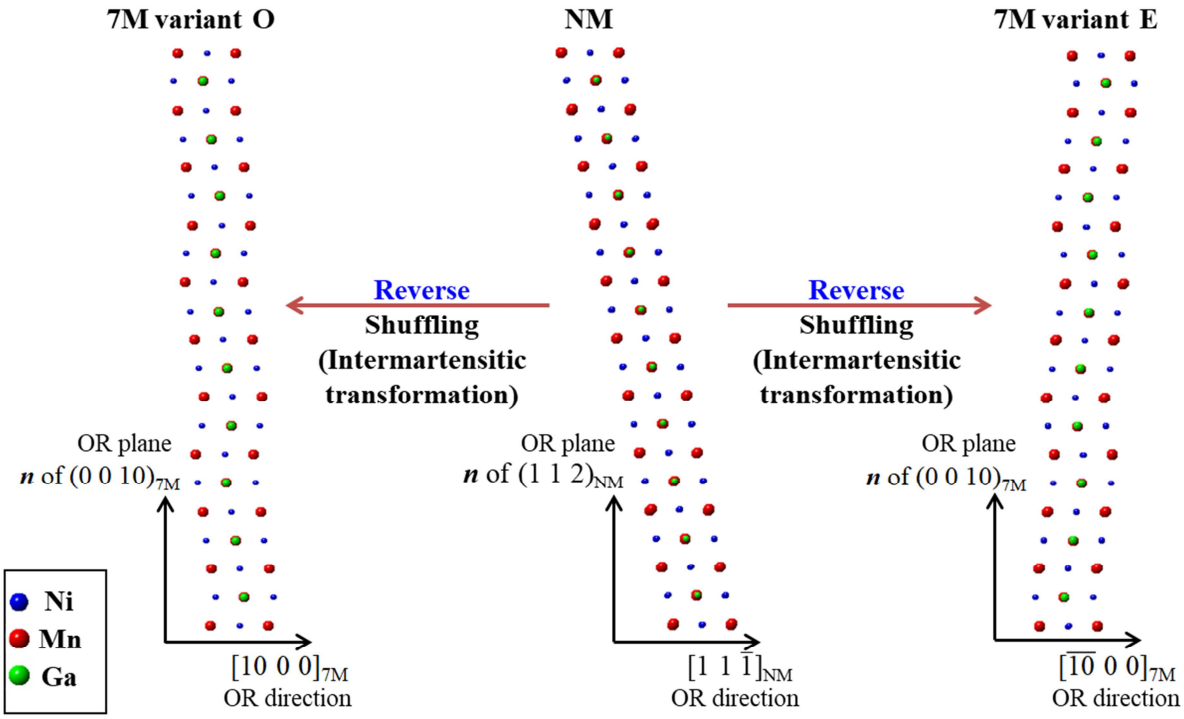

Fig. 5.12 Atomic correspondences of 7M variant O and E and NM martensite under the intermartensitic transformation ORs. ***n*** represents the OR plane normal.

To further study the contribution of the formation of variant O to the macroscopic deformation, the reverse intermartensitic transformation is further correlated with the macroscopic deformation caused by the external compressive load. The accommodation capacity of this process is evaluated by the corresponding deformation gradient tensor as given in **Table 5.6**. In the tensor, the value of the ε_{11} are slightly higher than 1, meaning no contribution to the macroscopic deformation. Moreover, the deformation gradient tensor has ε_{22} smaller than 1 and ε_{33} larger than 1 which is opposite to the deformation gradient tensors of Type-I DeF-twinning of variant C and of the shuffling of variant A, as displayed in **Table 5.5**. This indicates that the reverse martensitic transformation from the NM to variant O is not compatible with the macroscopic deformation. It should be induced by local constraints. By comparing the deformation gradient tensor of variant C to E and that of variant A to NM in **Table 5.5**, one can find that although the deformations of the Type-I DeF-twinning of variant C and the shuffling of variant A are largely consistent, small difference exists between the corresponding elements in the two tensors. These differences are accumulative with the growth of variant E and the NM martensite and become un-ignorable when the two

constituents exceed certain sizes, thus local accommodation should be required. The reverse intermartensitic transformation could be in this purpose. Thus we further calculated the deformation gradient tensor from variant A to O via the intermartensitic transformation and the reverse intermartensitic transformation. The results are given in **Table 5.7**. For an easy comparison, the deformation gradient tensor describing the transformation from variant C to E by twinning of Type-I DeF-twin is copied from **Table 5.5**. One can found that excellent matches happen to the three corresponding elements in the first row in the two tensors. This row concerns one normal strain and two shear strains in the compression direction, the most important deformation direction in the present work. The excellent matches indicate that the occurrence of the reverse intermartensitic transformation is indeed to accommodate the accumulated incompatible strains between the formation of variant E and the formation of NM martensite. However, the matches between the corresponding elements in the second and the third rows in the two tensors are not as excellent as those of the first row, meaning that the accommodations in the directions perpendicular to the compression direction are not so good. This may explain why the replacement of the NM martensite by variant O is not always complete, as shown in **Fig. 5.11($\mathbf{d_1}$)**. Variant O fully stretches in the length direction of the NM martensite that is close to the compression direction (the X axis) but does not in the directions that are close to the directions perpendicular to the compression direction.

Table 5.6 Deformation gradient tensors of reverse intermartensitic transformation (NM to variant O) in the macroscopic sample coordinate frame. The compressive load is applied along the X axis.

Variant	Deformation gradient tensor, ε_{ij}
NM to O	1.0084 -0.0046 -0.0039 0.0342 0.9366 -0.0523 0.0290 0.0684 1.0666

Table 5.7 Deformation gradient tensors of variant A to NM to variant O, and variant C to variant E in the macroscopic sample coordinate frame. The compressive load is applied along the X axis.

Variant	Deformation gradient tensor, ε_{ij}
A to NM to O	0.9535 -0.0135 0.0121 0.0483 0.9915 -0.0581 0.0282 0.0502 1.0544
C to E	0.9521 -0.0263 0.0072 0.0881 1.0484 -0.0132 0.0033 0.0018 0.9995

In view of the appearance of variant O (**Fig. 5.11(c_2)** and **(d_2)**), coherent interfaces are expected between variant O and the adjacent variants separated by straight interfaces. In addition to the NM martensite, variant O is also in neighbor with variants E and A, thus the respective orientation relationships were calculated with the measured Euler angles by EBSD. The results are given in **Table 5.8**. It can be seen that between variant O and variant E (separated by straight interface) there exist two 180° rotations, suggesting that the two variants are in compound twin relation. This compound twin is not the same as that of the compound TrF-twin. To fully identify the twinning features of this twin, the twinning elements are determined using the method in Ref. [5.22]. The results are displayed in **Table 5.9**. In addition to the differences in twinning plane and twinning direction and their conjugates, the noticeable difference happens to the twinning shear. The shear magnitude of this compound twin is 10 times higher than that of the compound TrF-twin (**Table 5.2**) and is close to those of the Type-I and Type-II DeF-twins (**Table 5.4**). Here we denote this twin compound DeF-twin. Further analysis on the interfaces between variant O and E using the indirect two trace method [5.23] revealed that the O-E interface coincides largely with the twinning plane with a deviation of about 0.47°, as illustrated in **Fig. 5.13**, thus this interface should be coherent. This explains why the O-E interfaces are always straight. However, the orientation relationship between variant O and A is not clearly defined. The two variants are related to each other with a relation between the Type-I and the Type-II DeF-twins. The

ambiguous twin relation between these two variants further confirm that the growth of variant O into variant A is realized by two steps, firstly intermartensitic transformation of variant A to NM and then reverse intermartensitic transformation from NM to variant O.

Clearly the formation of the new variant O has two folds of importance. The first it annihilates the local incompatible strain created by the formation of variant E from variant C through type-I DeF-twinning and the formation of NM from variant A through intermartensitic transformation. This further ensures the steady deformation process of the present material by the continuous process of highly coordinated twinning and intermartensitic transformation until the disappearance of the remaining variants (C and A). The second is that it creates a new twin relation with the neighboring variant of variant O, i.e., the compound DeF-twin. This twin has relatively higher twinning resistance and lower shear strain.

This part of the results evidence that the last part of the steady plastic deformation is realized by intensive twinning of the DeF-twins and intermartensitic transformation. During such processes to accommodate the macroscopic strain, local incompatible strain is accumulated and thus the inverse martensitic transformation is initiated. In general, the twinning process and the intermartensitic transformation proceed in a strain compatible way without much local resistances from incompatibles strain, therefore the plastic deformation is still in a steady way just with a little rise of the stress level as seen in the second plateau part of the stress-strain curve with respect to that of the first plateau part.

Table 5.8 Misorientation (in rotation angle and axis) between variant O and variant E, and O and A.

Variant pair	Misorientation angle (°)	Plane normal or direction parallel to $\vec{d}$ (in the lattice basis of the 7M modulated martensite)
O-E	179.89	[10 0.006 0.003] 0.201°from [10 0 0]
	179.91	(-0.003 -0.001 10) 0.203° from (0 0 10)
O-A	89.83	(1 -1.982 10.90) 2.243° from (1 -2 10)
	179.81	[10 -11.13 1.094] 2.605° from [10 -10 1]

Table 5.9 Twinning elements (K_1, K_2, η_1, η_2, P and s) of the compound DeF-twin in **Table 5.8**.

Elements / Variant pairs	O-E (compound DeF)
K_1	(0 0 10)
K_2	(1 0 0)
η_1	[10 0 0]
η_2	[0 0 1]
P	(0 -1 0)
s	0.1143

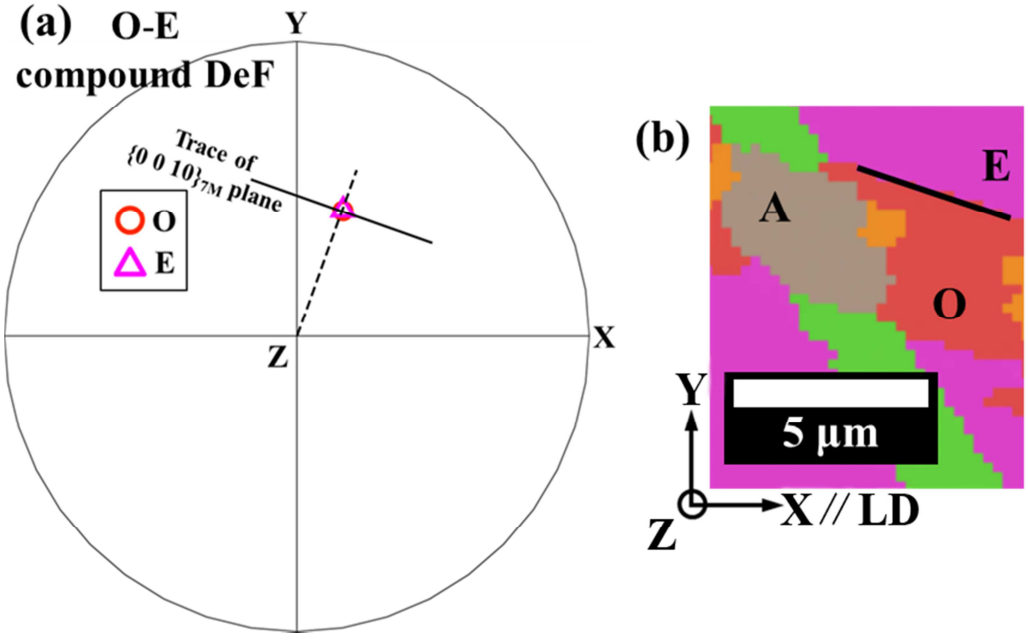

Fig. 5.13 (a) Pole figure of the twining plane of twin variant pair O-E (compound DeF, $\{0\ 0\ 10\}_{7M}$) and (b) the EBSD IPF micrograph of the microstructure of the variant pair O-E. In the figures the O-E interface traces are marked with the black straight lines.

When the deformation progressed to 5.5% in reduction, *i.e.*, the second linear part of the stress-strain curve (**Fig. 5.9(a)**), variant A and C almost disappeared through the twinning of Type-I DeF-twin process (variant C to variant E). The intermartensitic transformation (variant A to the NM) and the reverse (the NM to variant O) occurred, as shown in **Fig. 5.11(e_1)** and **(e_2)**. At this deformation state, the area fractions of variants E and O increase but that of the NM decreases. This confirms that the peak intensity decrease of the NM martensite in the neutron diffraction pattern in the second plateau part of the stress-strain curve in **Fig. 5.9(a)** is originated from the reverse intermartensitic transformation rather than NM variant reorientation. The area fraction increase of variant E is realized not only by the twinning of Type-I DeF-twin process from variant C to E but also from the compound DeF-twining process from variant O to E and the reverse intermartensitic transformation from the NM to E. As these shear systems have lower SFs (<0.02) and smaller shear magnitudes that represent higher twinning resistances, the further increase of the deformation strain required much higher stress level compared with that in the plateau part. Thus the stress-strain curve experiences a second linear part due to the weak accommodation capacity of these shear systems to the macroscopic deformation.

5.2.1.3 Texture evolution

The above deformation processes results in the orientation change of martensite variants. **Fig. 5.14 (a)** and **(b)** show the EBSD $\{0\ 2\ 0\}_{7M}$ pole figures of the respective initial state (0%) and the final deformed state (-5.5%). It can be clearly seen from the pole figures that the $\{0\ 2\ 0\}_{7M}$ planes of the four original variants are approximately parallel to the X axis (the compression direction, LD). In detail, variant A and D orientated with their $\{0\ 2\ 0\}_{7M}$ planes almost perpendicular to the Z axis, whereas variant B and C to the Y axis. As the deformation progressed to the reduction of 5.5%, the original variants (A, B, C and D) are all exhausted by the new variants (E and O). The $\{0\ 2\ 0\}_{7M}$ planes of these new variants appear to be perpendicular to the LD, as shown in **Fig. 5.14(b)**, forming a kind of $<0\ 2\ 0>_{7M}$ fiber texture in the compression direction, LD.

To further investigate if such texture change happens globally, which indirectly verifies if the same deformation processes visualized by the local EBSD examinations happened globally, through-volume neutron diffraction pole figure measurements were performed at the initial un-deformed state and the deformed states with reductions of 2%, 4% and 6%. The corresponding $\{0\ 2\ 0\}_{7M}$ pole figures are displayed in **Fig. 5.15**. The four pole figures clearly show the similar orientation evolution from a texture with the $\{0\ 2\ 0\}_{7M}$ poles located at the

outer circle of the pole figure, meaning that the $\{0\ 2\ 0\}_{7M}$ planes are nearly parallel to the compression direction, LD, to a fiber texture with the $\{0\ 2\ 0\}_{7M}$ poles located at the center of the pole figure, meaning that after the compression all the variants formed in the measured volume have their $<0\ 2\ 0>_{7M}$ directions parallel to the LD. This result indicates that the deformation process through detwinning, twinning and intermartensitic transformation and the reverse intermartensitic transformation revealed by the local *in-situ* EBSD investigation in the present work is representative for the whole material.

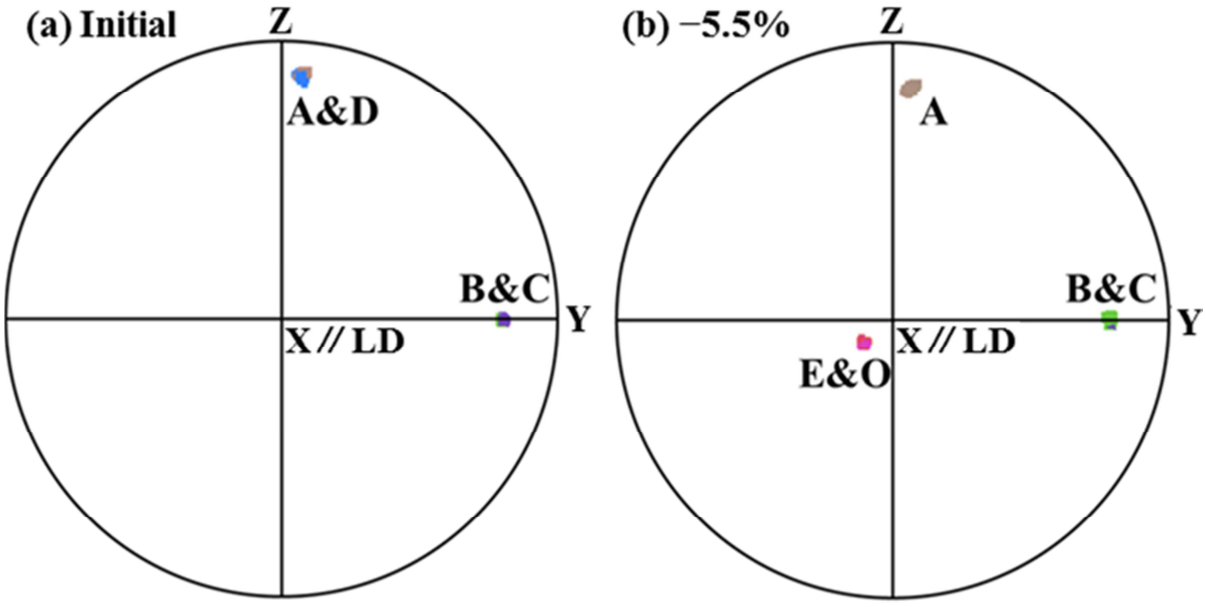

Fig. 5.14 EBSD $\{0\ 2\ 0\}_{7M}$ pole figures of (a) the initial state and (b) the deformed state (5.5% in reduction). The X direction is parallel to the compression direction.

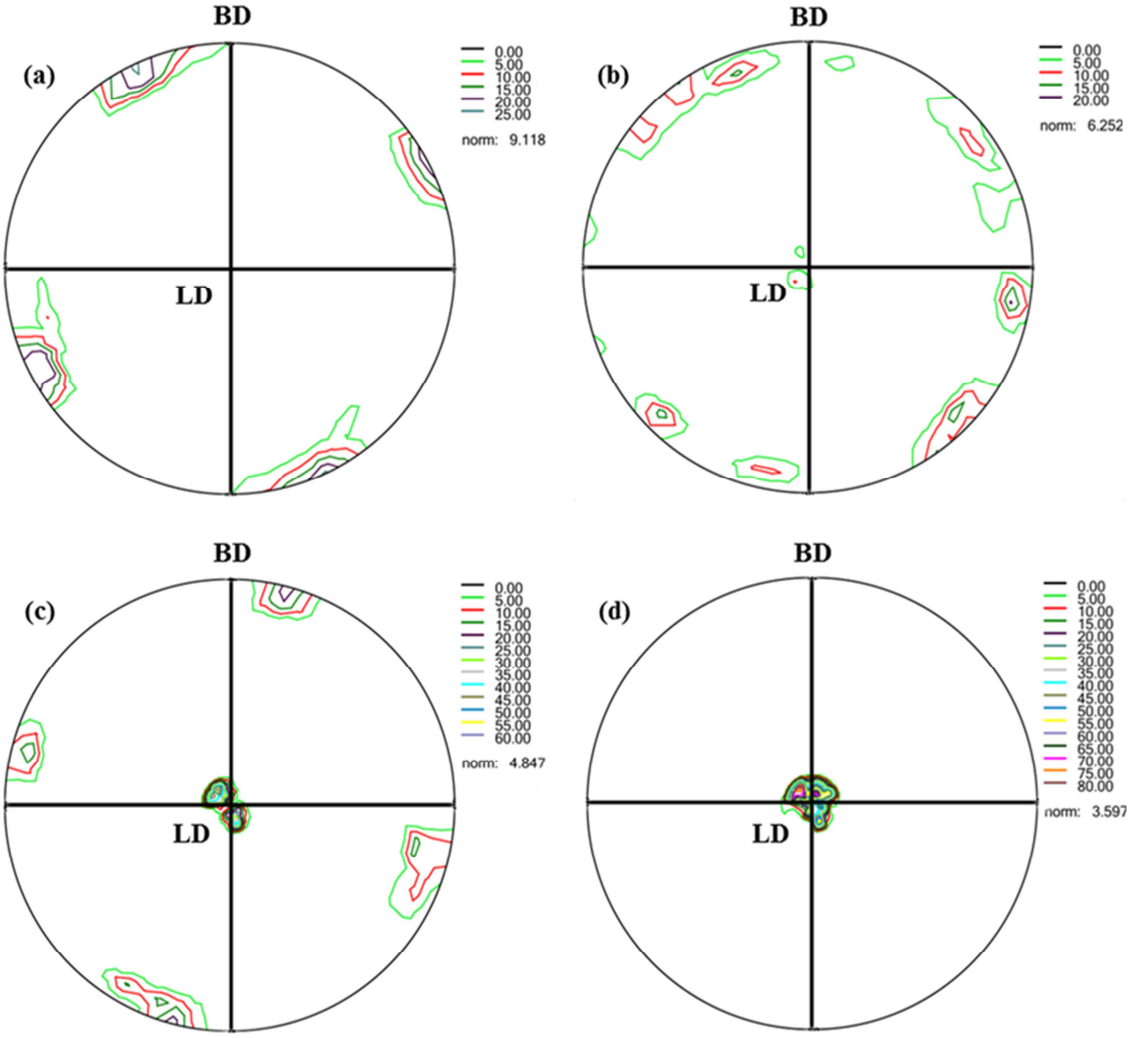

Fig. 5.15 $\{0\ 2\ 0\}_{7M}$ pole figures from through-volume neutron diffraction measurements of the initial un-deformed state (a) and the deformed states corresponding to 2% (b), 4% (c) and 6% (d) in reduction. BD is the beam direction and LD is the compression direction.

5.2.2 Summary

The microstructure evolution and the crystallographic orientation change during unidirectional compression in a Ni-Mn-Ga alloy prepared by directional solidification were investigated by *in-situ* neutron diffraction measurements at macroscopic scale and by interrupted *in-situ* EBSD measurement at microscopic scale. It is revealed that each 7M modulated martensite crystal of the Ni-Mn-Ga alloys possesses various shear systems allowing reversible processes of twinning (twinning and detwinning) and reversible intermartensitic transformation (forward and reverse). The plastic deformation of the Ni-Mn-Ga alloys in their martensitic state is realized by the activation of the various detwinning

processes of the TrF-twins and the twinning of DeF-twins and intermartensitic martensitic transformation without any involvement of dislocation slip. The twinning and intermartensitic transformation processes are highly compatible to the macroscopic strain and to each other.

The local incompatible strains accumulated at large deformation amount can further be accommodated by inverse intermartensitic transformation through forming new 7M variants. These processes allow total reorientation of the initial variants and ensure a large steady stress-strain regime (plateau part). The orientations of the new variants render their shear systems to unfavorable orientation with respect to the external load. Further deformation is realized by the shear systems (twinning and shuffling) with higher resistances and lower strain capacities, giving rise to the appearance of the second line part of the stress-strain curve.

The results of the present work provide detailed deformation mechanism information of 7M Ni-Mn-Ga martensite and their mechanical responses to the external loading. This result provides basic experimental data for mechanical simulation work for intermetallic compounds, especially shape memory alloys.

Reference:

[5.1] V. A. Chernenko. Scr. Mater. 40 (1999) 523-527.

[5.2] U. Gaitzsch, M. Pötschke, S. Roth, B. Rellinghaus, L. Schultz. Acta Mater. 57 (2009) 365-370.

[5.2] R. Chulist, L. Straka, N. Lanska, A. Soroka, A. Sozinov, W. Skrotzki. Acta Mater. 61 (2013) 1913-1920.

[5.4] A. Sozinov, N. Lanska, A. Soroka, W. Zou. Appl. Phys. Lett. 102, 021902 (2013).

[5.5] R. C. O'Handley, S. J. Murray, M. Marioni, H. Nembach, S. M. Allen. J. Appl. Phys. 87, 4712 (2000).

[5.6] Z.B. Li, B. Yang, N.F. Zou, Y.D. Zhang, C. Esling, W.M. Gan, X. Zhao, L. Zuo. Mater. 10 (2017).

[5.7] Z.B. Li, N.F. Zou, B. Yang, W.M. Gan, L. Hou, X. Li, Y.D. Zhang, C. Esling, M. Hofmann, X. Zhao, Liang Zuo. J. Alloys & Comp. 666 (2016) 1-9.

[5.8] Z.B. Li, Y.D. Zhang, C. Esling, W.M. Gan, N.F. Zou, X. Zhao, L. Zuo. Appl. Phys. Lett. 105, 021907 (2014).

[5.9] Z.B. Li, Y.D. Zhang, C. Esling, X. Zhao, Y.D. Wang, L. Zuo, J. Appl. Cryst. 43 (2010) 617-622.

[5.10] C. Jiang, J. Liu, J. Wang, L. Xu, H. Xu. Acta Mater. 53 (2005) 1111-1120.

[5.11] O. Heczko, L. Straka. Mater. Sci. Eng. A 378 (2004) 394-398.

[5.12] A. Rudajevová, M. Frost, A. Jäger. Mater. Sci. Technol. 23 (2007) 542-546.

[5.13] L. Righi, F. Albertini, E. Villa, A. Paoluzi, G. Calestani, V. Chernenko, S. Besseghini, C. Ritter, F. Passaretti. Acta Mater. 56 (2008) 4529-4535.

[5.14] L. Straka, O. Heczko, H. Hänninen. Acta Mater. 56 (2008) 5492-5499.

[5.15] Z.B. Li, Y.D. Zhang, C. Esling, X. Zhao, L. Zuo. Acta Mater. 59 (2011) 2762-2772.

[5.16] N.F. Zou, Z.B. Li, Y.D. Zhang, B. Yang, X. Zhao, C. Esling, L. Zuo. Inter. J. Plast. 100 (2018) 1-13.

[5.17] M. Chmielus, K. Rolfs, R. Wimpory, W. Reimers, P. Müllner, R. Schneider. Acta Mater. 58 (2010) 3952-3962.

[5.18] Z.B. Li, Y.D. Zhang, C. Esling, H. Yang, J.J. Wang, C.S. He, X. Zhao, L. Zuo. Mater. Sci. Forum 706 (2012) 1879-1884.

[5.19] Z.B. Li, Y.D. Zhang, C. Esling, X. Zhao, L. Zuo. Acta Mater. 60 (2012) 6982-6990.

[5.20] H.L. Yan, B. Yang, Y.D. Zhang, Z.B. Li, C. Esling, X. Zhao, L. Zuo. Acta Mater. 111 (2016) 75-84.

[5.21] Z.B. Li, B. Yang, Y.D. Zhang, C. Esling, N.F. Zou, X. Zhao, L. Zuo. Acta Mater. 74 (2014) 9-17.

[5.22] Y.D. Zhang, Z.B. Li, C. Esling, J. Muller, X. Zhao, L. Zuo. J. Appl. Cryst. 43(6) (2010) 1426-1430.

[5.23] Y.D. Zhang, C. Esling, X. Zhao, L. Zuo. J. Appl. Cryst. 40(3) (2007) 436-440.

6. Perspectives

Of course, science is endless. As driven by the Helmholtz mission of solving grand challenges which facing science and industrial using advanced large-scale facilities, I try to pursue persistently scientific researches which have practical applications at the beginning of my choice of a science career, and continue to maintain strong interest and extensive cooperation, and as well to train the young scientist taking the advantages of using large scale facilities. Following two main points will represent my perspectives.

6.1 Adapting the neutron scattering technique to solve modern grand challenges

It is known that energy, information technology, life and health are the main challenges for the modern human society. Research and development in the fields of engineering materials is aiming to improve their functionalities. New findings will lead to further developments affecting transportation, vehicles, aircrafts, sensors, mechanical and electronic nano-devices, and etc. Neutron scattering as one of the unique materials characterization methods will greatly contribute to the fundamental scientific research and as well as the practical applications. Using innovative techniques and novel methods based on neutron scattering allow one to obtain a unique insight into the structure and dynamic processes of matter from microscopic to macroscopic scale. This is specially related to my research field. Following aspects are foreseen.

(1) *In-situ* or *in-operando* characterization of structure, texture and stress. Mechanical or functional properties of materials are solely represented during the real service. It is known that the inner structure determines the properties of the materials. It is significant to know or to investigate *in-situ* what happens during the service of the materials. Neutron diffraction demonstrates the main advantage of high penetration (e.g., about 50 mm for steel) for such kind of analysis. Standard or special sample environment can be easily designed and installed in the neutron diffractometer, and the sample dimension can be tested as it is in real service. Phase transition, strain/ stress, texture information can be then simultaneously obtained. This will greatly contribute to the new materials design, such as light weight Mg alloys, Al-Si based alloys, and high temperature alloys (Ni super alloys, Ti-Al intermetatics, Co based alloys, etc.).

(2) Update and upgrade the neutron diffraction technology. This might be purely technical requirements, such as automatic and accurate gauge volume definition, automatic sample handling, high resolution monochromator, and etc. Moreover, update the data treatment software from raw images to final profile or property calculations.

(3) Most important, to motivate more young people interested in neutron scattering is also our task. Regular teaching or training course is one way. The best thing will be help them to apply neutron scattering measurement technique to his/ her own research topic.

6.2 Continue and further deepen current research topics

My current main research interests have been described above, however, some need to be continued and strengthened. This will be listed as follows.

(1) R&D of the new light weight Mg alloys through alloy deign for structure application or as bio-materials. One of the effective methods to realise low cost micro-alloying. While the main mechanisms have not been fully understood yet. The addition of other elements to Mg has to some degree effects on the activation of various slip or twinning systems in structural applications. Another interest is the Mg based composite reinforced by nano particles. Investigation on the strain/ stress state of these composites during deformation will help one to understand the role of each phase and as well the strengthening mechanisms.

(2) Broaden the studies of anisotropy effect on the residual stress of engineering materials, especially on materials through welding or other jointing techniques. It is well known that the raw materials for final engineering products are mostly rolled or extruded. The pre-existed preferred orientation / texture will have to some extent effects on the following deformation or processing, especially on the residual stress profile. This is extremely important for joining components. Through series studies on the anisotropic effect on stress profile by neutron diffraction could help to optimize the jointing process.

(3) Further study on the γ-Ti-Al based alloys which are an attractive material for structural high temperature applications due to their high specific tensile and creep strength. Nevertheless, their wider application is still hampered by the difficulties involved in TiAl processing and by the limited understanding how ductility and damage tolerance of the material during service is influenced by microstructure and phase constituents. This can be studied by *in-situ* neutron scattering.

6.3 New research topics

So far, following aspects has not much been studied and will be attractive to me and to our institute, which will broaden the neutron applications.

(1) Magnetic textures investigation by neutron diffraction. This is not a new topic but it has not been carried out at GEMS-N at FRM 2 yet. The definition of the crystallographic texture can also be applied to describe the magnetic state of a polycrystalline, ferromagnetic materials, as has been reported in detailed by Bunge. With neutron diffraction pole figure measurement the

contribution of nuclear scattering and magnetic scattering could be solved by an iterative method. Anyway, strong cooperation with other potential institutions is necessary.

(2) Based on the internal research interest of our institute, a commercial dilatometer has been modified for neutron facilities and will be implemented at GEMS-N (located at FRM 2) for both *ex-situ* and *in-situ* phase kinetics and deformation studies. This investment will open a new broad field for us to combine diffraction and dilatometry studies, with the focusing on the materials for high temperature applications.

(3) Study on the modern **AM** - Additive Manufacturing technology like **SLM** - Selective Laser Melting, there are lots of initiatives to understand the microstructure evolution (like phase transition, lattice strain and texture evolution, etc.) during the whole manufacturing process. And as well, the residual stress of the quasi -/ finished components, which might affect their properties in real service.